

81

THERMAL DESIGN AND ANALYSIS OF A RECUPERATIVE
COMBUSTOR FOR GAS-TURBINE COMBUSTION

by

Vishnu P. Venkatesh

B.Tech.(Honours), Naval Architecture and Ocean Engineering
Indian Institute of Technology
Kharagpur
(1991)

Submitted to the Department of
Mechanical Engineering
in Partial Fulfillment of the Requirements
for the Degree of

MASTER OF SCIENCE

at the

MASSACHUSETTS INSTITUTE OF TECHNOLOGY

August 1993

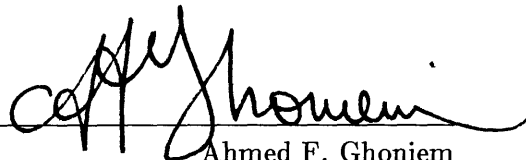
© Massachusetts Institute of Technology, 1993

Signature of Author: _____



Department of Mechanical Engineering
August 1993

Certified by: _____



Ahmed F. Ghoniem
Professor, Mechanical Engineering
Thesis Supervisor

Accepted by: _____



Ain A. Sonin
Chairman, Departmental Graduate Committee

MASSACHUSETTS INSTITUTE
OF TECHNOLOGY

NOV 29 1993

LIBRARIES
ARCHIVES

**THERMAL DESIGN AND ANALYSIS OF A RECUPERATIVE COMBUSTOR
FOR GAS-TURBINE COMBUSTION**

by

Vishnu P. Venkatesh

Submitted to the Department of Mechanical Engineering
on August 24, 1993 in partial fulfillment of the
requirements for the Degree of Master of Science in
Mechanical Engineering

ABSTRACT

The thermal design and analysis of a recuperative combustor to burn low-calorific-value fuels, specifically an ultra-lean mixture of methane and air available in coal mine exhaust is performed. The combustor is designed to be fitted onto a gas-turbine engine. The recuperative combustor consists of two parts: a heat exchanger to heat up the reactant stream to a temperature necessary to sustain spontaneous combustion and a combustor where the flame is stabilized and the fuel-air mixture burnt. The perfectly stirred reactor model is employed to predict the minimum temperature at which the fuel-air mixture sustains spontaneous combustion. For a particular fuel-air mixture, with a given equivalence ratio and specific mass-flow rate, there is a unique asymptotic value of temperature above which spontaneous combustion in a well-stirred reactor is sustainable. The function of the heat exchanger is to transfer excess enthalpy of the hot products at the exit of the combustor to the cold reactants at the exit of the compressor (recuperation). The ϵ -NTU method is employed on the assumption that the heat exchanger is compact. The design and analysis exercise strongly recommends the use of plate-fin counterflow heat exchangers and provides quantitative data for the same. A swirler-equipped combustor is found most suitable for design of the combustor. Parameters that influence the development of the central recirculation region where the flame is anchored are studied. Quantitative recommendations for the geometry of the combustor and the swirler are given based on these parameters. Numerical visualization of the non-reacting flow in the recommended combustor is also carried out.

Thesis Supervisor: Ahmed F. Ghoniem
Title : Professor of Mechanical Engineering

Dedicated to my family

Prem & Raj,

Chotu,

Oman & Tha

Acknowledgement

I wish to acknowledge the role of a number of people who have been instrumental in the successful completion of this thesis. Since each contribution is important, this list is not in any particular order:

My advisor, Professor Ahmed F. Ghoniem, who not only guided me through this project but also served as my mentor, academic and otherwise,

Dr. Peet Sööt, President, Northwest Fuel Development, for sponsoring the exciting research behind this thesis,

Professor David G. Wilson, whose timely advice and comments were catalysts in the design of the heat exchanger,

FLUENT Inc., for their excellent numerical flow visualization package used in the combustor design,

Kevin Wasson of the Heat Transfer Laboratory at MIT for his assistance in FLUENT printouts,

My friends, Satbir, Hitesh, Nikhil and Ujjwal for egging me on and lifting my spirits when most needed,

My parents, who inspired the cutting edge when I showed signs of wear,

And my better half, Maitreyi, who always stood by me.

24 August 1993

Vishnu Venkatesh
Cambridge, MA 02139

Contents

1	Introduction	1
1.1	Motivation for the project	1
1.2	Means of recovering methane	2
1.3	Phase I of the project	3
1.4	Phase II	6
1.5	Parts of the thermal design problem: basic mechanism of combustion chemistry	8
1.6	Heat exchanger design	11
1.7	Combustor design	12
1.8	Pivotal point: the perfectly stirred reactor model of the combustion zone	14
1.9	Design integration	15
1.10	Thesis Layout	15
2	Perfectly Stirred Reactor model of the combustor	17
2.1	Perfectly Stirred Reactor model	18
2.2	Numerics	23
2.3	Results and predictions of the perfectly stirred reactor model	23

2.4	Summary	27
3	Cycle Calculations for the GS-350	28
3.1	Air-standard ideal Brayton Cycle	28
3.2	Air Standard ideal Recuperative Brayton Cycle	31
3.3	Ideal Cycle Efficiencies	33
3.4	Actual Overall gas-turbine Efficiency	34
3.4.1	Compressor efficiencies η_{cad} , η_{pc} and compression work W_c	35
3.4.2	Turbine efficiencies η_{tad} , η_{pt} and turbine work W_t	39
3.4.3	Overall gas-turbine efficiency η	43
4	Heat Exchanger Design	47
4.1	Performance criterion for the heat exchanger	49
4.2	Heat transfer algorithm for compact heat exchanger design: the ϵ -NTU method . . .	50
4.3	Algorithm for pressure drop analysis in compact heat exchangers	52
4.4	Types of compact heat exchangers	54
4.5	Design of the Steady Flow heat exchanger	56
4.5.1	Fabricated heat exchanger: performance analysis	60
4.5.2	Multipass-crossflow steady flow heat exchanger	68
4.5.3	Plate-fin counterflow steady-flow heat exchanger	86
4.6	Design of the Periodic Flow heat exchanger	94
4.6.1	Choice of matrix geometries	94
4.6.2	Data presentation for the hexagonal ceramic matrix	95
4.6.3	Numerics for the periodic flow heat exchanger	98

4.6.4	Results and Discussion	98
4.6.5	Power required to rotate the matrix	101
4.7	Decision making: the Steady-flow vs. the Periodic-flow heat exchanger	102
4.8	Conclusions	103
5	Combustor Design	105
5.1	Requirements for the combustor that would burn ultra-lean methane-air mixtures . .	107
5.2	Types of ultra-lean combustors	108
5.2.1	Swiss Roll combustor	109
5.2.2	Swirl Combustors	110
5.3	Choice of ultra-lean combustor	114
5.4	Understanding the mechanism of swirl	114
5.4.1	Degree of swirl: the swirl number S	116
5.4.2	Conditions under which a recirculation zone is established	116
5.4.3	Size of the recirculation region	121
5.4.4	Effect of type of swirler on swirl flow	129
5.4.5	Precessing Vortex Core (PVC)	130
5.4.6	Effect of combustion on swirler combustor performance	132
5.5	Design parameters for the combustor	134
5.6	Swirler vane design	136
5.7	Heat transfer performance	138
5.8	Pressure drop in the combustor	141
5.9	Flowfield simulation	143

5.10	Conclusions	147
6	Conclusions and Future Work	149
6.1	Purpose of the thesis	149
6.2	Approach to the problem	150
6.3	Summary of design	150
6.4	Design integration	151
6.5	Future work and accuracy of the current design	152
	Bibliography	154
A	GS-350 cycle calculations: derivations	156
A.1	Efficiency of an Air-standard ideal Recuperative Brayton cycle	156
A.2	H_{pc} , W_c , η_{pc} and η_{cad}	158
A.2.1	Polytropic head work H_{pc} done in compression of a gas	158
A.2.2	Actual work done W_c done during compression	159
A.2.3	Polytropic efficiency during compression η_{pc}	159
A.2.4	Relation between polytropic efficiency η_{pc} and adiabatic efficiency η_{cad}	160
A.3	Exothermic Energy Yield (ψ) of a methane-air mixture	160
A.4	Relation between β and equivalence ratio of methane-air mixture ϕ	161

List of Symbols

- a : height of each pass in a heat exchanger
 A_p : pre-exponential factors
 b : width of each pass in a heat exchanger
 c : depth of each pass in a heat exchanger
 c_p : specific heat
 C : product of mass flow rate and specific heat
 C_{rot} : switching rate of matrix
 d, D : diameter
 E_a : activation energy
 f : friction coefficient, frequency
 G : axial flux
 h : specific enthalpy, heat transfer coefficient
 H : height
 H_p : polytropic head work
 \mathcal{H} : total pressure head
 k : rate of reaction, ratio of specific heats, thermal conductivity, plate spacing, turbulent energy
 K : coefficient associated with flow geometry
 L : length
 \dot{m}, M : mass flow rate
 n : number of passes
 N : number of plates, number of fins
 Nu : Nusselt number
NTU: number of transfer units
 o : throat diameter
 p : porosity
 P : pressure
 Pr : Prandtl number
 Q : stoichiometric heat of reaction
 \dot{Q} : rate of heat loss
 r : radius
 r_p : pressure ratio, radius to the precessing vortex core

R : universal gas constant
 Re : Reynolds number
 s : blade spacing
 S : swirl number
 St : Stanton number
 t : thickness
 T : temperature
 u : velocity
 U : velocity, overall heat transfer coefficient
 v : velocity
 V : velocity, volume
 \dot{w} : mass rate of fuel consumption
 W : work done
 x : length of recirculation zone, length of furnace region of combustor

Subscripts

c : compressor, contraction, cross-section
 ci : cold stream inlet
 co : cold stream outlet
 cad : compressor adiabatic
 d : disk, divergence
 e : exit
 f : flame, flow, fins, furnace
 h : hydraulic
 hi : hot stream inlet
 ho : hot stream outlet
 ir : reactants inlet
 k : species
 m : matrix
 mix : mixing
 mr : mean of reactants
 net : net amount
 o : outlet conditions
 p : products
 pc : polytropic compressor
 pt : polytropic turbine
 r : residence, reactor, reactants, recuperative cycle
 rr : reaction
 s : swirl
 t : turbine
 tad : turbine adiabatic
 $1,2,2',3,4,5,6,6'$: states in gas turbine cycles

Greek symbols

- α : empirical factors, blade angle
- β : percentage volume concentration of CH_4 in a CH_4 -air mixture
- δ : infinitesimal increment/decrement
- Δ : finite increment/decrement
- ϵ : effectiveness, dissipation energy
- η : efficiency of ideal simple and recuperative gas-turbine cycles, efficiency of swirl generation
- θ : angle
- ρ : density
- τ : time
- ψ : exothermic energy yield of a fuel-air mixture, stream function

Greek subscripts

- θ : linear momentum
- ϕ : angular momentum

Superscripts

- * : constant value, inlet conditions

Chapter 1

Introduction

By viewing Nature, Nature's handmaid, art,
Makes mighty things from small beginnings.
— *John Dryden (1631-1700 AD) - Annus Mirabilis*

1.1 Motivation for the project

Underground coal mines in the United States emit about 300 million ft³ of methane (CH₄) into the atmosphere *every day* from their ventilation air shafts (Ref[26]). Methane is a significant contributor to the greenhouse effect occurring over the entire globe. It has been shown that it is 5 to 50 times as damaging a greenhouse gas as carbon dioxide (CO₂) (Ref[26]). Methane is also the fastest growing of the common greenhouse gases; its concentration in the atmosphere increasing by a significant fraction in the last few decades. For example, underground coal emissions increased by 33% from 220 million ft³/day in 1975 to 300 million ft³/day (Ref[26]). Measurements have shown that the coal mining contribution to global methane concentration to be about 35%. Therefore, it has been recognized that any technology which showed some promise of curbing or converting

methane emissions from underground coal mines to a less damaging form would be welcomed. The commercial deployment of such technology supported first in the United States and then in the rest of the world is currently underway(Ref[26]).

1.2 Means of recovering methane

The difficulty in utilizing or recovering methane from the mine ventilation air has been its low to ultra-low levels. The mine ventilation air may not, under current safety regulations, contain more than 1% of methane in air by volume in working areas or in return air. If the 1% limit is exceeded in the return mains, then the mine operator must stop mining coal. If the methane concentration in the mine ventilation exceeds 2% in the main return airways, the mine must be evacuated. These have been decided on the basis of the flammability limit of methane; methane will spontaneously combust when the volume concentration of methane in a methane-air mixture is about 5%. The 2% maximum allows for some measurement error, and also recognizes that an average of 2% methane concentration in the well mixed ventilation return air may be caused by higher concentrations of methane in certain parts of mine entries and shafts.

Two methods, common for gas recovery, have been suggested: The first was carbon adsorption of the methane in the methane-air mixture. Due to the high volume flow rates (typically about 500,000 ft³/minute per shaft in gassy mines), the resultant pressure drop penalties through any containment vessels would have been prohibitive. The other was to burn the ventilation air in a combustion system. Since the methane is so dilute, a normal combustion system was ruled out. Catalytic combustion in ambient air was also ruled out because catalytic combustion is very expensive and more so since methane is the most difficult paraffinic hydrocarbon to oxidize. Of all the combustion systems considered, the gas-turbine system was found to be most suitable for this

project (Ref[26]).

The overall goals of this project seeks to establish the economic and technical feasibility of operating a gas-turbine engine that would achieve the objective of burning the mine ventilation air and at the same time provide a beneficial by-product - electric energy.

1.3 Phase I of the project

Broadly, the objectives of Phase I were to outline the technical feasibility for the gas-turbine engine modification to burn the ultra-lean mixture of methane-air. This includes combustor and/or gas-turbine design, commercial equipment review, fuel characterization, byproduct application, some economic analysis, a marketing study and outline of detailed efforts for Phase II.

A concept lean-burning combustor was suggested at MIT during Phase I as shown in Figure 1-1 (Ref[26]). It is a simple "boot-strap" heat exchanger/combustion chamber which raises the temperature of the fuel-air mixture entering the combustion zone to a level at which combustion can proceed - even for extremely dilute mixtures. This is also found from a fundamental study of combustion limits of methane-air mixtures (see Chapter 2). The concept heat exchanger used was a rotary disk-type ceramic heat exchanger that in one cycle, alternated between hot products and cold reactants transferring energy from the former to the latter (see Chapter 4 for a detailed description of this type of heat exchanger).

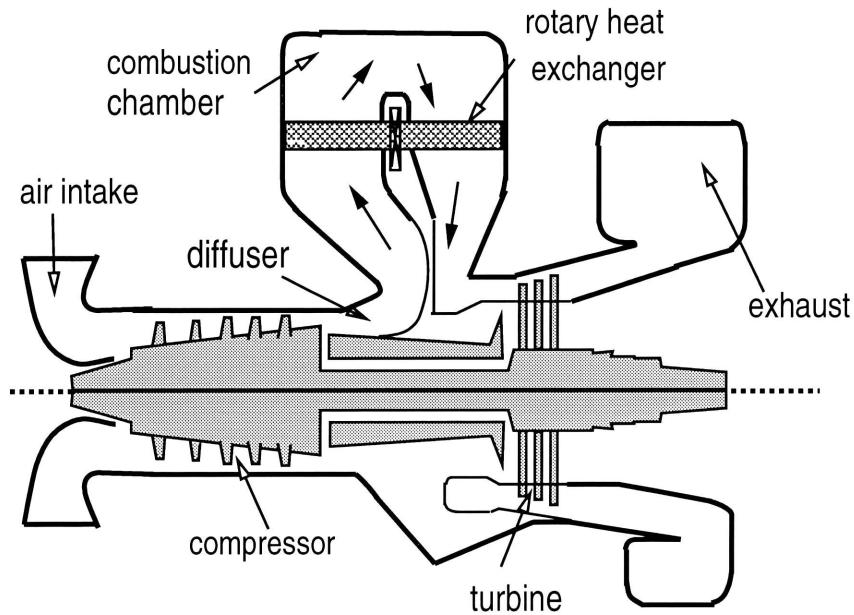


Figure 1-1: Concept lean burning combustor suggested at MIT during Phase I of the project. A rotary disk-type ceramic heat exchanger was suggested as part of this combustor (Ref[26])

The most likely candidate for the recuperative combustor design was identified as the Swiss Roll combustor (Ref[32]) shown in Figure 5-2. This ingenious design is an integrated heat exchanger-combustor and is shaped in the form of a spiral with the the reactants and products flowing in adjacent coils. The purpose of the spiral is to act as a heat exchanger. Combustion takes place in the cavity at the center of the spiral. Ultra-lean mixtures of the order of the 1% of methane in air have been shown to be burnt in this type of combustor.

Several types of gas-turbine cycles and potential gas-turbine engine configurations were examined (Ref[26]) for their ability to be adapted to burning 1-2% methane-air fuels. Three such hardware frames were identified:

- The Solar Saturn GS-350 gas-turbine engine. This engine operates on a low pressure ratio

with a simple gas-turbine cycle and has a maximum rated power output of 225 kW.

- A low pressure ratio, but highly regenerative engine and
- A ceramic turbine and ceramic rotary heat exchanger such as the GM-Allison experimental AGT-100 which has a maximum rated power output of 100 kW with a low pressure ratio.

Additionally, some potential military units were also identified. These included the M1-Abrams main battle tank AGT-1500 engine that develops 1500 hp and may become available on the civilian market as the engine nears the end of its nominal life. Another potential unit identified was the Allison 250, available in several versions, which develops power in the range of 450hp to about 1500hp and is used principally to power helicopters.

Several significant byproduct applications were recognized to utilize the low grade heat from the exhaust of the gas-turbine:

- The low grade heat could be used for greenhouses, an example of which was given as the Bon-neville Pacific plant in Rifle, Colorado where low grade waste heat is used to grow tomatoes and bell peppers.
- The low grade heat could be used to dry fuel. At the LFC plant in Yuba City, California, exhaust gases are used to dry wood and agricultural wastes.
- Reusing the waste heat in the form of regeneration in an industrial process that utilizes the gas-turbine.

A marketing study was also done including a study of coal mines and the kinds of ratings of the gas-turbines necessary for this application.

1.4 Phase II

The objective of Phase II is to develop the concepts and ideas of Phase I into greater detail.

Of the hardware frames mentioned in Section 1.3, the Solar Saturn gas-turbine GS-350 was selected. This gas-turbine, shown in Figure 1-2, has the following specifications:

- Maximum rated power output: 225 kW
- Compressor/Turbine pressure ratio: 4:1
- Compressor/Turbine type: single stage, centrifugal
- Gas-turbine cycle: simple (see Chapter 3 for more details about gas-turbine cycles)

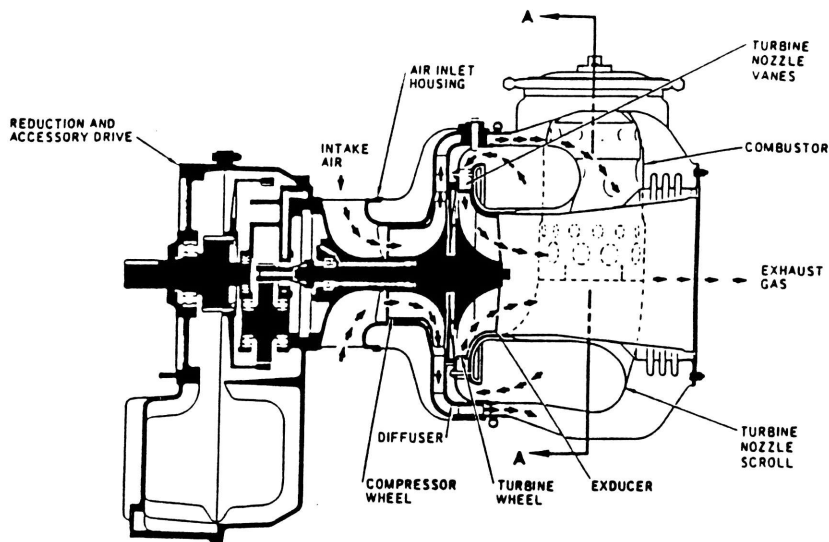
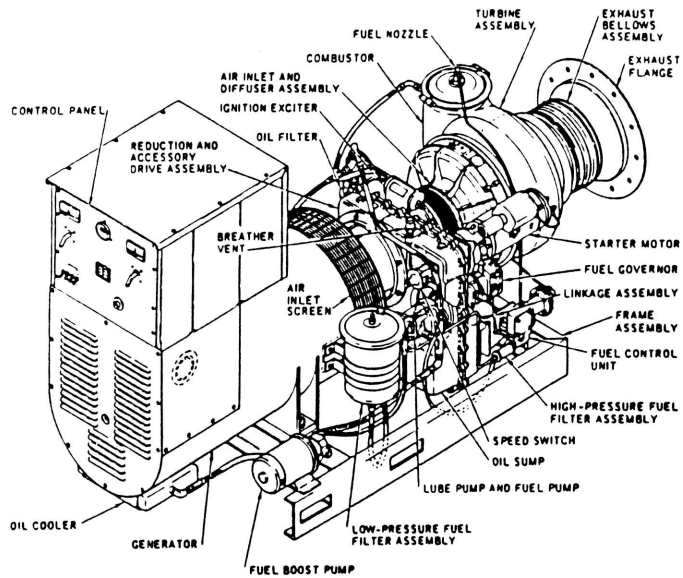


Figure 1-2: Solar Saturn GS-350 gas turbine (Ref[23])

The first objective of Phase II is to carry out a detailed thermal design modification to the combustor and/or gas-turbine itself given the GS-350 hardware. The following chapters in this thesis deal with the thermal design and analysis of the combustor and heat exchanger that are

necessary to be incorporated into the modified gas-turbine. The other objectives of Phase II are to carry out the mechanical design and testing of the designed combustion system.

1.5 Parts of the thermal design problem: basic mechanism of combustion chemistry

In order to fully realize the various aspects of the design problem, it is necessary to briefly inspect the mechanism of chemistry.

It has been experimentally observed that the variation in the lean limit of flammability with the initial temperature of a hydrocarbon fuel can be represented as an approximate constant flame temperature. Thus, as the fuel supplied heat is decreased, the initial mixture temperature must be raised such that the final temperature of the products remains the same. For methane, this constant flame temperature is approximately 1500 K. This result has been found experimentally in Ref[32] and proved theoretically in Chapter 2. This can be written as:¹

$$T_4 = T_3 + \frac{\Delta h}{c_p} \quad (1.1)$$

where Δh is the enthalpy of combustion = ϕQ

T_4 is the final products temperature

T_3 is the inlet temperature

Q is the stoichiometric heat of reaction

ϕ is the equivalence ratio of the fuel-air mixture defined as the fuel-air ratio

in the desired case divided by the fuel-air ratio in the stoichiometric case

¹the symbols T_4 and T_3 have been used to be consistent with the same symbols in later chapters

c_p is an average specific heat at constant pressure

Hence as the fuel is made leaner, i.e. ϕ is reduced, T_3 must be raised so that T_4 remains constant. Raising T_3 corresponds to preheating the fuel.

The greatest effect of preheating the fuel is on accelerating the rate of reaction given by the overall Arrhenius equation for $F + A \rightarrow \text{products}$:

$$\frac{d[F]}{dt} = -k_f[F]^{\alpha_F}[A]^{\alpha_A}$$

where:

$$k_f = A_p T^\beta \exp\left(\frac{-E_a}{RT}\right)$$

where $\frac{dF}{dt}$ is the rate of consumption of a species F having a concentration of [F]

A_p is the pre-exponential factor accounting for collision frequency between molecules and the orientation of the colliding molecules with respect to each other (steric factor)

E_a is the activation energy

R is the universal gas constant

α are the stoichiometric coefficients or empirical factors

Accelerating the rate of burning is best done by recycling some of the enthalpy of the hot products back to the cold reactants. This way, some of the excess enthalpy of the hot products is utilized to raise the overall combustion temperature. There are two ways by which a reactant

stream may be preheated by recycling enthalpy from the product stream: (a) in a combustor where the hot products are recirculated and mixed with the cold reactants and (b) in a heat exchanger where enthalpy is recycled by allowing heat transfer from the products to a heat transfer surface and then from this surface to the reactants. Unlike in case (a), case (b) this kind of heat transfer does not involve the dilution of the reactant stream. The influence of these two methods on the reaction rate are shown in Figure 1-3 (Ref[32]).

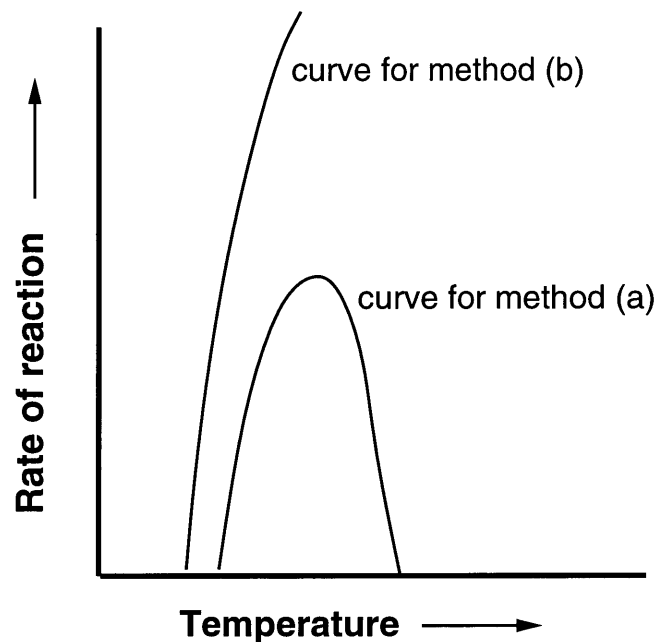


Figure 1-3: Influence of temperature on rate of reaction by recycling heat from hot products to cold reactants: method (a) recirculation of products with reactants resulting in increasing dilution of latter by former and method (b) heat transfer by means of a heat exchanger where there is no dilution of reactants (Ref[32])

The curve for method (a) shows that initially, the reaction rate is accelerated due to the temperature rise. However, as the products dilute the reactants, the concentration of reactant species

drops until the increase in reaction rate due to the rise in temperature is offset by the dilution. Conventional combustion systems utilize this method of heat transfer to the reactant stream because the fuel and air are not premixed and it is relatively easy to selectively increase the equivalence ratio of the fuel in the mixing zone (see Chapter 5). However, this method cannot be used with effectiveness to transfer heat to the reactant stream in the case of premixed ultra-lean mixtures of fuel-air since the fuel concentration in the mixture is very low concentration to begin with.

The curve for method (b), on the other hand, assures the monotonic increase in the reaction rate simply by heat transfer alone without dilution. This is the method that applies for both premixed and non-premixed fuels at all equivalence ratios (but is unnecessary in the case of non-premixed fuels used in conventional combustion systems) and is most useful in the case of ultra-lean fuel-air mixtures such as the methane-air mixture used in this project. Thus a heat exchanger is essential for ultra-lean combustion.

The recycling of heat, shown schematically in Figure 3-4, is called **recuperation**. Semantically, it is differentiated from regeneration, which is the heat transfer between two streams at different pressure. For example, regeneration through the a heat exchanger is employed in some gas-turbine cycles to heat the pressurized reactants prior to the combustor by utilizing the exhaust stream.

1.6 Heat exchanger design

Heat exchanger design is a complex problem because of the number of constraints including size, friction pressure loss, metallurgical and structural features and the continuous variation of thermophysical properties of fluids within the heat exchanger. There are also hundreds of surface geometries that could be potentially employed while a design is being attempted.

An enormous simplification in the analysis, yet without much loss of accuracy, is the assumption

that average thermophysical properties can be used over the entire volume of the heat exchanger especially if the heat exchanger is designed to be of small size. This is the definition of the compact heat exchanger (Ref[12]). Therefore, heat transfer coefficients are assumed to be of the same value regardless of the location in the heat exchanger. This is the basis of the ϵ -NTU (ϵ is the effectiveness of the heat exchanger and NTU is the non-dimensional number of transfer units; both terms are defined in Chapter 3) method of heat exchanger design. The gain in computation time and speed using this method more than makes up for the loss of accuracy.

Even with this simplification, heat exchanger design still requires an iterative procedure. Most often, inlet and outlet temperatures are not completely known (though the input may be sufficient to find a unique solution or a finite set of solutions) and therefore estimates are needed for thermophysical properties of the fluids used. A converged solution will match an estimate of the temperatures with the thermophysical properties of the fluids at the average inlet and outlet temperatures.

It will be shown in a later chapter that the hundreds of choices available to the designer, can be, for the purpose of this project, be narrowed down to three.

1.7 Combustor design

Conventional combustors are designed to burn fuels in diffusion flames since the fuel and oxidizer (usually air) are not mixed. Prior to their introduction into the combustor, fuels are carried in tanks and are mixed with air brought in from ambient atmosphere in varying ratios as desired. The combustion zone is called the primary zone where the fuel is mixed with the air at a stoichiometric ratio (equivalence ratio $\phi = 1$).

In the combustion zone, aerodynamic mechanisms such as swirlers are used to cause reverse

flow by utilizing adverse pressure gradients created by sudden expansion and swirl (simultaneous axial-tangential flow). Reverse flow achieves two objectives: it locally reduces the speed of the fluid flow so that the flame may be stabilized. Measures to stabilize the flame are necessary since flame speeds (of the order of 3-4 m/s) are very much lower than typical fluid speeds (of the order of 100 m/s). Reverse flow also allows the turbulent mixing of hot products with cold reactants thus raising the temperature of the reactants and increasing the rate of the reaction according to the Arrhenius equation. In the secondary zone just downstream of the primary zone, the combustion of the gases are completed. Since the temperatures of combustion are much higher than that tolerated by the metallurgy of the turbine, more air is added in the dilution (or tertiary) stage downstream of the secondary zone in order to cool the products of combustion to a temperature suitable for the turbine.

Unconventional combustors, such as the lean burning combustor to be designed in this project, utilize a premixed mixture of methane and air in which the concentration of methane in the mixture is very low (of the order of 1-2%). It is not desirable to introduce more air or fuel into the system. This is because introduction of additional air makes the ultra-lean fuel-air mixture leaner and the introduction of more fuel defeats the purpose of design of an ultra-lean combustion system. Thus, the equivalence ratio ϕ must remain constant for the entire length of the combustor.

However, the provision for a region to stabilize the flame is imperative in the lean burning combustor as well. It is advantageous to design a region of stabilization of flame for this combustor similar to the swirler design used in conventional combustors since experimental data are available. Data usually correspond to isothermal or cold flow but can be approximately adapted to the combustion regime.

Compared to the large number of options available to the designer in the case of the heat

exchanger, the basic design choices for unconventional combustors are relatively few, the exact number being three. With the decision to incorporate a swirler in the design, the choice can be narrowed even more.

In Chapter 5, it will be shown that the combustor design cannot function simultaneously as a heat exchanger. Therefore, the entire load of heating the reactant stream must be borne by the heat exchanger.

1.8 Pivotal point: the perfectly stirred reactor model of the combustion zone

The region of the mixing of the products and reactants in the combustion can be modelled very effectively by means of a simplification - that the products and reactants are homogeneously mixed in the combustion zone and that the mixing time required to mix the product species with the reactant species to homogeneity is virtually zero. This means that the time for the conversion of the reactants to products is the time taken for the chemistry only. By dispensing with mixing time and assuming it being negligible, the modelled is greatly simplified since it is only needed to simulate chemistry and leave out a complicated array of aerodynamic parameters essential to estimate mixing time. Most practical combustion systems with the turbulent reverse flow mixing zone come close to this approximation and the tradeoff in computation reduction more than makes up for loss of accuracy. This model is called the Perfectly (or Well) Stirred Reactor model.

This simplified model can be safely said to be the pivotal point of the entire design process. In Chapter 2 this model is used to verify the constant flame temperature at all equivalence ratios of a fuel-air mixture. The predictions of this model are used to set the temperature limits of the heat exchanger, which are crucial to its design, one of the limits being the constant flame temperature.

1.9 Design integration

The purpose of this thesis is to provide a thermal design of the modified gas-turbine engine. With this objective, some important mechanical design issues will be addressed. These include size, pressure-drop and metallurgy constraints, as well as a conceptual idea of how the designed combustor and heat exchanger may be integrated with the essentially unmodified compressor and turbine to make a working unit. Some note may also be made of vibration analyses, especially in the case of the combustor, where combustor noise can be the cause of serious resonant oscillations. Recommendations will be made regarding the possibility of using supplementary fuel during startup or operation if the fuel quality is low. Since lean burning engines are increasingly assuming importance, future work including the development of a comprehensive package for the design of lean burning systems will be investigated.

1.10 Thesis Layout

The organization of this thesis almost corresponds to the major sections described above and comprises six chapters.

Chapter 2 describes the perfectly stirred model of the combustor and its results in detail. As mentioned in Section 1.8, the results from this model will be referenced to in the other chapters, and it is only logical that it be placed before any of the others.

Chapter 3 establishes the validity of the thermodynamic model of the engine cycle by comparing the original gas-turbine cycle efficiencies obtained from field data to those obtained theoretically utilizing a mixture of methane-air according to the predictions of this model. It also verifies the experimental observation of constant flame temperature at almost all equivalence ratios for a

methane-air mixture.

Chapter 4 describes the design of the heat exchanger utilizing the ϵ -NTU method. The hundreds of potential designs mentioned in Section 1.6 will be shown to logically and mathematically be narrowed down to three with the design charts presented for each type. A performance analysis of these three designs are also presented.

Chapter 5 describes the design of the combustor. It discusses the various basic options as well as modifications to some of the basic designs already existing. Based on these, as well as experimental and theoretical data, the combustor is designed. As in the case of the heat exchanger, a performance analysis will be done and it will be proved that the combustor cannot be used as part of the heat exchanger.

Chapter 6 describes the integration of the heat exchanger and combustor designs and summarizes the results and bounds within which the modified gas-turbine may be operated. It also mentions the future mechanical design necessary to translate the thermal design in this thesis into an operational system in the field. Some guidelines for the future work in the area of design of ultra-lean mixture systems are also presented.

Chapter 2

Perfectly Stirred Reactor model of the combustor

How many things by season seasoned are,
To their right praise and true perfection.

— *William Shakespeare(1564-1616 AD)* - The Merchant of Venice

The time it takes for the combustion of a fuel in a zone where the flame is stabilized is determined by the mixing time τ_{mix} and the reaction time τ_{rr} (Ref[4]). In a premixed combustor, the mixing time τ_{mix} is the minimum average time required for the products and reactants to mix in the combustion zone in order to insure that the temperature of the reactants is raised to the ignition temperature required for stable burning. The reaction time τ_{rr} is the minimum time required for the reaction to proceed to completion, i.e. the time required for the reactants to be completely burned to the products.

In practical combustion systems, combustion is highly turbulent. Turbulence rapidly mixes the burned and unburned gases in such a way that the flame essentially becomes a homogenous region

with a constant flame temperature (Ref[4]). Due to turbulence, and especially in lean mixtures, the time for mixing τ_{mix} becomes small compared to the time for the combustion reaction to take place τ_{rr} .

2.1 Perfectly Stirred Reactor model

An idealization of turbulent mixing and combustion is the Perfectly Stirred Reactor (PSR) model first developed in Ref[33]. Mixing of reactants and products is considered to be infinitely fast so that τ_{mix} is zero and reaction rates and times τ_{rr} are the only governing parameter. Computational modelling of the perfectly stirred reactor is relatively inexpensive (Ref[5]) and therefore there is considerable value in using this model to understand, design and predict the performance of some complex combustion problems.

The PSR model of the combustion zone is shown in Figure 2-1. Schematically, it is a chamber into which the reactants, a fuel-air mixture enters the chamber at bulk equivalence ratio ϕ , temperature T_3 (symbol T_3 has been chosen in order to be consistent with the combustor inlet temperature symbol used in subsequent chapters) and mass flux \dot{m} . The k th species in the reactant stream enters the chamber with a mole fraction Y_k^* and specific enthalpy h_k^* . Reactants and products in the chamber are assumed perfectly mixed with a homogenous composition at a final flame temperature T_4 (again symbol T_4 is chosen in order to be consistent with the symbol used for flame temperature in subsequent chapters). The product stream exhausts from the chamber at a bulk temperature T_4 , mass flow rate \dot{m} . The k th species in the product stream has a mole fraction Y_k and specific enthalpy h_k . The chamber may be also set up to admit a heat loss \dot{Q} from the reactor.

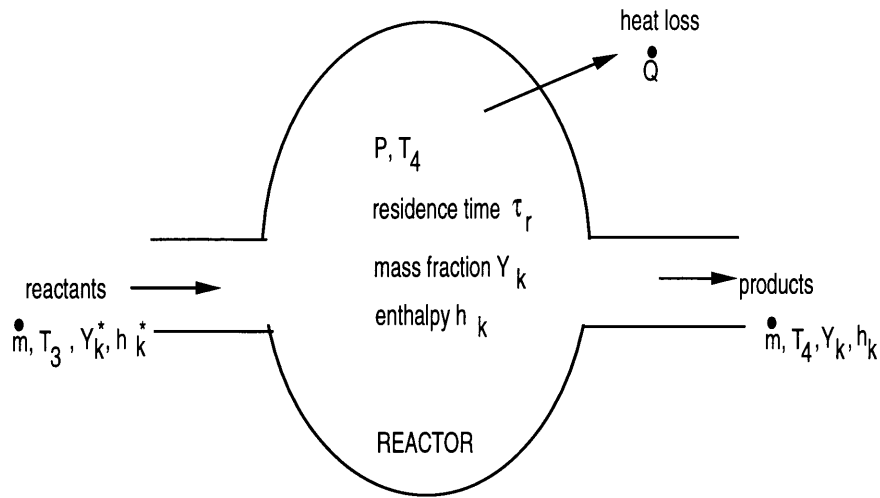


Figure 2-1: Schematic model of the Perfectly Stirred Reactor. Inlet conditions are \dot{m} , T_3 , Y_k^* , h_k^* . In the reactor, products of combustion mix perfectly with reactants. Conditions in the reactor chamber and product stream are \dot{m} , T_4 , Y_k , h_k . (Ref[5])

A simpler analysis of the PSR helps to gain an understanding of the dynamics in the model (Ref[4]). This analysis assumes that the combustion reaction within the reactor chamber may be approximated by a one step simple Arrhenius type reaction.

In this simpler analysis, energy balance states that the energy added to the flow across the reactor \dot{Q}_f :

$$\dot{Q}_f = \dot{m}c_p(T - T_3) \quad (2.1)$$

must be equal to the energy released by the simple one-step chemical reaction inside the reactor \dot{Q}_r :

$$\dot{Q}_r = V\Delta h_r \dot{w} = V\Delta h_r A_f \rho^n Y_f^n e^{-\frac{T_a}{T}} \quad (2.2)$$

where T = temperature in the combustor at an arbitrary time

c_p = the mass averaged specific heat at constant pressure

V = volume of the reactor

Δh_r = heat of reaction per unit mass of fuel and

\dot{w} = mass rate of fuel consumption

To reach the steady state in the reactor, equations 2.1 and 2.2 must be equal when $T = T_4$, the final burned gas temperature.

The solution in this simpler model is represented graphically in Figure 2-2 (Ref[4]). The straight lines correspond to \dot{Q}_f in equation 2.1. The slope of the line indicates the mass flow rate \dot{m} . Increased slope leads to increased \dot{m} in a linear manner.

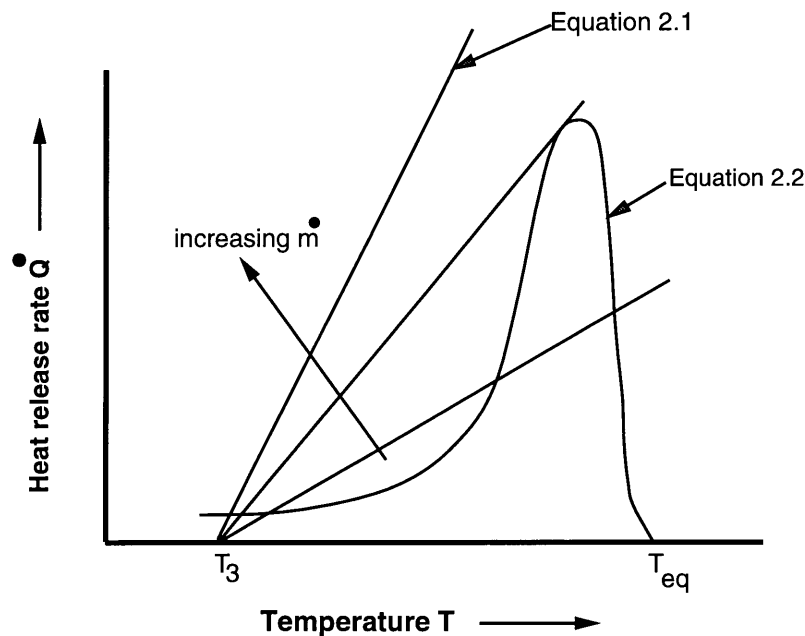


Figure 2-2: Solution to the simple model of the perfectly stirred reactor that involves simplification of the chemistry to a single equation. Slope of equation 2.1 gives \dot{m} and its intersection with equation 2.2 gives the solution for temperature (Ref[4])

In Figure 2-3, the effect of increasing inlet temperature while keeping the mass flow rate constant

can be seen. There are three conditions corresponding to T_3' , T_3 and T_3'' . When the inlet temperature is T_3' , the only solution is the cold solution close to T_3' . When the inlet temperature is T_3 , the straight line in equation 2.1 is tangent to the curve in equation 2.2. T_3 is then the minimum temperature required to insure a hot solution T_4 close to the equilibrium flame temperature T_f . When the inlet temperature is T_3'' , three solutions are obtained. One of them is a stable cold solution, the other unstable and the third is a stable hot solution as shown. However, for the purpose of the project, it is important to identify the minimum temperature required for stable burning. This temperature, T_3 is the least temperature to which the reactants need to be heated up to insure combustion in the reactor.

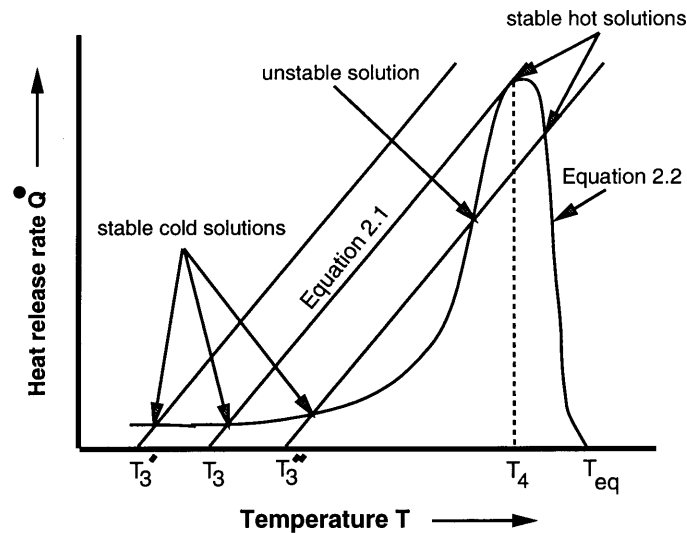


Figure 2-3: Effect of increasing inlet temperature to the reactor while keeping \dot{m} constant. The first hot solution is at temperature T_3 . Above T_3 , there is always a hot a solution

With detailed chemistry involving many intermediate reactions and time dependency, the equations for the perfectly stirred reactor model are as follows (Ref[5]):

Equation for mass conservation:

$$\dot{m}(Y_k - Y_k^*) - \dot{w}_k W_k V = -\rho V \frac{dY_k}{dt} \quad (2.3)$$

the equation for energy conservation:

$$\frac{dh}{dt} = c_p \frac{dT}{dt} + \sum_{k=1}^K h_k \frac{dY_k}{dt} \quad (2.4)$$

and the equation for the average residence time τ_r (explained shortly):

$$\tau_r = \frac{\rho V}{\dot{m}} \quad (2.5)$$

lead to a final equation which is solved numerically:

$$c_p \frac{dT}{dt} = \frac{1}{\tau_r} \sum_{k=1}^K Y_k^* (h_k^* - h_k) - \sum_{k=1}^K \frac{h_k \dot{w}_k W_k}{\rho} - \frac{\dot{Q}}{V} \quad (2.6)$$

where K = total number of species involved in the entire reaction

\dot{w}_k = molar rate of production by chemical reaction of the k th species

per unit volume

W_k = molecular weight of the k th species

\dot{Q} = reactor heat loss

τ_r = mean averaged residence time of a species in the reactor. This is the average minimum time that the gas must spend in the reactor chamber to be completely burnt. In the idealized model, the time for the reaction

τ_{rr} is the only governing parameter and this time may be interpreted as the average minimum time that the reactants need to spend in the reactor in order that chemistry may proceed to completion. By equality in definition, this is the same as τ_r .

The other symbols have the same meaning as shown in Figure 2-1.

2.2 Numerics

The SANDIA PSR utility numerically implements equation 2.6 by using the damped Newton's method (Ref[5]). It calculates the final temperature of combustion in the reactor, T_4 and the product composition Y_k (shown in Figure 2-3) based on the inlet temperature of the reactants to the reactor chamber T_3 (see Figure 2-3), mean mass flow rate \dot{m} , inlet composition of reactants Y_k^* , volume of the reactor chamber V and a database of chemical reactions describing the combustion of a particular fuel.

2.3 Results and predictions of the perfectly stirred reactor model

Figure 2-4 shows the variation of minimum inlet temperature required for combustion T_3 with the volume V of the reactor for a range of equivalence ratios ϕ of a fuel-oxidizer mixture of methane-air. The mass flow rate \dot{m} is kept constant ($= 2.32$ kg/s from Ref[23]).

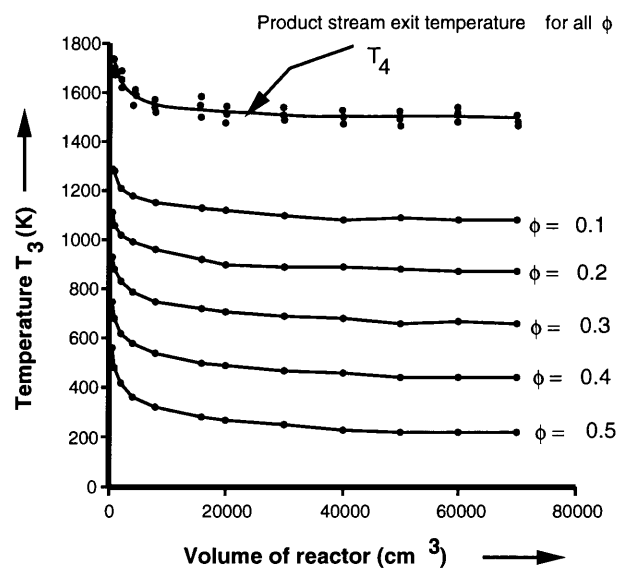


Figure 2-4: Variation of T_3 against V for a constant \dot{m} for a CH_4 -air mixture. Product stream temperature T_4 is constant for all ϕ

Figure 2-5 explains the curves shown in Figure 2-4. The curve is the locus of the minimum temperature required in the reactor in order that stable combustion may be achieved given an equivalence ratio ϕ of a particular fuel-oxidiser mixture and the mass flow rate \dot{m} . The region above the curve shows complete burning (or a hot solution in the sense of Figure 2-3) and the region below the curve shows no burning (or a cold solution in the sense of Figure 2-3). It can be seen that for small volumes, T_3 , the minimum temperature required to insure complete burning in the reactor increases sharply. This T_3 rise is related to the minimum time τ_r required for the chemistry to proceed to completion, which, in turn, is governed by the reaction rate. According to the basic Arrhenius equation of chemical reactions, reaction rate increases exponentially with temperature and therefore required τ_r decreases exponentially. Thus, at small volumes, it is possible to insure combustion in the reactor simply by raising T_3 exponentially. At large volumes of the reactor, however, the minimum τ_r is already provided and further increase in V , and thus in τ_r ,

(the relation between V and τ_r is given by equation 2.5) does not appreciably decrease T_3 due to the Arrhenius equation dependence. Therefore, the curve approaches an asymptotic value. Hence, it can be concluded that for a given ϕ and \dot{m} of a particular type of fuel, and provided sufficient average residence time is allowed, there is a unique value of T_3 for complete combustion.

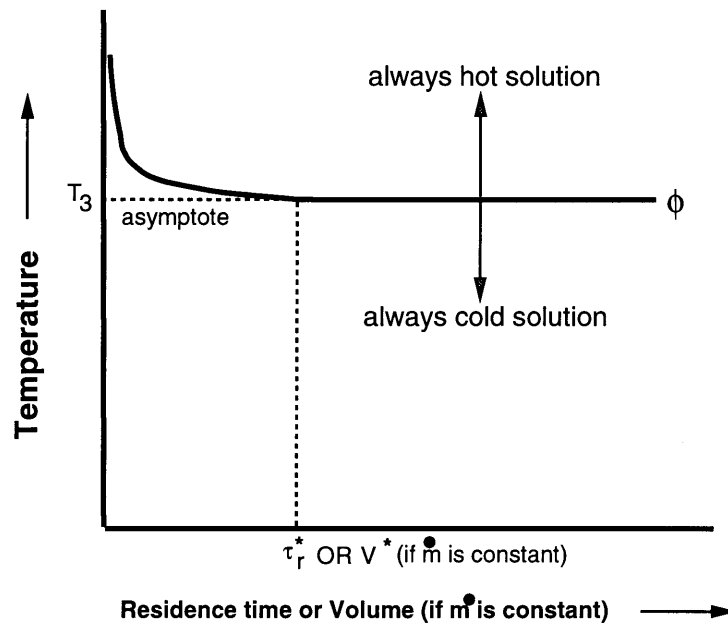


Figure 2-5: Variation of T_3 against τ_r or V (if \dot{m} is kept constant for some arbitrary ϕ and for some fuel-oxidiser mixture. Note that there is an asymptotic T_3 . Also note a τ_r^* (or a V^*) value beyond which T_3 does not decrease significantly

Figure 2-5 also shows that, whatever be the resulting final geometry of the reactor, (or in the practical sense, the combustor), there is no significant gain when the reactor volume V is increased beyond a certain V^* . V^* automatically limits the size of the reactor needed for a particular type of fuel-oxidiser mixture. This is because the curves decrease exponentially very quickly. As can be seen, for $\dot{m} = 2.32 \text{ kg/s}$, $V^* = 20000 \text{ cm}^3$ appears to be universal for all ranges of ϕ for a methane-air mixture.

Note that the variation of V in Figure 2-4 may be equivalently expressed as a variation in τ_r , since V , τ_r and \dot{m} are related by equation 2.5. This has been shown in Figure 2-5. Hence, if \dot{m} is kept constant, V^* would correspond to τ_r^* .

From Figure 2-4, we can also see that the final temperature of the product stream T_4 is roughly a constant provided sufficient residence time τ_r is provided. For a mixture of methane-air, $T_4 \approx 1500$ K.

Figure 2-6 shows the variation of T_3 with respect to equivalence ratio ϕ of the methane-air mixture for $\dot{m} = 2.32$ kg/s. We can see that this variation is almost linear and may be written as:

$$T_3 = 1295 - 2150\phi \quad (2.7)$$

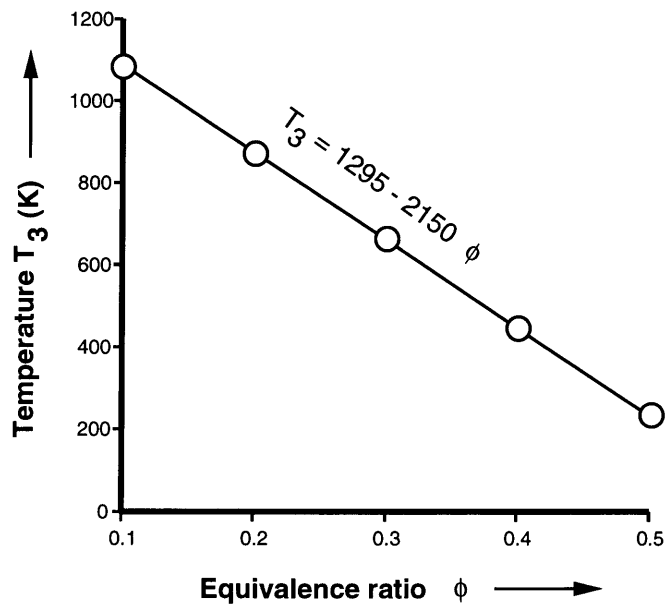


Figure 2-6: Variation of inlet temperature to reactor T_3 with equivalence ratio ϕ for a CH_4 -air mixture. This variation is linear

2.4 Summary

As mentioned before, although the perfectly stirred model of the combustor is an idealized assumption, most practical combustion systems perform close to the predictions of this model. The two conclusions obtained from Figures 2-4 and 2-5 are therefore powerful tools that can be used in the design combustors for which the assumption of a perfectly stirred reactor are valid. For clarity, these conclusions are summarized:

- (a) For a particular type of fuel-oxidiser mixture, there is a unique asymptotic value of T_3 associated with a value of ϕ provided sufficient τ_r is allowed.
- (b) For a particular type of fuel-oxidiser mixture, there is an average residence time τ_r^* (or volume V^* if \dot{m} is constant) beyond which there is no significant gain in reduction in T_3 . This τ_r^* (or V^*) is universal over all ranges of ϕ for that mixture.
- (c) For a particular type of fuel-oxidizer mixture, regardless of what the value of ϕ and provided the residence time is at least τ_r^* , the final combustion temperature T_4 is approximately constant.

The specific results from Figure 2-4, 2-6 and the conclusions above will be used in the design of the heat exchanger and the combustor in subsequent chapters. The validity of data from Figures 2-4 and 2-6 are examined in the next chapter.

Chapter 3

Cycle Calculations for the GS-350

All things from eternity are of like form,
And come around in a circle.

— *Marcus Aurelius Antonius(121-180 AD)* - Meditations

This chapter describes the Brayton gas-turbine cycle on which the performance of the GS-350 is based and the modification necessary to include recuperation to insure burning of very low BTU fuels such as a methane-air mixture. The performance of this modified cycle, called the Recuperative Brayton cycle, is predicted and compared with equivalent field data.

3.1 Air-standard ideal Brayton Cycle

The Brayton Cycle, also called the Joule Cycle, was developed originally for use in a piston engine with fuel injection, but its most common embodiment is in open and closed-cycle gas turbine engines.

The fuel-air cycle (or the open cycle) of a simple gas-turbine power plant is shown in Figure 3-1. Air at state 1 is compressed to state 2 by the compressor expending work W_c . Fuel is added to

the air at state 2 in the combustor and the resulting mixture is burned in the combustor resulting in the chemical release of heat \dot{Q} . The products of combustion at the exit of the combustor at state 3 are expanded in the turbine to state 4 resulting in gross work output of the turbine W_t . W_c part of this gross work is used to compress air in the compressor. Hence the useful work output of the gas-turbine system is $W_{net} = W_t - W_c$.

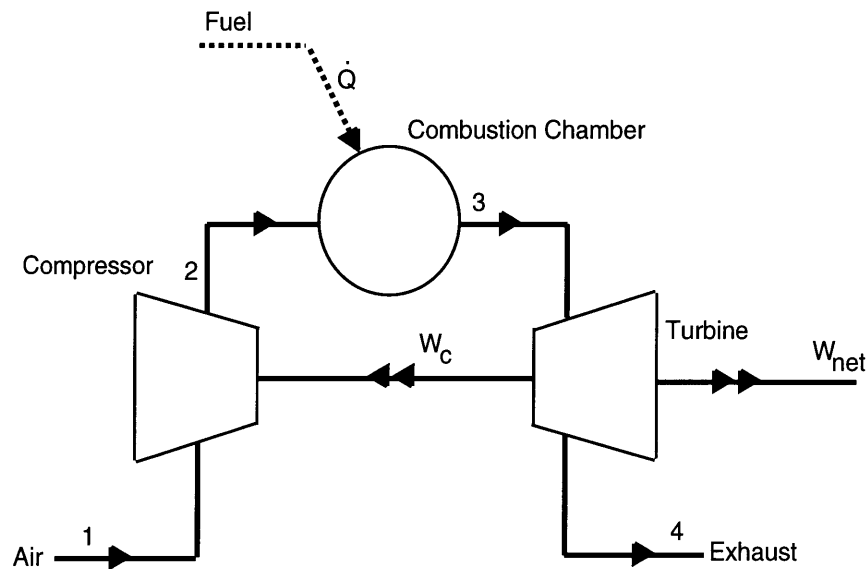


Figure 3-1: Fuel-Air or Open Cycle of a simple gas-turbine power plant
 Air at state 1 is compressed to state 2. Fuel is added in the combustor and mixture is burned. Products of combustion at state 3 are expanded in the turbine to state 4 resulting in net useful work W_{net}

Since the actual working fluids do not go through a complete thermodynamic cycle in the gas-turbine, it is advantageous to devise a closed cycle that closely approximates the open cycle. This approach leads to the air-standard cycle for the gas-turbine (Ref[10]) shown in Figure 3-2 where the working fluid, approximated as air, is considered as a fixed mass of an ideal gas throughout the entire cycle. The ideal cycle approximates the compression and expansion processes to be isentropic

(i.e. no loss of reversibility). The combustion process in the air-standard cycle is modelled as heat transfer to the working fluid in the combustor from an external source and the cycle is completed by heat transfer to the surroundings (in contrast to the intake and exhaust processes of an actual engine).

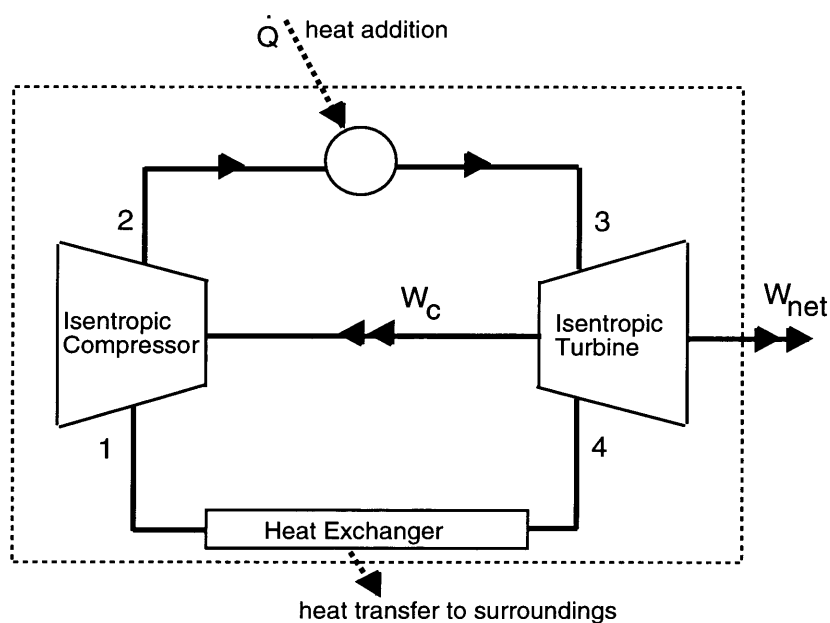


Figure 3-2: Schematic of Air-standard Ideal Brayton Cycle. Working fluid is approximated as an ideal gas with properties of air. The gas undergoes two heat transfer processes separated by isentropic compression and expansion processes (Ref[10])

The T-S diagram of the air-standard Brayton Cycle for an ideal simple gas-turbine is shown in Figure 3-3 (Ref[10]). This cycle is composed of constant pressure heat transfer processes (corresponding to external heat addition and heat transfer to the surroundings) separated by isentropic compression and expansion processes.

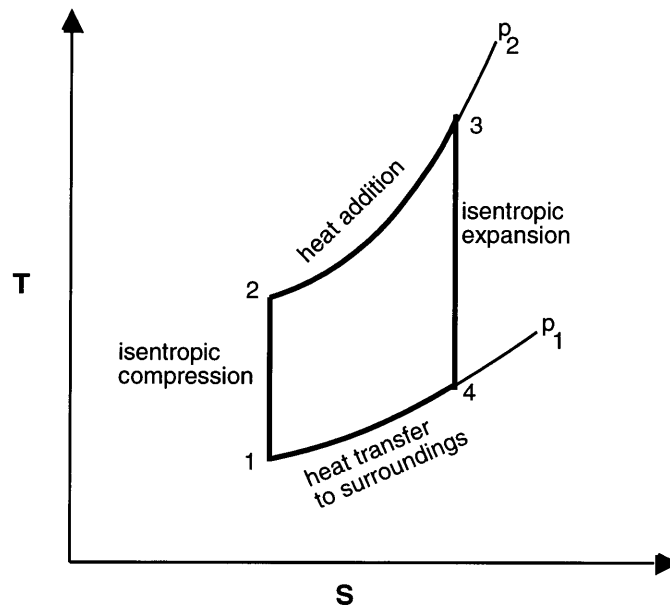


Figure 3-3: T-S diagram of the air-standard ideal Brayton cycle. Two constant pressure heat transfer processes are separated by isentropic compression and expansion processes (Ref[10])

3.2 Air Standard ideal Recuperative Brayton Cycle

For the purpose of this project, the working fluid is a very low concentration mixture of methane (CH_4) in air. In order for this mixture to burn in the combustor, it must be raised to a sufficiently high temperature that is usually greater than the temperature attained by isentropic compression (Figure 2-6), it is necessary to provide a heat exchanger after the compression stage and before the combustor so that the reactant stream may be heated by exchanging excess enthalpy from the hot product stream. This is shown in Figure 3-4. The gas mixture is at ambient temperature T_1 at the intake of the compressor. Compression raises it to a temperature T_2 . To ensure burning in a lean combustion model, however, it must be raised further to a temperature T_3 by means of a heat exchanger that transfers the excess enthalpy of the hot product stream at temperature T_4 to the relatively cold reacting stream at temperature T_2 . The hot product stream enters the

turbine at temperature T_5 . Gross work W_t is produced from the turbine when the gas is allowed to expand resulting in a lower exhaust temperature T_6 . A part of this gross work is used as back work W_c to compress the reactants in the compressor. The net useful work output from the ideal gas turbine system W_{net} is the difference of W_t and W_c . This is the Recuperative Brayton Cycle. The corresponding $T - S$ diagram for the ideal recuperative gas-turbine cycle is shown in Figure 3-5.

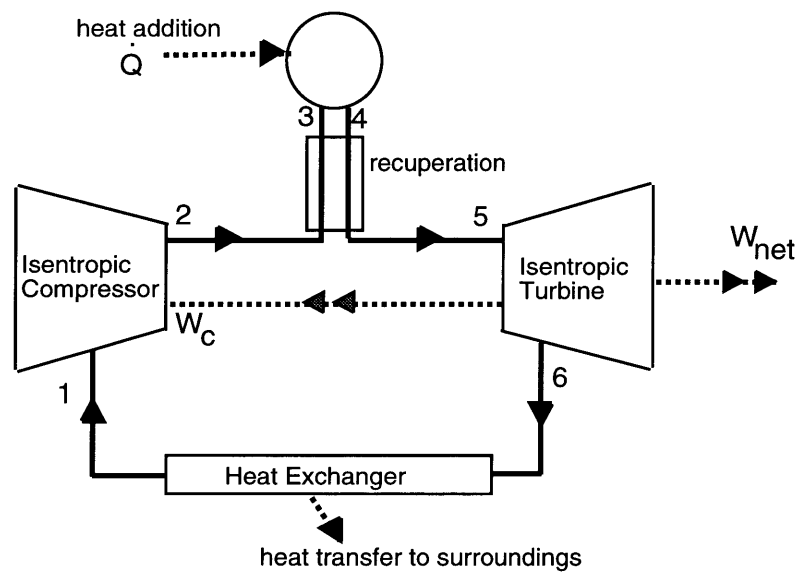


Figure 3-4: Recuperative Brayton cycle. Temperature of the reactants at T_2 are raised to a higher temperature T_3 (which is the minimum required for ignition in the combustor) by means of heat transfer from hot products at T_4

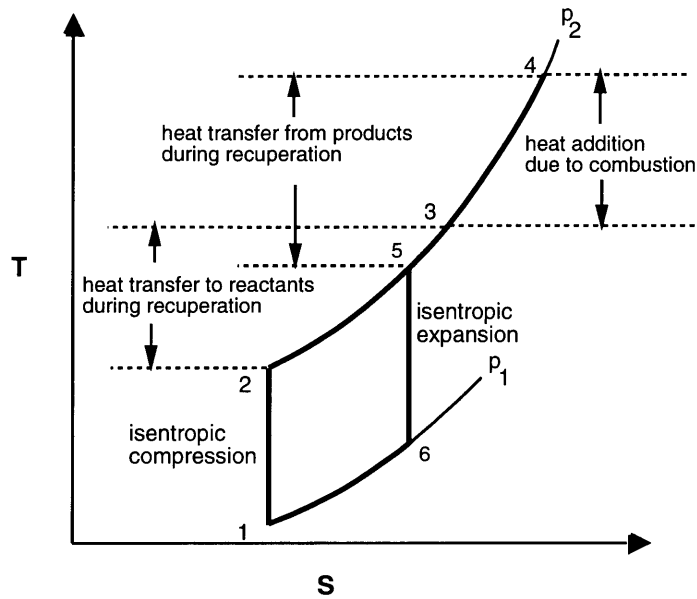


Figure 3-5: T-S diagram of the Recuperative Brayton cycle. 4-5 is heat transfer from hot product stream to cold reactant stream. 2-3 is the enthalpy increase of the cold reactant stream due to this heat transfer

3.3 Ideal Cycle Efficiencies

The ideal efficiency η for any thermodynamic cycle is defined as (Ref[10]):

$$\eta = \frac{\text{useful work output}}{\text{total energy supplied}}$$

For the simple ideal Brayton cycle, η (Ref[10]) is:

$$\eta = 1 - \left(\frac{1}{r_p} \right)^{\frac{k-1}{k}} \quad (3.1)$$

where r_p = pressure ratio in the compressor or in the turbine and

k = ratio of specific heats of the gas viz. $\frac{c_p}{c_v}$

In the case of the ideal recuperative air-standard Brayton cycle, cycle efficiency η_r can be similarly derived (see Appendix 1) as:

$$\eta_r = 1 - \left(\frac{1}{r_p} \right)^{\frac{k-1}{k}} \quad (3.2)$$

where the symbols have the same meaning.

It can be seen from equations 3.1 and 3.2 that ideal cycle efficiencies for the simple and recuperative Brayton cycles are the same. An acceptable value for $k = 1.4$ and for the GS-350, the pressure ratio $r_p = 4.0$. Hence the ideal cycle efficiency for the air-standard Recuperative Brayton cycle from equation 3.2 is:

$$\eta_r = 0.33 \quad (3.3)$$

3.4 Actual Overall gas-turbine Efficiency

Real compressors and turbines, are, of course, not isentropic as shown in Figures 3-3 and 3-5. There is some loss of reversibility in both compression and expansion in the compressor and turbine respectively. This may be due to heat loss to the surroundings as well as fluid friction losses within the compressor and turbine stage(s). This has been shown as the dotted lines in Figure 3-6.

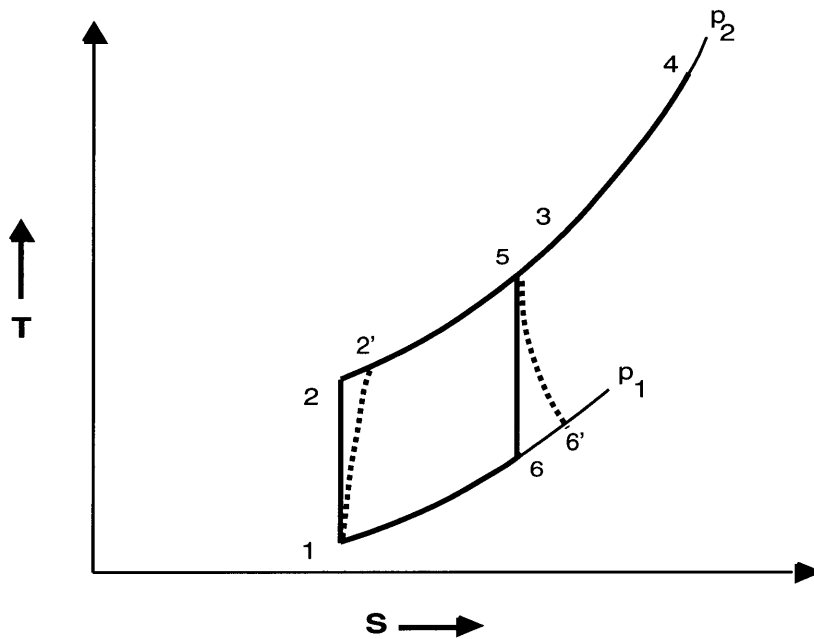


Figure 3-6: Effect of irreversibility in the components of the gas-turbine shown schematically by means of dotted lines on the ideal cycle shown in Figure 3-5. Actual cycle is 12'3456'

3.4.1 Compressor efficiencies η_{cad} , η_{pc} and compression work W_c

The *adiabatic* efficiency of a compressor η_{cad} is defined as the ratio of the adiabatic isentropic work H_{ad} required to compress the fluid to the actual work W_c done in the compression (Ref[15]). The general isentropic process is of the form (Ref[9]):

$$PV^k = \text{constant} \quad (3.4)$$

where P is the pressure of the gas at any given state,

V is the volume of the gas at that state and

k is the ratio of the specific heats as defined earlier.

The *polytropic* efficiency of a compressor η_{pc} is defined as the ratio of the polytropic work required H_{pc} to compress the fluid to the actual work W_c done during compression (Ref[15]). The polytropic process is a variable entropy process in which heat transfer and friction can take place. Therefore, the isentropic process described by equation 3.4 is actually a special case of the polytropic process. The general polytropic process is of the form (Ref[9]):

$$PV^n = \text{constant} \quad (3.5)$$

where n is the polytropic coefficient and the other symbols have the same meaning.

The polytropic head work H_{pc} done in compressing a gas can be derived as (see Appendix 1):

$$H_{pc} = RT_1 \frac{n}{n-1} \left[r_p^{\frac{n-1}{n}} - 1 \right] \text{ kJ/kg} \quad (3.6)$$

where R is the gas constant and the other symbols have their usual meaning.

The actual work W_c may be simply derived as a difference of enthalpies of the gas after and before compression (see Appendix 1) as:

$$W_c = \Delta h_{1-2} = RT_1 \frac{k}{k-1} (r_p^{\frac{n-1}{n}} - 1) \text{ kJ/kg} \quad (3.7)$$

Thus we may derive the relation between k , n and η_{pc} from equations 3.6 and 3.7 as:

$$\frac{n}{n-1} = \frac{k}{k-1} \eta_{pc} \quad (3.8)$$

since by definition, W_c is defined as (Ref[15]):

$$W_c = \frac{H_{pc}}{\eta_{pc}} \quad (3.9)$$

From equation 3.8 it can be seen that the polytropic efficiency η_{pc} is independent of the thermodynamic state of the gas undergoing compression including temperature, pressure or molecular weight. This is a powerful result for design and analysis and as a result, manufacturers tabulate polytropic efficiencies for classes of compressor frames against flow rate.

The compressor used in the GS-350 is a single-stage centrifugal unit. Table 3-1 shows a tabulation of centrifugal compressor frame polytropic efficiencies against classes of volume flow rates (Ref[15]) In the case of the GS-350, the volume flow rate is $\dot{V} = \frac{\dot{m}}{\rho} = 8352 \text{ m}^3/\text{hr}$

where $\dot{m} = 2.32 \text{ kg/s}$ is the mass flow rate from Ref[1] and

$\rho = 1.0 \text{ kg/m}^3$ is the density at the intake temperature of 300K and

ambient pressure of 1 atm.

Table 3-1: Centrifugal Compressor Polytropic Efficiencies (from Ref[15])

Frame	Inlet Volume Flow (m ³ /hr)	Polytropic Efficiency η_{pc}
A	1300-12000	0.76
B	10000-31000	0.76
C	22000-53000	0.77
D	39000-75000	0.77
E	56000-110000	0.78
F	82000 - 170000	0.78

It can be easily inferred from Table 3-1 that the compressor flow rate of the GS-350 corresponds to type Frame A and therefore:

$$\eta_{pc} = 0.76 \quad (3.10)$$

Using equations 3.5 to 3.10, the iterative procedure of converging to definite values of temperature at exit of the compressor T_2 , polytropic head work required H_{pc} and power required to compress the gas W_c have been performed. The results are summarized below:

$$H_{pc} = 158.1 \text{ kJ/kg}$$

$$W_c = 482.6 \text{ kW}$$

$$T_2 = 501.4 \text{ K}$$

Additionally, we may obtain the adiabatic efficiency η_{cad} in terms of polytropic efficiency η_{pc} and the the pressure ratio r_p as (see Appendix 1)

$$\eta_{cad} = \frac{r_p^{\frac{k-1}{k}} - 1}{r_p^{\frac{k-1}{\eta_{pc}k}} - 1} \quad (3.11)$$

Therefore, for the GS-350 we obtain also:

$$\eta_{cad} = 0.71 \quad (3.12)$$

3.4.2 Turbine efficiencies η_{tad} , η_{pt} and turbine work W_t

Figure 3-7 reproduces the variation of adiabatic turbine efficiency η_{tad} from Ref[34], (which is defined as the ratio of the actual work output of the turbine to the adiabatic, isentropic work output) to the pressure ratio r_p .

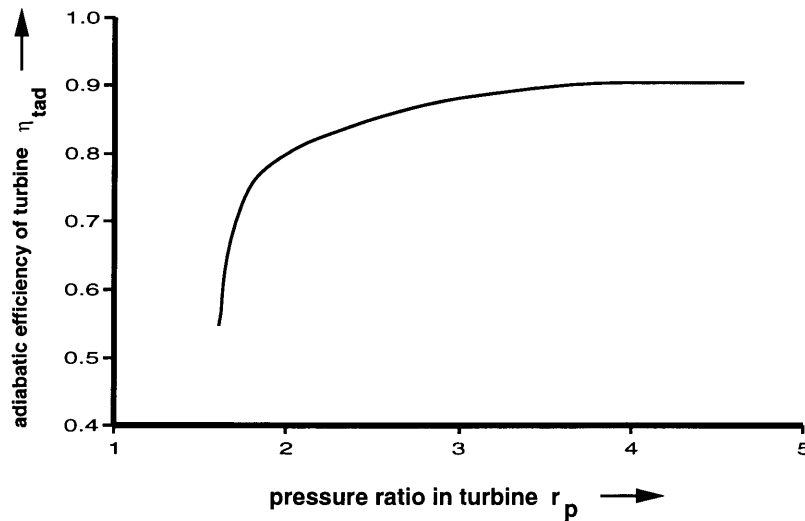


Figure 3-7: Variation of isentropic efficiency η_{tad} as a function of pressure ratio r_p in a turbine. η_{tad} is virtually constant for a large range of r_p (Ref[32])

For $r_p = 4.0$ it can be easily seen that:

$$\eta_{tad} = 0.9. \quad (3.13)$$

The relation between the polytropic efficiency of the turbine η_{pt} (defined as the ratio of the actual work output of the turbine to the polytropic work output upon expansion in the turbine) can be derived similar to that in Section 3.4.1 and is almost identical to equation 3.11:

$$\eta_{tad} = \frac{r_p^{\frac{k-1}{k}} - 1}{r_p^{\frac{k-1}{\eta_{pt}k}} - 1} \quad (3.14)$$

Using the ideal gas adiabatic isentropic value of $k = 1.4$ and with $r_p = 4.0$, the polytropic efficiency of the turbine is:

$$\eta_{pt} = 0.88 \quad (3.15)$$

The value of the polytropic coefficient n can be found from the relation in equation 3.8, which can be derived as identical to both compressor and turbines as:

$$\frac{n}{n-1} = \frac{k}{k-1} \eta_{pt} \quad (3.16)$$

In a manner similar to that used in Section 3.4.1, the turbine polytropic head work H_{pt} of the expanding gas may be derived:

$$H_{pt} = RT_5 \frac{n}{n-1} \left[r_p^{\frac{n-1}{n}} - 1 \right] \text{kJ/kg} \quad (3.17)$$

where T_5 is the turbine inlet temperature as shown in Figures 3-4 and 3-5 and other symbols have the same meanings. If the heat transfer from the hot products to the cold reactants in the recuperative cycle (Figure 3-4) is assumed perfect and the specific heats equal ($c_{pp} = c_{pr}$), then approximately:

$$T_5 = T_4 - (T_3 - T_2) \quad (3.18)$$

where T_2 = temperature at the exit of the compressor = 501.4 K

T_3 = the minimum temperature required to burn the fuel-air mixture

obtainable from Figure 2-2 and therefore depends on equivalence ratio ϕ

T_4 = burnt gas temperature independent of ϕ and is around 1500 K

Figure 3-8 shows the variation of T_5 against ϕ . As can be seen, this variation is almost linear and can be written as:

$$T_5 = 2100\phi + 710 \quad (3.19)$$

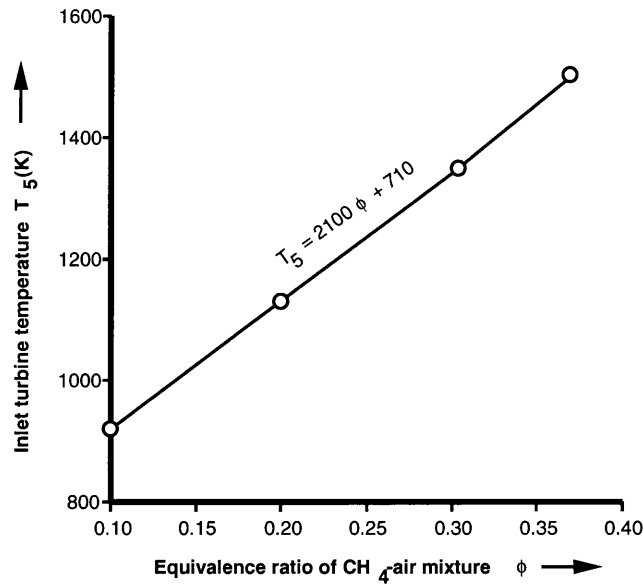


Figure 3-8: Plot of turbine inlet temperature T_5 as a function of equivalence ratio ϕ

The gross actual work output W_t of the turbine can be derived similar as in Section 3.4.1 as:

$$W_t = RT_5 \frac{k}{k-1} (r_p^{\frac{n-1}{n}} - 1) \quad (3.20)$$

where the symbols have their usual meaning.

Figure 3-9 shows the variation of the net useful power output, W_{net} ($= W_t - W_c$) with equivalence ratio ϕ of the mixture. This has been derived by iterative calculations using equations 3.5 to 3.20. Superimposed on the theoretical data are data from the setup of the GS-350 gas-turbine in the field. While interpreting the field data, note that ϕ is the concentration of the methane-air mixture equivalent of diesel fuel that would produce the same power output.

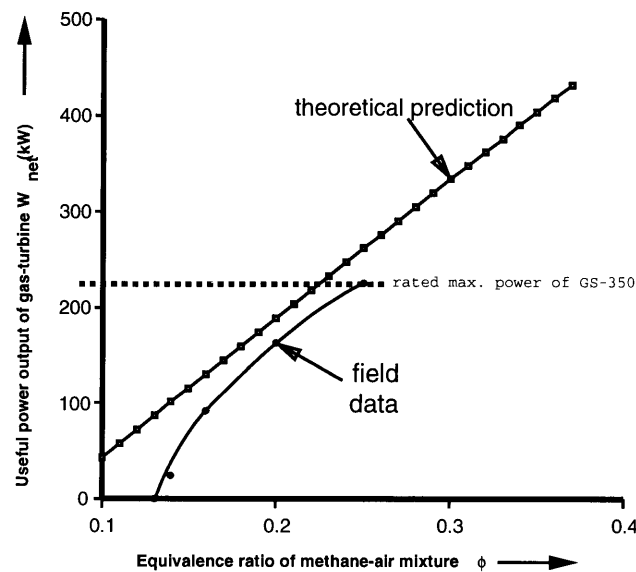


Figure 3-9: Plot of net useful power output W_{net} predicted and from field data (Ref[21]) as a function of CH_4 -air mixture equivalence ratio ϕ

It can be seen from Figure 3-9 that the experimental data from the field are always less than the theoretical results. This is to be expected since mechanical losses have not been taken into account, which are significant considering that the GS-350 is a scrap gas-turbine brought back into trial operation. Also note that the difference between the theoretical and field data reduce as the power output approaches the rated maximum of 225 kW. This is also expected since a gas-turbine is designed to be most efficient at the rated power output.

From Figure 3-9, it can be also inferred that in order to produce the rated maximum power output of 225kW from the GS-350, ϕ of the methane-air mixture need be only slightly above 0.2.

3.4.3 Overall gas-turbine efficiency η

The Exothermic Energy Yield (ψ) of a fuel-air mixture, which can be defined as the theoretical maximum energy yield upon complete combustion of a unit mass of fuel-air mixture, may be derived

from the definition and value of the Lower Heating Value (LHV) of the fuel. For methane, LHV = 50MJ/kg of fuel (Ref[9]). For a mixture of $\beta\%$ methane in air by volume, the ψ can be easily derived (see Appendix 1) as:

$$\psi = \frac{8 \times 10^5 \beta}{16\beta + 28.96(100 - \beta)} \text{KJ/kg of CH}_4\text{-air mixture} \quad (3.21)$$

Note that the relation between percentage volume concentration of methane in a methane-air mixture β and the equivalence ratio of the same mixture ϕ may be written without much loss of accuracy as (see Appendix 1):

$$\phi = \frac{\beta}{10} \quad (3.22)$$

The theoretical maximum rate of heat addition Δh can be then written as:

$$\Delta h = \dot{m}\psi \text{ kW} \quad (3.23)$$

Thus, it is easy to see that the overall efficiency of the gas-turbine η , defined as the ratio of the net useful work done W_{net} to the chemical rate of heat addition Δh can be written as:

$$\eta = \frac{W_{net}}{\Delta h} \quad (3.24)$$

Since both W_{net} and Δh are functions of equivalence ratio ϕ , which in turn depends on β according to equation 3.21, the variation of η can be found as a function of volume percent of methane in air, β .

Figure 3-10 shows this variation. Superimposed on the theoretical data are data from the field.

Note that in the case of the field data, β is the volume percentage concentration of methane in a methane-air mixture equivalent to the diesel used for the same overall efficiency η .

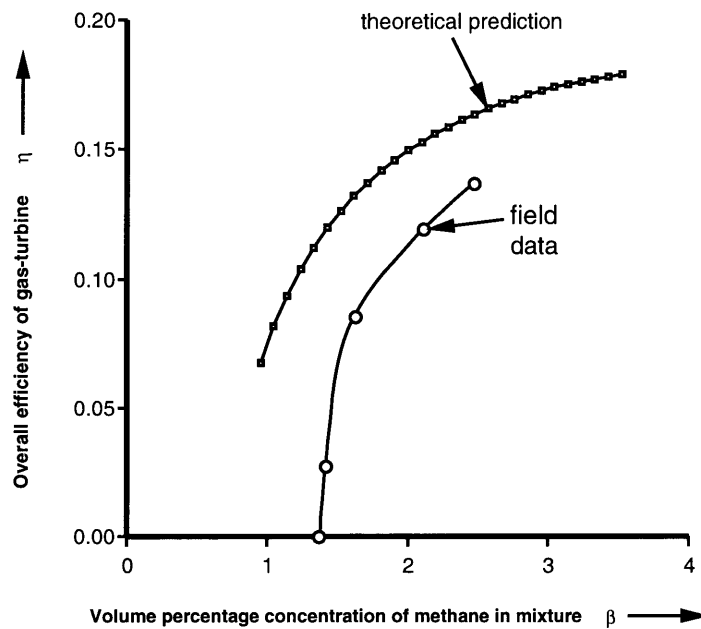


Figure 3-10: Variation of overall efficiency η of the gas-turbine as a function of percentage volume concentration of CH_4 in a mixture of CH_4 -air.

Again, it may be noted from Figure 3-10 that the theoretical efficiency is greater than the actual efficiency of the GS-350 operating in the field for the same reasons as mentioned in Section 3.4.2.

Figure 3-11 shows the variation of W_{net} against η . Superimposed are the field data for the GS-350. It can be seen that the theoretical predictions closely match the values obtained from the field data. It can also be seen that for a given power output, the actual gas-turbine efficiency is lower than that predicted, which also are due to the reasons mentioned in Section 3.4.2.

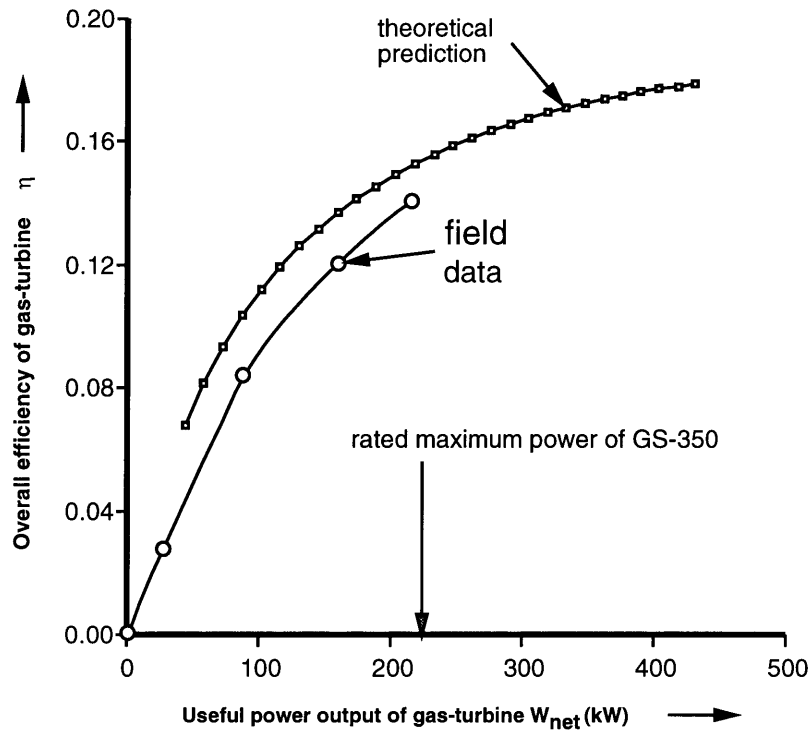


Figure 3-11: Variation of W_{net} as a function of overall efficiency η

Note that in Figures 3-9 and 3-11, the theoretical predictions are redundant after the point marked as the “maximum power output of GS-350” since maximum achievable W_{net} is 225 kW from the GS-350 gas-turbine (hence they are valid for simple gas-turbines that are designed for higher power outputs). It is theoretically possible to get a higher W_{net} beyond this point, but for the practical system GS-350, that would mean extending the performance beyond the design limits and possibly compromising system life and/or safety issues.

A reasonable agreement of field data with theoretical predictions of performance can be seen in Figures 3-9 to 3-11. Since the results in these figures are obtained by using Figure 2-2, they prove its validity. As mentioned in Chapter 2, Figure 2-2 will be an important guideline in subsequent designs of the recuperative heat exchanger as well as the combustor shown in Figure 3-4.

Chapter 4

Heat Exchanger Design

Energy is eternal delight!

— *William Blake(1757-1827 AD)* - Voice of the Devil

As mentioned in Chapter 1 and as shown in Figure 3-4, the temperature of the reactant stream at the exit of the compressor T_2 is usually insufficient to insure ignition of the gases in the combustor. This is because there is a minimum temperature T_3 , that depends on equivalence ratio ϕ of the fuel-oxidizer mixture (such as Figure 2-6 for a methane-air mixture), below which the mixture will not burn (see Figure 2-5). For most values of ϕ , T_3 is greater than T_2 , necessitating the requirement of a heat exchanger by means of which the hot products may give up some of their enthalpy to the cold reactants to raise them to T_3 (see Figures 1-3 and 3-4). The design of this heat exchanger is the objective of this chapter.

Figure 4-1 (Ref[11]) shows the general methodology for heat exchanger design. Mechanical design of the heat exchanger, being beyond the scope of this thesis, will not be attempted. Thus the resulting design(s) of the heat exchanger will be optimized for heat transfer and pressure drop

only.

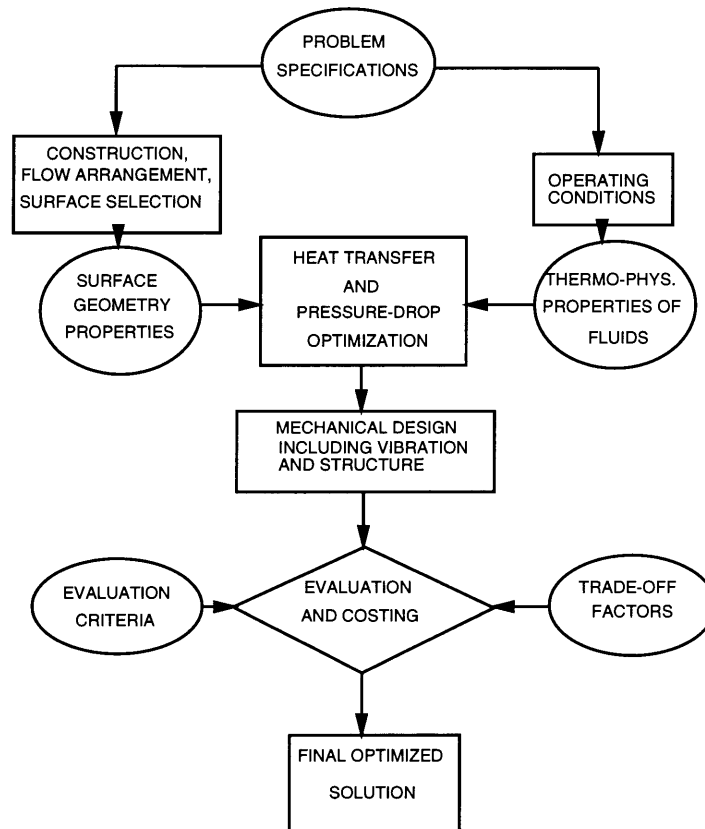


Figure 4-1: Methodology of heat exchanger design (Ref[11])

The primary goal of the heat exchanger is to provide means by which a hot fluid may give up some of its heat to a cold fluid. This may be done either by *mixing* the hot and cold fluids or by providing a *surface* made of metal or ceramic which interacts with the two fluids and enhances the heat transfer through increased surface area by convection and/or radiation.

In the former case, if hot burned products and cold reactants are allowed to mix, the concentration of the reactants is inherently diluted by product species. The chemical reaction rate, as

shown in Figure 1-3, may be thus adversely affected by this dilution (this is more pronounced since the reactant stream is itself a low concentration mixture of fuel-oxidizer).

Therefore, a surface must be provided by means of which heat transfer may take place between the hot products and cold reactants. In general, the greater this heat transfer surface area, the greater is the enthalpy exchanged between the two streams.

In practical systems, this surface area must be constrained within a finite volume since the heat exchanger itself cannot be unrestricted in size. In other words, the heat exchanger must be made *compact*. When a heat exchanger is made compact, the passage-ways available for the fluid flow become narrower as the surface area is increased resulting in increased friction between the fluid and the heat transfer area. Fluid friction manifests itself as a *pressure loss* between the inlet and outlet of the heat exchanger.

Hence the design of the heat exchanger is an optimization problem between increasing the area of the heat transfer surface A_h and simultaneously decreasing the pressure loss ΔP .

4.1 Performance criterion for the heat exchanger

A performance criterion has been defined, based on the above two parameters. A heat exchanger is defined to satisfactorily perform if:

1. it meets the needs of the surface area A_h for the desired heat transfer while satisfying that this surface area be contained within a volume that is limited by practical size constraints.

A good general rule is that no dimension of the heat exchanger must be greater than 1 m.

2. the pressure loss ΔP is within bounds. Typically, for heat exchangers used in gas-turbines, an acceptable limit for ΔP is 8% based on the inlet pressure of the fluid to the heat exchanger

(Ref[22]).

4.2 Heat transfer algorithm for compact heat exchanger design: the ϵ -NTU method

The heat transfer design and pressure drop analysis for compact heat exchangers were first fully developed in Ref[12] and the principles are briefly explained here. The major assumption used in this development is that thermodynamic properties of each fluid in the heat exchanger may be considered as the average of properties at the inlet and outlet of the heat exchanger. This is within the bounds of acceptable error if the heat exchanger is compact.

In Figure 4-2, the schematic representations of a heat exchanger in both parallel flow and counterflow configurations are seen. Inlet and outlet temperatures for the cold fluid correspond to T_{ci} and T_{co} . From Figure 3-4, it can be seen that these temperatures are the same as T_2 and T_3 respectively. Similarly the inlet and outlet temperatures for the hot fluid correspond to T_{hi} and T_{ho} and from Figure 3-4, these temperatures are the same as T_4 and T_5 respectively.

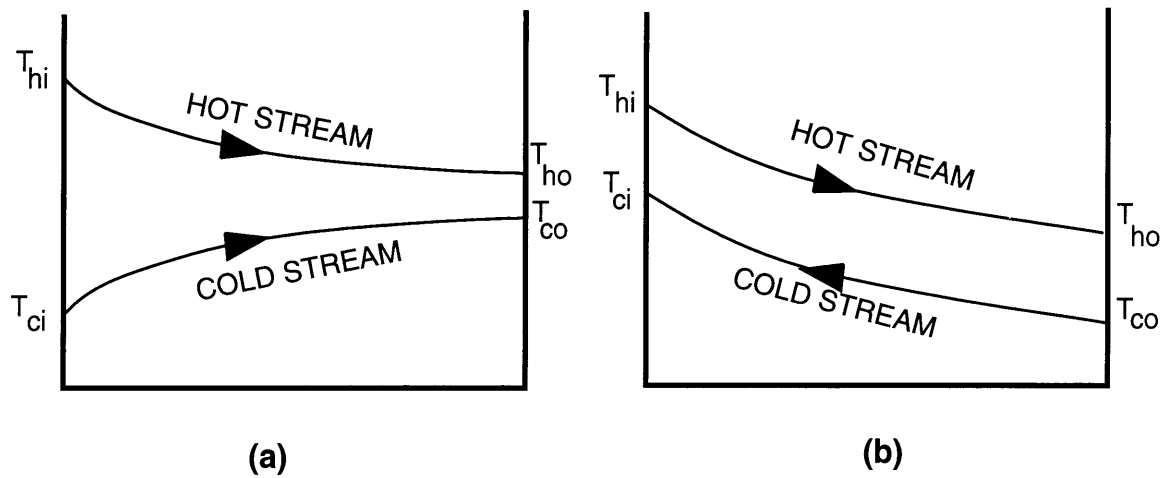


Figure 4-2: Schematic representations of (a) parallel-flow and (b) counterflow heat exchangers T_{ci} and T_{co} are cold stream inlet and outlet temperatures and T_{hi} and T_{ho} are inlet and outlet hot stream temperatures

The two major parameters used in the development are called the *effectiveness* ϵ and *number of transfer units* NTU.

Heat exchanger effectiveness ϵ is defined as (Ref[12]):

$$\epsilon = \frac{\text{actual heat transferred}}{\text{maximum heat transfer possible}} \quad (4.1)$$

Let the product of the mass flow rate \dot{m} and the average specific heat of the stream c_p be C :

$$C = \dot{m}c_p$$

Then C_c would correspond to the cold stream and C_h to the hot stream. Let the minimum of C_c and C_h be C_{min} .

We may easily infer from Figure 4-3 and equation 4.1 that:

$$\epsilon = \frac{C_c(T_{co} - T_{ci})}{C_{min}(T_{hi} - T_{ci})} = \frac{C_h(T_{hi} - T_{ho})}{C_{min}(T_{hi} - T_{ci})} \quad (4.2)$$

It is assumed that the temperature drop in the combustor section is negligible (the temperature drop in the combustor is the drop in temperature from the flame to the exit of the combustor). In Chapter 5, this assumption will be shown to be true.

The Number of Transfer Units NTU is defined as the ratio of the heat capacity of the heat exchanger to the maximum heat capacity of either of the fluid flows. The heat capacity of the heat exchanger measures its ability to transfer heat from one stream to another and thus is dependent on the overall heat transfer coefficient U and the heat transfer surface area A_h . Thus:

$$NTU = \frac{UA_h}{C_{min}} \quad (4.3)$$

Relations and graphs exist between ϵ and NTU for various configurations of parallel flow and counterflow (Ref[12]) and therefore, using this method, it is possible, given the temperatures of the inlet and outlet conditions of the heat exchanger, to determine the surface area A_h of heat transfer area required.

4.3 Algorithm for pressure drop analysis in compact heat exchangers

Figure 4-3 shows entrance pressure-drop and exit pressure rise characteristic of flow through a heat exchanger core.

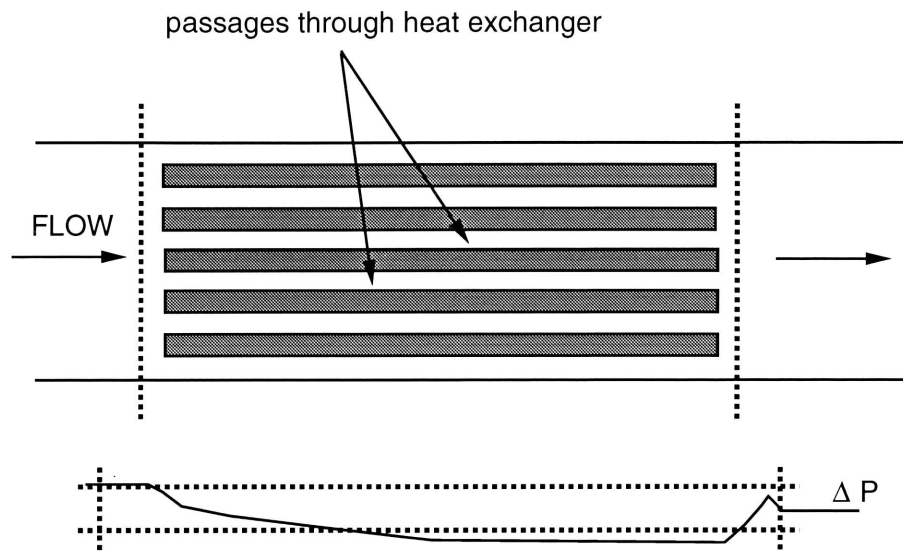


Figure 4-3: Entrance pressure-drop and exit pressure rise in a heat exchanger core (Ref[12])

The entrance pressure loss is a combination of the sudden contraction of flow area as well as the drop due to the momentum change that occurs till such time fully developed flow is established in the passages. The entrance pressure-drop ΔP can then be expressed as (Ref[12]):

$$\Delta P = \frac{1}{2} V^2 \rho (1 - \sigma^2) + K_c \frac{V^2}{2}$$

where V = average bulk flow velocity,

ρ is the average density,

σ is the ratio of the mean flow area to the frontal area.

The exit pressure rise is similarly a combination of pressure rise due to sudden expansion and pressure-drop due to momentum changes that occur till the flow is fully developed in the free

passage (Ref[12]):

$$\Delta P = \frac{1}{2}V^2\rho(1 - \sigma^2) - K_e \frac{V^2}{2}$$

K_c and K_e are functions of the contraction and expansion geometry and in some cases, of the Reynolds' number in the tubes. These coefficients have been established analytically for a number of simple geometries and are tabulated in Ref[12]. Typically, $K_c = 0.4$ and $K_e = 0.2$.

By integration of the momentum equation through the core, the relation for the flow stream pressure-drop calculation for most heat exchanger cores can be derived as (Ref[12]):

$$\Delta P_r = \frac{V_r^2}{2\rho_{ir}}(K_c + K_e + f \frac{A}{A_c} \cdot \frac{\rho_{ir}}{\rho_{mr}}) \quad (4.4)$$

$$\Delta P_p = \frac{V_p^2}{2\rho_{ip}}(K_c + K_e + f \frac{A}{A_c} \cdot \frac{\rho_{ip}}{\rho_{mp}}) \quad (4.5)$$

and the total pressure drop is given by:

$$\Delta P = \Delta P_r + \Delta P_p$$

4.4 Types of compact heat exchangers

Compact heat exchangers involving two fluids in the same phase are of two types (Ref[11],[12],[33]):

- Steady Flow heat exchanger is shown in Figure 4-4a and Figure 4-4b (Ref[34]). Figure 4-4a shows a multipass-*crossflow* configuration and comprises a number of passes where heat is exchanged between the hot and cold fluid streams. The ideal condition is when the number of passes is infinite, thus making the multipass-crossflow actually a counterflow. But physical and structural limitations limit the number of passes to a finite value, usually between two and four. Figure 4-4b shows a *counterflow* heat exchanger where the cold and hot streams

move counterflow to each other and exchange enthalpy across a heat transfer surface. This heat transfer surface may vary from a very simple tube-within-tube geometry or sets of tube bundles to a highly surface area enhanced plate-fin geometry.

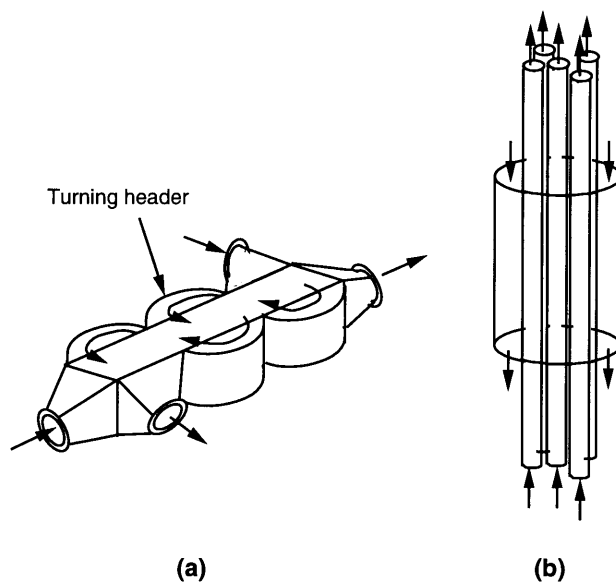


Figure 4-4: Steady flow heat exchangers (a) multipass crossflow configuration (Ref[34]) and (b) counterflow configuration

- Periodic Flow heat exchanger. The principle of this type of heat exchanger is that energy transfer occurs in cycles and each cycle comprises two parts. In one part of the cycle, heat is transferred by convection from the hot products to a matrix and stored in it. During the next part of the cycle, the hot matrix gives up its energy to the cold reactants. Depending on whether the matrix is in motion or not, there are two types of periodic flow heat exchangers. In one type, called the switching two-chamber periodic flow heat exchanger shown in Figure 4-5a (Ref[34]), the matrix is fixed and the flow alternates between products and reactants over the matrix. In the other type, called the disk-type rotary periodic flow heat exchanger

and shown in Figure 4-5b (Ref[34]), a matrix disk rotates between the two fluid streams transferring energy from hot stream to the cold. The two fluid streams are prevented from leaking into each other by a seal that acts against the rotating disk.

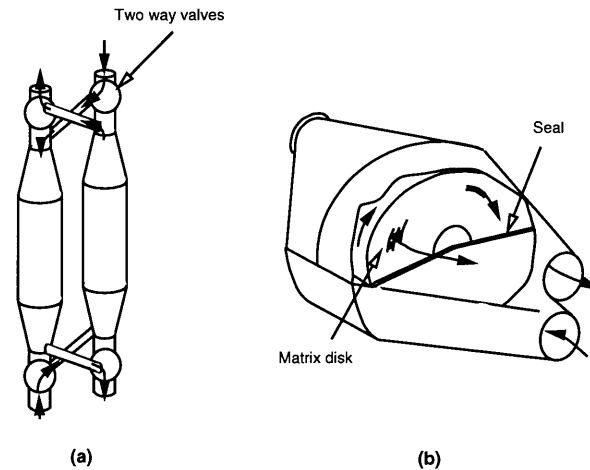


Figure 4-5: Periodic flow heat exchangers (a) Switching two-chamber configuration and (b) Rotary disk-type configuration (Ref[34])

In each type of compact heat exchangers briefly described above, a number of heat transfer surface geometries are commercially available. The design exercise presented in the next few sections and their sub-sections will attempt to isolate a few designs that would satisfy the performance criterion in Section 4.1 best.

4.5 Design of the Steady Flow heat exchanger

The steady-flow heat exchanger is shown in Figures 4-4a and b. As shown, they comprise the multipass-crossflow and counterflow types.

Heat transfer surfaces used in steady-flow heat exchangers are of two basic kinds (Ref[12]):

- Tube bundles: This is the simplest and most common arrangement for two-fluid heat exchangers. One form is shown in Figure 4-6a. The number and size of the tubes depend on the surface area requirement. In addition, surface area may also be enhanced by the addition of fins as shown in Figure 4-6b.

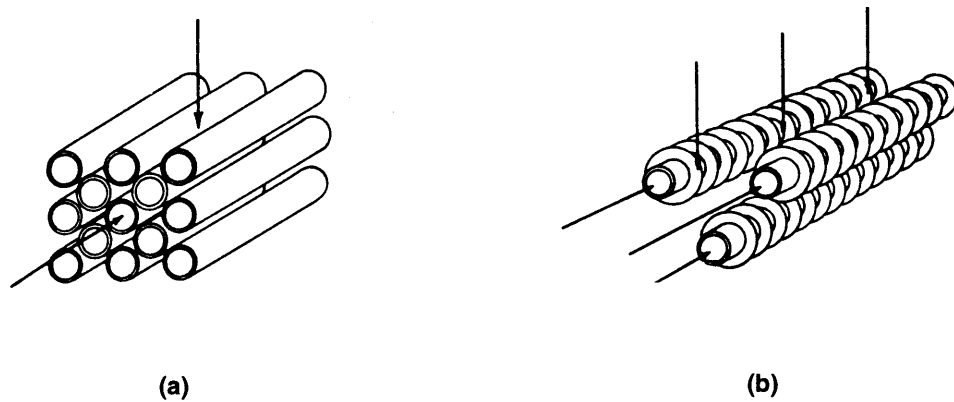
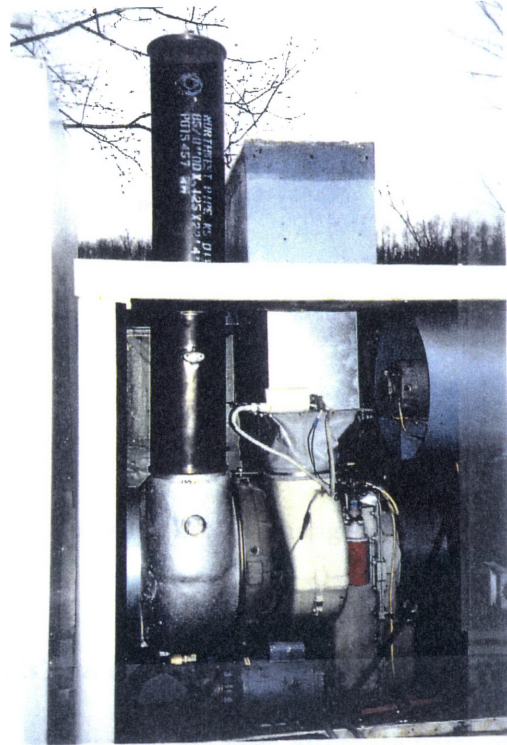


Figure 4-6: Tube bundles used as heat transfer devices (a) without fins
(b) with circular fins

The heat exchanger fabricated by Ref[21] while alternate designs were being studied by the author is shown in Figure 4-7. The fabricated heat exchanger consists of a set of concentric pipes. Their surface area is enhanced by the addition of fins as seen in Figure 4-7a. The dimensions of this heat exchanger can be seen in Figure 4-7c.



(a)



(b)

Figure 4-7a,b: (a) Fabricated heat exchanger of length 30 in. (0.754 m) showing finned inner tube (b) Gas-turbine showing mounted fabricated heat exchanger (Ref[21])

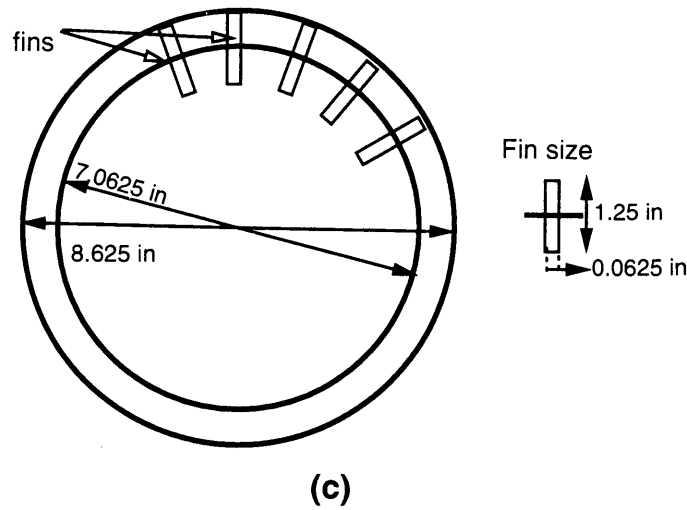


Figure 4-7c: Cross-sectional dimensions of fabricated heat exchanger (Ref[21])

- Plate fins:** Here the heat transfer surface is built of a sandwich of flat plates interconnected by fins as shown in Figure 4-8. The two fluids are carried between alternate pairs of plates. The fin structure may be of many types and can either be continuous or discontinuous. Discontinuous fins break down the boundary layer established by the fluid while flowing over the fin thereby increasing heat transfer, but they also pay a higher penalty in terms of pressure loss.

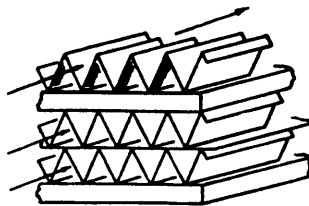


Figure 4-8: Plate-fin surface comprising a sandwich of plates and fins that are used in steady flow heat exchangers (Ref[12])

While *tube bundles* are simple and straightforward to manufacture, the only way in which surface area density (defined as the surface area per unit volume) can be substantially increased is to decrease the diameter of the tubes. Fabrication difficulties and cost place a limitation on how small the diameter of the tubes can be, and tube diameters with less than $\frac{1}{4}$ in. are rare (Ref[12]).

Plate fin geometries on the other hand, offer a much higher surface area density than do tube bundles. For gas-to-gas heat exchangers, as desired in this project, the usage of plate fin surfaces is the best method of accomplishing heat transfer (Ref[12]). Hence plate-fin surfaces are chosen for usage in the passes of the steady-flow heat exchanger.

Since a tubular heat exchanger (shown in Figure 4-6) has already been fabricated, a performance analysis will be done on this design. If necessary, some steps towards augmentation of this heat exchanger will also be suggested.

Design alternatives will also be suggested from the multipass-crossflow and counterflow types of steady-flow heat exchangers.

4.5.1 Fabricated heat exchanger: performance analysis

As mentioned in Section 4.5, a heat exchanger was already fabricated as shown in Figure 4-7. This heat exchanger is a basic counterflow type comprising two concentric tubes. The surface area of the inner tube is enhanced by means of fins.

4.5.1.1 Heat transfer requirements for the fabricated heat exchanger

Since the geometry shown in Figure 4-7 is relatively simple, it is possible to use the generalized equation of heat transfer for turbulent flow in pipes. This equation is given in terms of the Nusselt

number Nu , which is given for turbulent flow in pipes as (Ref[17]):

$$Nu = 0.023(Re)^{0.8}Pr^{\frac{1}{3}} \quad (4.6)$$

where: Re is the Reynolds number based on the hydraulic diameter

the velocity term in Re being determined from the continuity equation

Pr is the Prandtl number

= 0.7 for gases without too much loss of accuracy

When $Pr = 0.7$, this equation may be immediately simplified to:

$$Nu = 0.02 Re^{0.8}$$

The basic definition of the Nusselt number may be used to find the values of heat transfer coefficients:

$$Nu = \frac{hd_h}{k} \quad (4.7)$$

where: h is the average heat transfer coefficient

= h_r for the reactant side

= h_p for the product side

k is the average thermal conductivity of the gas

= k_r for the reactants and

= k_p for the products

The overall heat transfer coefficient U can be determined from:

$$\frac{1}{UA_h} = \frac{1}{h_r A_r} + \frac{1}{h_p A_p} \quad (4.8)$$

where A_h is an overall heat transfer area considered

A_p is the heat transfer on the product side

A_r is the heat transfer area on the reactant side

Usually A_h is taken either equal to A_r or A_p . A knowledge of A_h can be immediately correlated to the geometry and the length L of the fabricated heat exchanger required may be thus determined.

4.5.1.2 Pressure drop estimate for the fabricated heat exchanger

The pressure drop ΔP may be expressed as the penalty to overcome shear stresses along the wall:

$$\Delta P A_{cr} = A_h f \left(\frac{1}{2} \rho V^2 \right) \quad (4.9)$$

where A_{cr} is the cross-sectional area

f is the friction factor

ρ is mean density

V is the mean speed of the fluid

and the other symbols have the same meaning

For turbulent flow in pipes, the friction factor may be written as (Ref[17]):

$$f = \frac{0.046}{Re^{0.2}} \quad (4.10)$$

4.5.1.3 Results of heat transfer and pressure-drop analysis for the fabricated heat exchanger

Figure 4-9a shows the variation of the length L of the fabricated heat exchanger against equivalence ratio ϕ of the methane-air mixture. Figure 4-9b magnifies this graph in the region $0 < L < 1$ m. From Figure 4-9b, we can see that with the lengths marked L' (=30 inches), which is the maximum fabricated length of the heat exchanger, it is possible to allow the burning of methane-air mixtures of only $\phi = 0.35$ or higher (theoretical maximum $\phi = 0.37$; this is the equivalence ratio at which no heat exchanger is needed). From Figure 3-12, it can be seen that the theoretical maximum equivalence ratio ϕ needed to produce the rated power output is ≈ 0.2 . Clearly then, from the Figures 4-9b and 3-12, it can be seen that the heat transfer requirements cannot be satisfied by the fabricated heat exchanger shown in Figure 4-7.

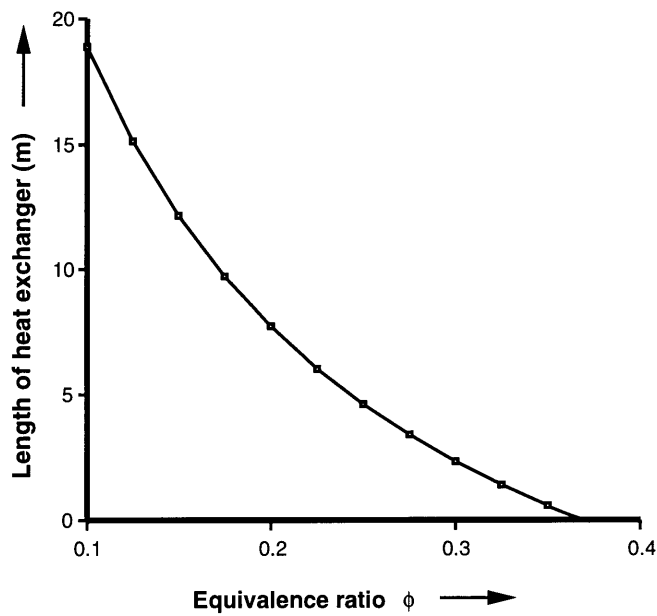


Figure 4-9a: Variation of length L of fabricated heat exchanger as a function of equivalence ratio ϕ of methane-air mixture

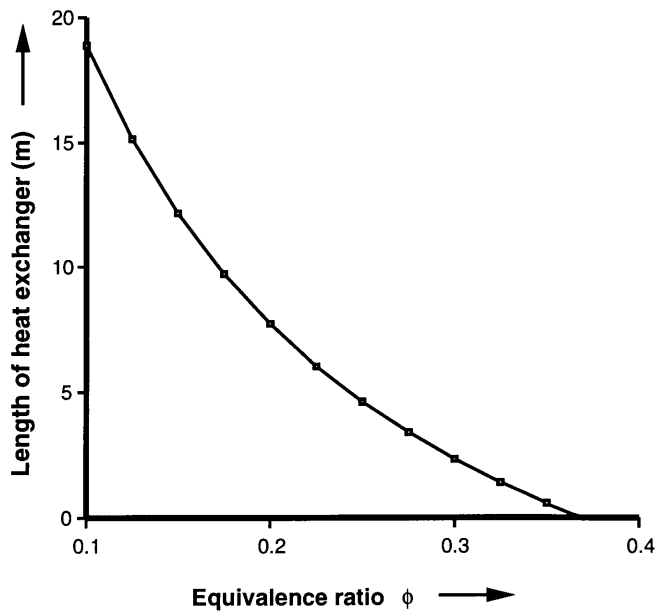


Figure 4-9b: Variation of length of heat exchanger L when $0 < L < 1$ against equivalence ratio ϕ

Since the fabricated heat exchanger does not satisfy heat transfer requirements, it is redundant to do a pressure-drop analysis. A method of augmenting the performance of this heat exchanger

will be suggested in the next section and the performance of such an augmented heat exchanger will be evaluated.

4.5.1.4 Suggested augmentation of fabricated heat exchanger: addition of fins

From continuity relations, the average bulk velocity of fluid in the inner tube in the fabricated heat exchanger has been determined to be ≈ 83 m/s. Ref[22] suggests that the velocity of the fluid in this tube be increased by the addition of a blockage and also extend the fin length upto the blockage (see Figure 4-10). The diameter of the blockage d_0 can be determined from continuity relations and the velocity of flow which has been limited to 100 m/s. Thus:

$$d_0 = 2.90 \text{ in.} = 74 \text{ mm}$$

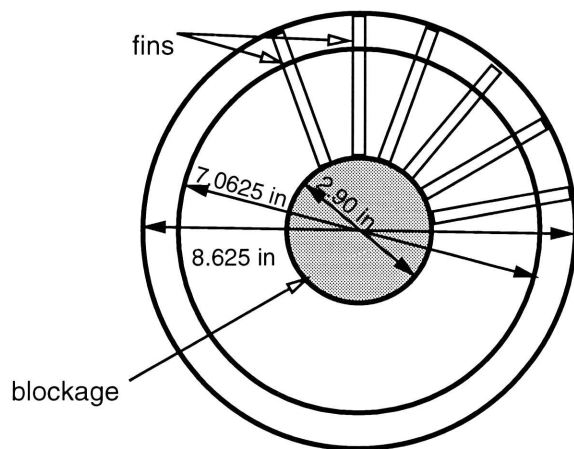


Figure 4-10: Suggested augmentation to the fabricated heat exchanger by adding a blockage and lengthening the fins to the blockage. Diameter of the blockage has been suggested as $d_0 = 2.90$ in = 74 mm

4.5.1.5 Performance of fin augmented heat exchanger

Figure 4-11a shows variation of the length of the augmented heat exchanger L against the number of fins N_f for various values for equivalence ratio of the methane-air mixture ϕ used. Figure 4-11b magnifies this graph in the region $0 < L < 1$ m. From this figure, it can be seen that with $N_f = 100$ and length same as the maximum fabricated length $L' = 30$ inches, it can be seen that the lowest equivalence ratio ϕ of fuel-air mixture that can be burned is ≈ 0.2 . Since this is the ϕ value around which the gas-turbine GS-350 gives its maximum rated power output (see Figure 3-12), this augmentation satisfies heat transfer requirements.

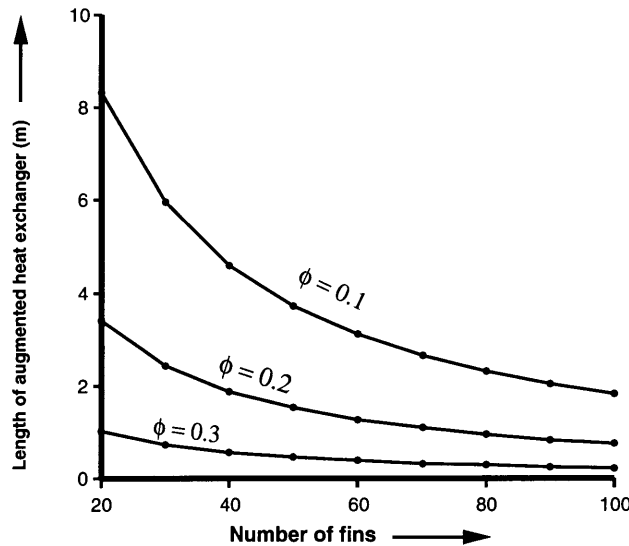


Figure 4-11a: Variation of length L of augmented heat exchanger against number of fins N_f for various ϕ

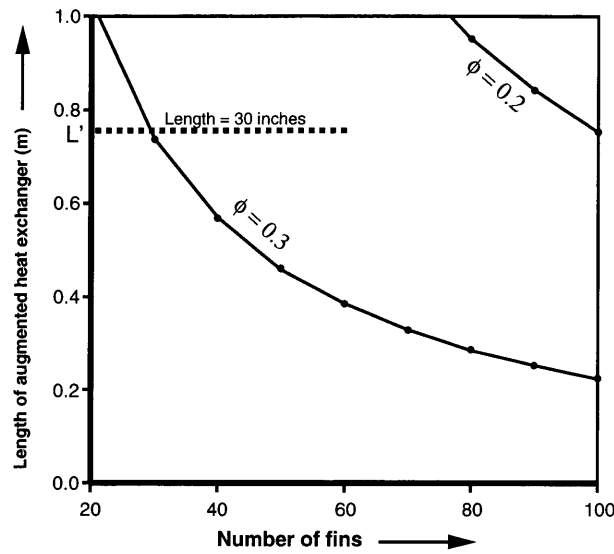


Figure 4-11b: Variation of L against N_f for $0 < L < 1$ m. Using maximum length of fabricated heat exchanger of $L' = 30$ in. and $N_f = 100$, lower bound of ϕ that can be used is 0.2

Figure 4-12 shows the variation of pressure-drop ΔP (expressed as a percentage of the inlet pressure) against length of the heat exchanger L in the region $0 < L < 1$ for various values of number of fins N . ΔP is almost linearly dependent on L . Also with $L = 1$ m, and with $N_f = 100$, ΔP is $\approx 2.5\%$, which satisfies the performance criterion for performance defined in Section 4.1.

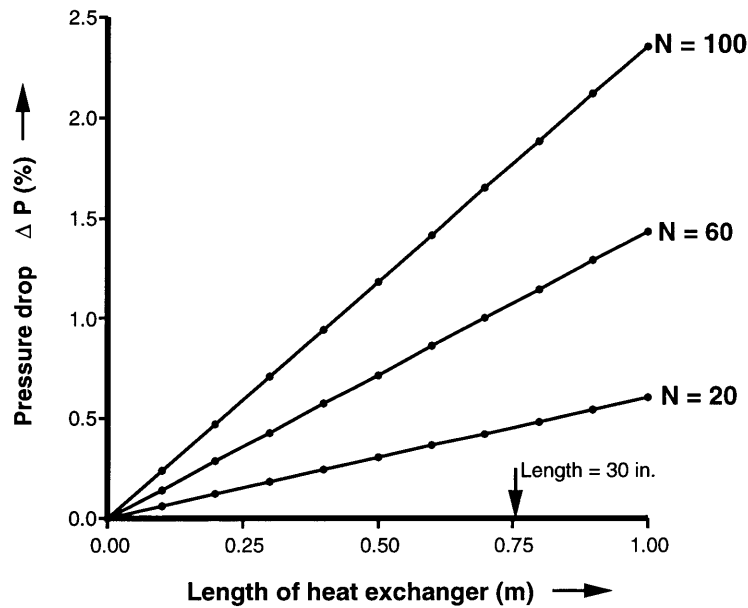


Figure 4-12: Variation of ΔP against L of the augmented heat exchanger for various values of N

From Figures 4-11 and 4-12, it can be seen that the augmented heat exchanger can be used satisfactorily when $N = 100$ and with $L = L' = 30$ inches.

In the original fabricated heat exchanger $N_f = 20$ and the recommended augmentation $N_f = 100$. Hence 80 more fins have to be added around the smaller tube. This addition may be source of thermal stresses and structural weakness. It is therefore, more advantageous to design a heat exchanger with enhanced surface geometry of the plate-fin type.

4.5.2 Multipass-crossflow steady flow heat exchanger

The multipass-crossflow heat exchanger is shown schematically in Figure 4-4a. From the figure, it can be seen that each pass in crossflow can be considered as a cuboid of dimensions a , b and c as shown in Figure 4-13. If the turning headers are disregarded for design, which does not introduce too much inaccuracy, the multipass-crossflow heat exchanger in Figure 4-4a may be considered as

a stack of cuboids.

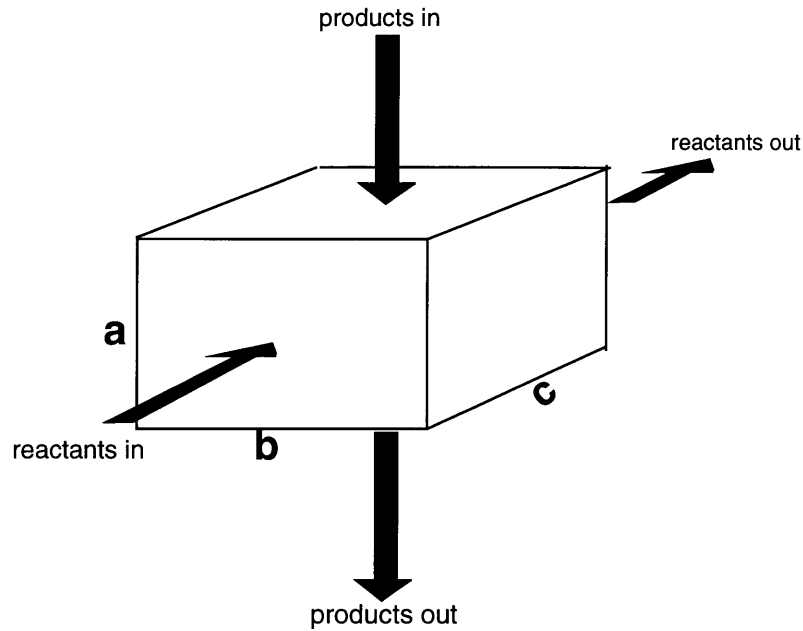


Figure 4-13: Each pass in a multipass-crossflow heat exchanger modelled as a cuboid of height a , width b and depth c

4.5.2.1 Choice of plate-fin geometries

As mentioned in Section 4.5, tubular heat transfer surfaces are not as good as plate-fin surfaces for gas-to-gas heat transfer (Ref[12]). Therefore, only plate-fin heat transfer surfaces are chosen and design and analysis is done for these surfaces.

Plate-fin geometries have been subdivided into plain-fin, louvered-fin, strip-fin, wavy-fin and perforated-fin types as shown in Figure 4-14. Heat transfer and friction data for numerous members of each type are tabulated in Ref[12]. Within each type, however, only one or at the most two geometries are chosen to be evaluated. The criterion for elimination can mostly be done by simple inspection and is based on heat transfer data provided. Accordingly, the performance, of a steady-flow heat exchanger with plate-fin geometries has been evaluated for the geometries shown in Figure

4-14. Note that the geometries are coded by semi-descriptive methods that are described below.

Plain-fin surfaces shown in Figure 4-14a are characterized by long, uninterrupted flow passages with a simple fin configuration. The semi-descriptive method of designating plain-fin surfaces refer to the number of fins per inch transverse to the flow direction. The additional letter *T* indicates traingular passageways.

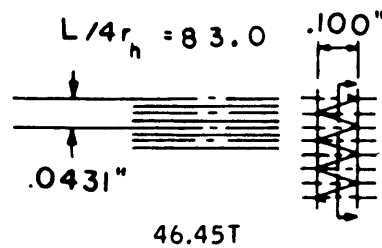


Figure 4-14a: Plain-fin 46.45T heat transfer surface geometry (Ref[12])

Louvered-fin surfaces shown in Figure 4-14b are characterized by fins that have been cut and bent out into the flow stream at frequent intervals. Louvered-fin surfaces are characterized by two figures. The first refers to the length of the louvered fin in the flow direction, and the second to the fins per inch transverse to the flow.

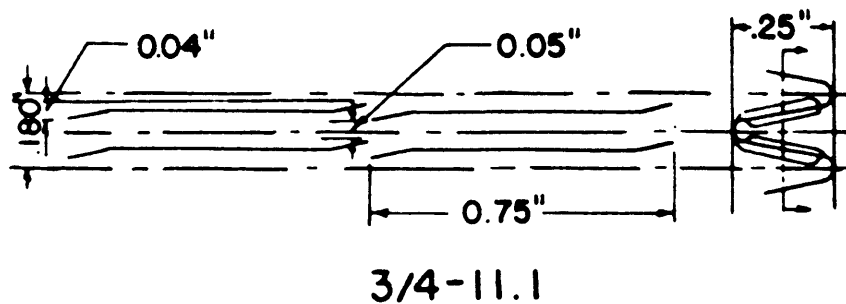


Figure 4-14b: Louvered-fin $\frac{3}{4}$ -11.1 heat transfer surface geometry (Ref[12])

Strip-fin surfaces shown in Figure 4-14c are similar to the louvered-fin surfaces, the only difference being that the short sections of fins are aligned entirely with the flow direction. With the strip-fin configuration it is feasible to have the very short flow-length fins and therefore very high heat transfer coefficients. However, experimental uncertainty for strip fins is greater than any other surface because the friction performance is very sensitive to the structural integrity of the surface, which is difficult to maintain given the complexity of the surface. The designation scheme for strip-fin surfaces is essentially the same as louvered-fin surfaces.

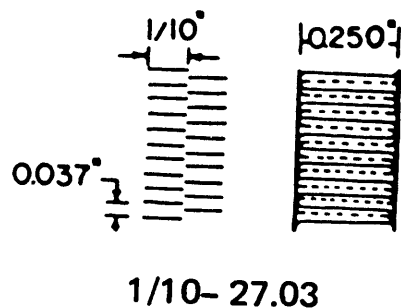


Figure 4-14c: Strip-fin $\frac{1}{10}$ - 27.03 heat transfer surface geometry (Ref[12])

Wavy-fin surfaces shown in Figure 4-14d are also high performance surfaces with performance similar to the strip-fin and louvered-fin surfaces. Wavy-fin surfaces are designated by two figures, giving the number of fins per inch and the wavelength, followed by the letter W. Thus surface $17.8-\frac{3}{8}W$ has 17.8 fins per inch and a complete wave every $\frac{3}{8}$ in.

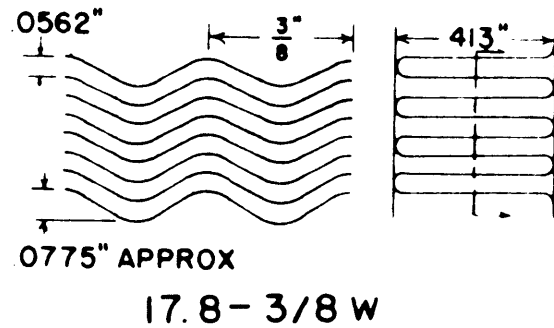


Figure 4-14d: Wavy fin $17.8-\frac{3}{8}W$ heat transfer surface geometry (Ref[12])

Pin-fin surfaces shown in Figure 4-14e can also achieve very high heat transfer coefficients by maintaining thin boundary layers on fins. Fins are constructed from small-diameter wire. However, friction factors can be quite high sometimes. The designation scheme for pin-fin surfaces is not descriptive.

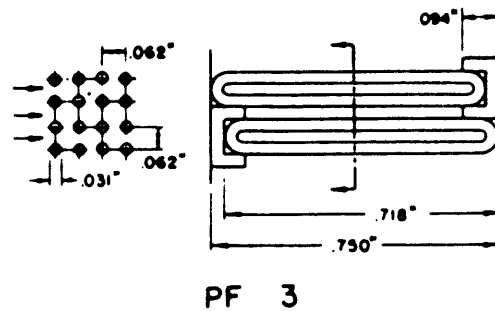


Figure 4-14e: Pin-fin PF-3 heat transfer surface geometry

Perforated-fin surfaces shown in Figure 4-14f is described and designated simply by the number of fins per inch transverse to the flow and the letter P. Holes cut out of the fins again provide boundary layer interruptions and therefore high heat transfer coefficients.

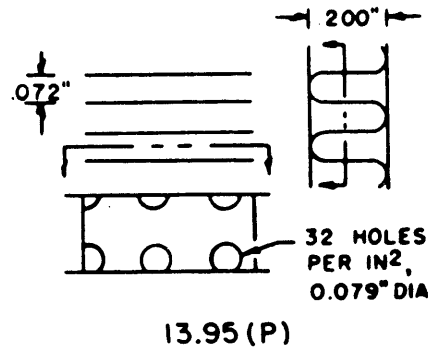


Figure 4-14f: Perforated-fin 13.95(P) heat transfer surface geometry (Ref[12])

4.5.2.2 Data presentation for each plate-fin surface

Both heat transfer and pressure drop data are tabulated in Ref[12]. Heat transfer data for plate-fin surfaces are specified through a number of parameters:

k : the plate spacing in m ;

d_h : the hydraulic diameter in m;

α : the heat transfer area per unit volume in m^2/m^3 ;

$StPr^{\frac{2}{3}}$: the non-dimensional heat transfer coefficient and

Re : the Reynolds number.

Relations between heat exchanger effectiveness ϵ and number of transfer units NTU for steady-flow heat exchangers of the multipass-crossflow type are shown in Figure 4-15. The specific heats

of the reactant and product streams has been assumed to be equal, an assumption that is within the bounds of accuracy so that their ratio $\frac{c_{pp}}{c_{pr}}$ is 1.

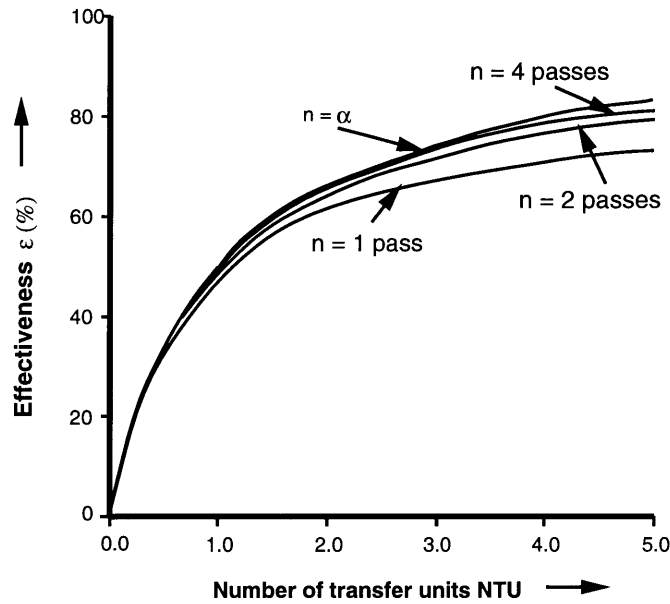


Figure 4-15: Relation between ϵ and NTU for multipass-crossflow heat exchangers for number of passes n . It is assumed that $\frac{c_{pp}}{c_{pr}} = 1$ (Ref[12])

It can be seen that the effectiveness of a single-pass steady flow heat exchanger is not as good as the effectiveness of two-pass to counter-flow kinds. The effectiveness of the steady-flow heat exchanger having at least two-passes can be represented by the following best fit polynomial equation with a high degree of accuracy:

$$NTU = 118.59\epsilon^5 - 178.18\epsilon^4 + 97.01\epsilon^3 - 19.91\epsilon^2 + 2.61\epsilon + 0.001 \quad (4.11)$$

Pressure drop for plate-fin surfaces in Ref[12] are specified through the parameters:

f : the friction factor and

K_c & K_e : entrance and exit coefficients

4.5.2.3 Numerics for the steady-flow heat exchanger

The size and pressure drops for each of plate-fin geometries shown in Figure 4-14 have been iteratively computed as functions of equivalence ratio of the methane-air fuel used (an iterative method is necessary to converge to the integral number of sets of plates that simultaneously satisfy requirements of heat transfer and flow cross-section).

Size has been expressed in terms of volume V , and also in terms of physical dimensions viz. height, width and depth of a two-pass, three-pass and four-pass steady-flow heat exchanger for each type of geometry. Height of an N -pass heat exchanger is the same as N times the dimension a shown in Figure 4-13. Width and depth are the same as the dimensions b and c respectively in Figure 4-13.

Pressure drop ΔP has been expressed as a percentage of the inlet pressure to the heat exchanger, which is 4 atm (Ref[12]).

A ranking system to compare the various geometries has been devised. According to this system, heat exchangers are ranked according to the volume V and pressure ΔP with a smaller rank assigned to the designs resulting in lower V and ΔP . A combination of these ranks in performance expresses a total rank of performance (performance is defined in Section 4.1).

4.5.2.4 Results

Figure 4-16 shows the relation between the volume V of the multipass steady-flow heat exchanger calculated for various plate-fin geometries shown in Figure 4-14 against equivalence ratio of a

methane-air mixture ϕ . Note that V is the same for a particular geometry and particular ϕ regardless of the number of the passes. V expresses the size of the heat exchanger that satisfies heat transfer requirement. The size of the heat exchanger decreases with increasing ϕ . This expected since with increasing ϕ , the minimum temperature required to ensure burning of the methane-air mixture in the combustor T_3 lowers according to Figure 2-6.

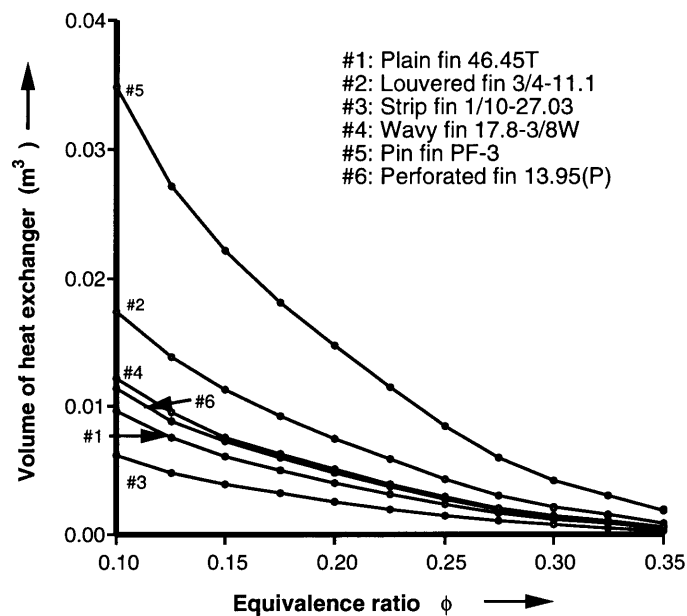


Figure 4-16: Variation of volume V against ϕ for multipass crossflow heat exchangers

Figure 4-17 shows the relation between the pressure drop ΔP expressed as a percentage of the inlet pressure (4 atm) for the multipass steady-flow heat exchanger calculated for various plate-fin geometries shown in Figure 4-14 against equivalence ratio of a methane-air mixture ϕ . Since the total flow lengths are the same regardless of the number of passes, ΔP is the same for a particular heat transfer surface geometry and particular value of ϕ . Since the size of the heat exchanger reduces as ϕ increases, fluid flow lengths decrease, and hence ΔP decreases as ϕ increases. As

mentioned before, the percentage of ΔP is restricted to 8%, and therefore, some of the geometries could be eliminated on that strength alone.

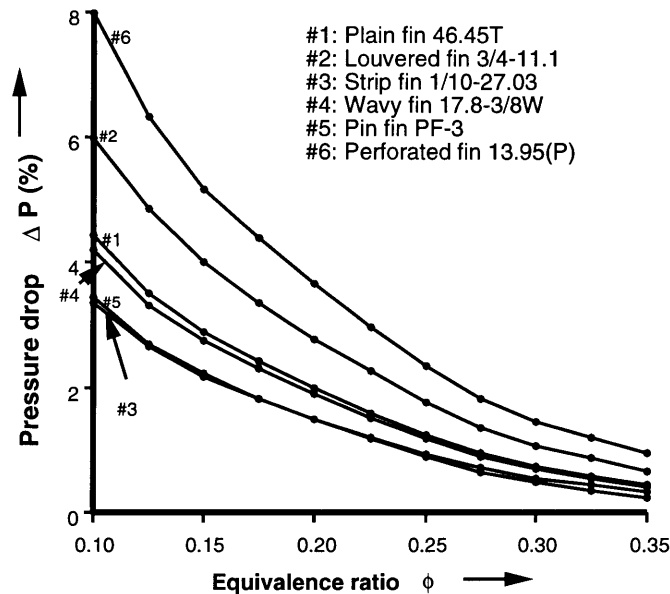


Figure 4-17: Variation of pressure drop ΔP against ϕ for various plate-fin geometries

Figure 4-18 shows the comparison of the geometries in Figure 4-14 by means of the ranking system discussed in Section 4.4.1.3. As mentioned, a lower rank shows a better performance. From Figure 4-18, it can be seen that the four geometries corresponding to the gray bars (including the cross-hatched bar) have a higher performance than the other geometries. Though the ranking system may be faulted to not give proper weightage to the parameter in question - size or pressure drop by assuming equal weightage to both, it is a simple but powerful way to eliminate the large number of geometries that are being considered and restricts the choices to four. These four are the plain-fin 46.45T, strip-fin $\frac{1}{10}$, the wavy-fin $17.8-\frac{3}{8}W$ and in-line pin-fin PF-3. It may be noted that while satisfying heat transfer requirements, these geometries do not give a pressure loss of more

than about 5%, which is well within the limit of the performance criterion defined in Section 4.1.

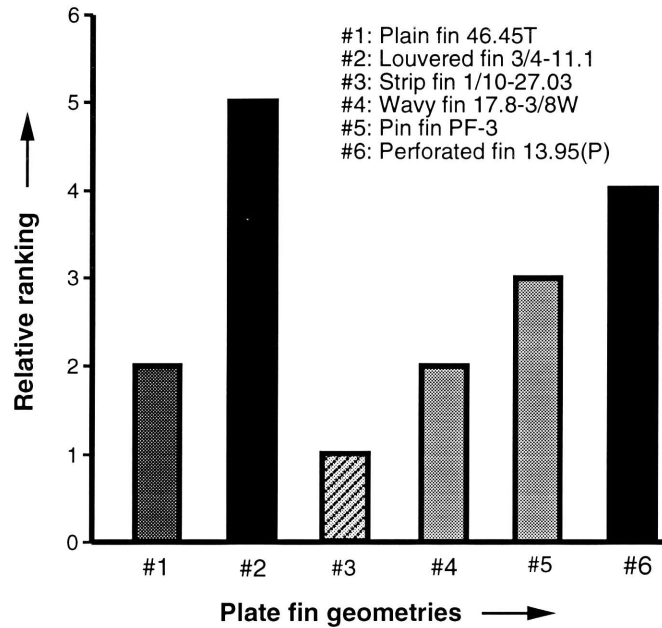


Figure 4-18: Relative ranking of performance of the various plate fin geometries. Geometries shown in gray have higher performance than geometries shown in black

A further elimination of geometry may be done on the basis of the inaccuracy of results of the strip-fin (performance shown as the cross-hatched bar in Figure 4-18) resulting from its complicated geometry. As mentioned in Section 4.4.1.1, in spite of having the best performance, strip-fin geometries are not easy to fabricate and structural integrity, dependent on the material, and upon which the experimental heat transfer data depend, cannot be accurately maintained. Hence the number of geometries can be further restricted to three - the plain-fin 46.45T, the wavy-fin $\frac{1}{10}$ and the pin-fin PF-3 geometries. Depending on more structural investigation, either of these three heat transfer surface geometries may be used. A more detailed analysis of the dimensions of heat exchangers using these three geometries is summarized in Figures 4-19, 4-20 and 4-21.

Figure 4-19 shows the dimensions and number of plates of a multipass heat exchanger in whose

crossflow passes the plain-fin 46.45T heat transfer area geometry is used. The dimensions, explained in Section 4.4.1.3, are the height, width and depth of the resultant heat exchanger. N is the number of sets of plate-fins used, which must be equal on both product and reactant side.

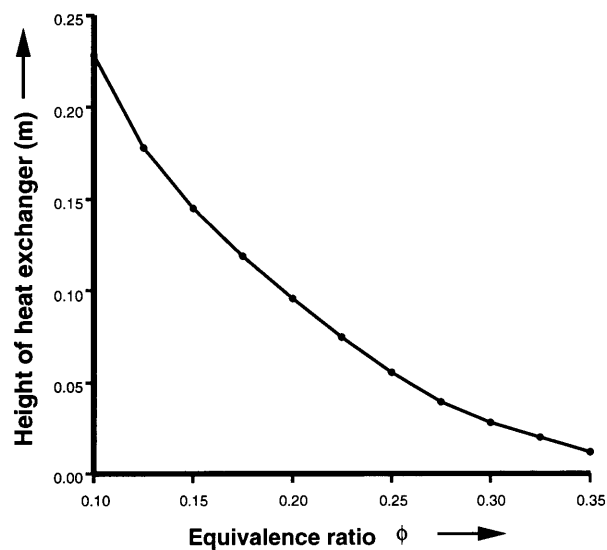


Figure 4-19a: Variation of height of multipass crossflow heat exchanger with plain-fin 46.45T against equivalence ratio ϕ for various n

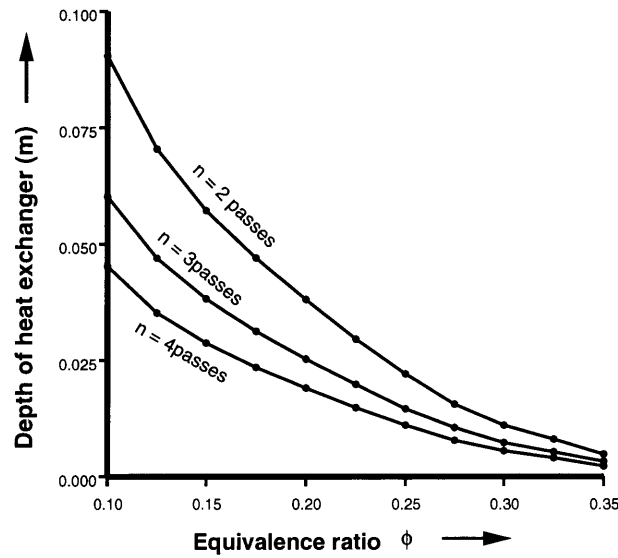


Figure 4-19b: Variation of depth of multipass crossflow heat exchanger with plain-fin 46.45T against equivalence ratio ϕ for various n

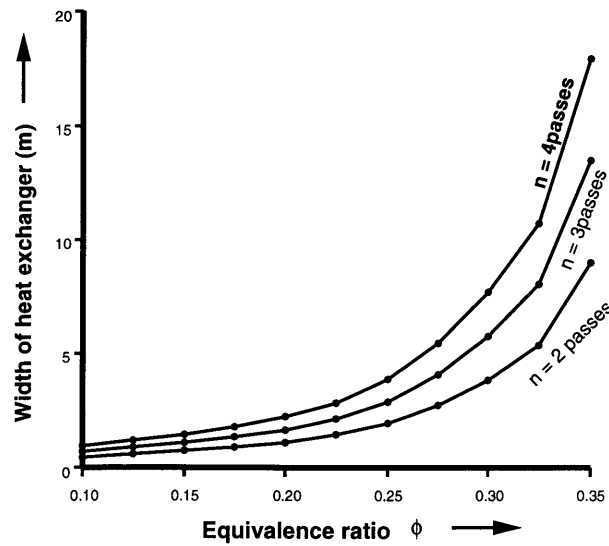


Figure 4-19c: Variation of width of multipass crossflow heat exchanger with plain fin 46.45T against ϕ for various n

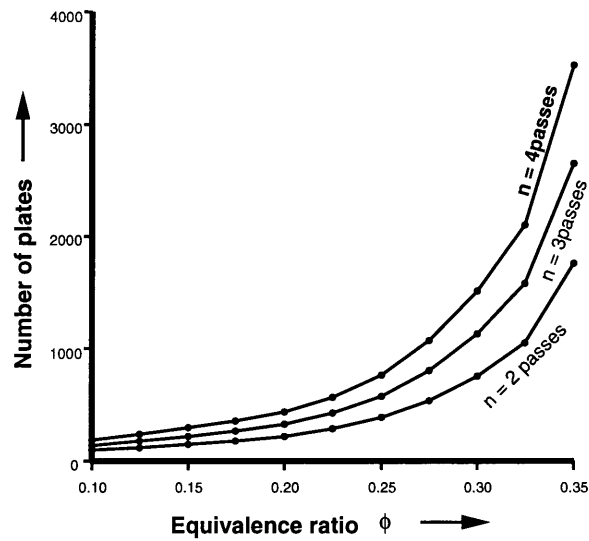


Figure 4-19d: Variation of number of plates N against ϕ for various n : plain-fin 46.45T

Similarly, Figures 4-20 and 4-21 show the dimensions and number of plates of a multipass heat exchanger in whose crossflow passes the wavy-fin $17.8-\frac{3}{8}W$ and pin-fin PF-3 respectively heat transfer area geometries are used.

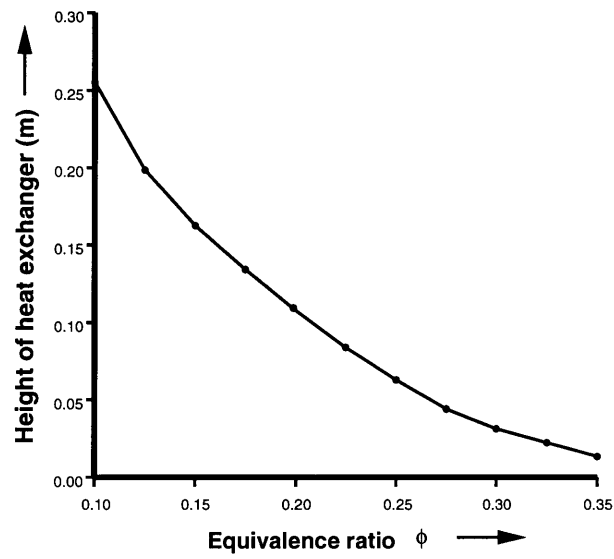


Figure 4-20a: Variation of height of multipass crossflow heat exchanger with wavy-fin 17.8- $\frac{3}{8}$ W against equivalence ratio ϕ for various n

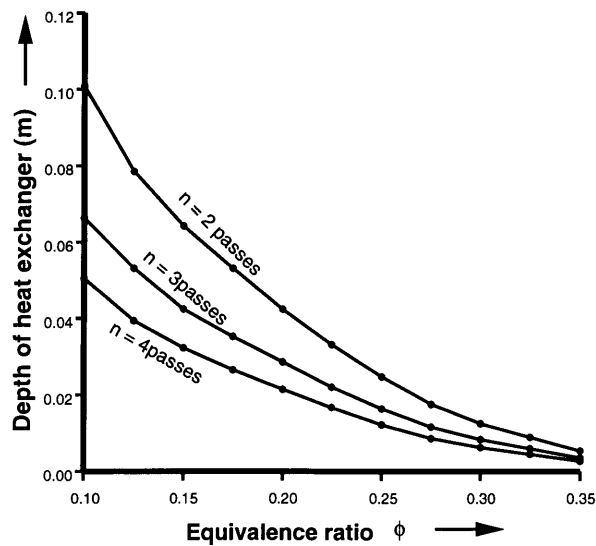


Figure 4-20b: Variation of depth of multipass crossflow heat exchanger with wavy-fin 17.8- $\frac{3}{8}$ W against equivalence ratio ϕ for various n

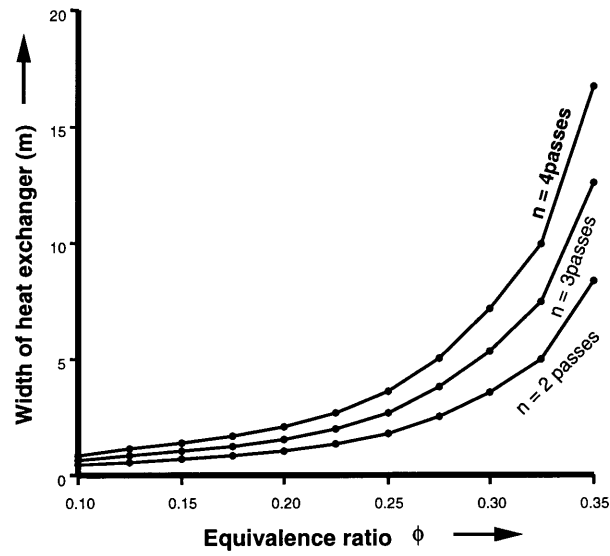


Figure 4-20c: Variation of width of multipass crossflow heat exchanger with wavy-fin $17.8\text{-}\frac{3}{8}\text{W}$ against ϕ for various n

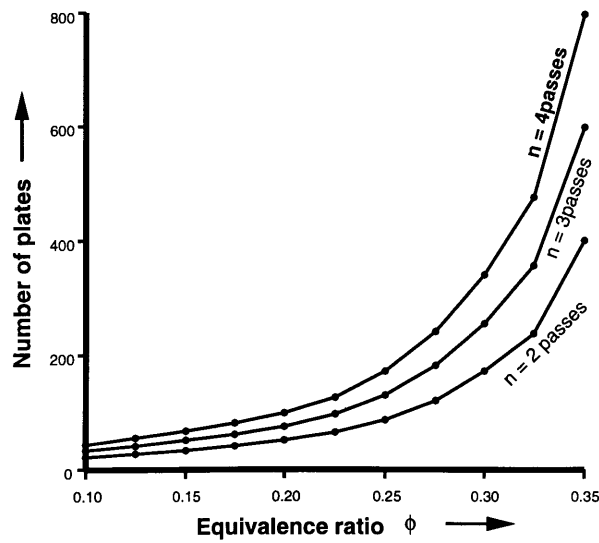


Figure 4-20d: Variation of number of plates N against ϕ for various n : wavy-fin $17.8\text{-}\frac{3}{8}\text{W}$

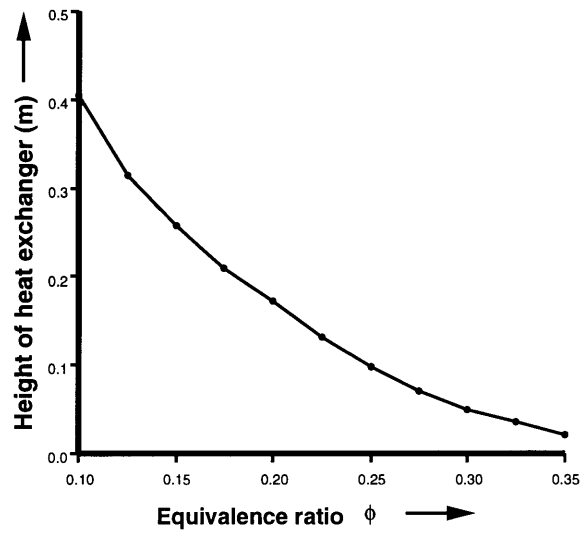


Figure 4-21a: Variation of height of multipass crossflow heat exchanger with pin-fin PF-3 against equivalence ratio ϕ for various n

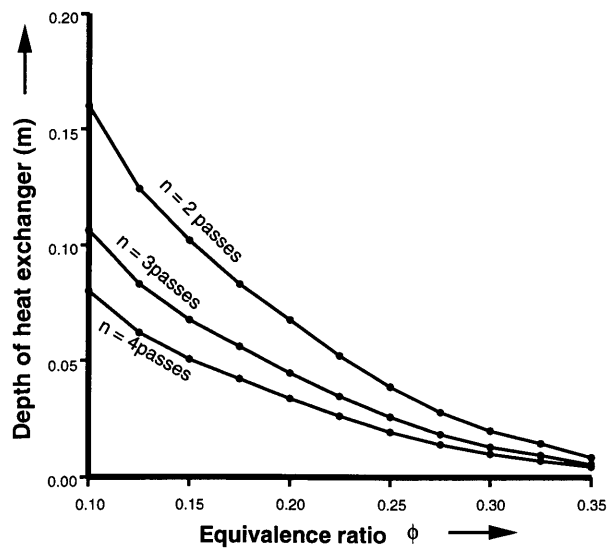


Figure 4-21b: Variation of depth of multipass crossflow heat exchanger with pin-fin PF-3 against equivalence ratio ϕ for various n

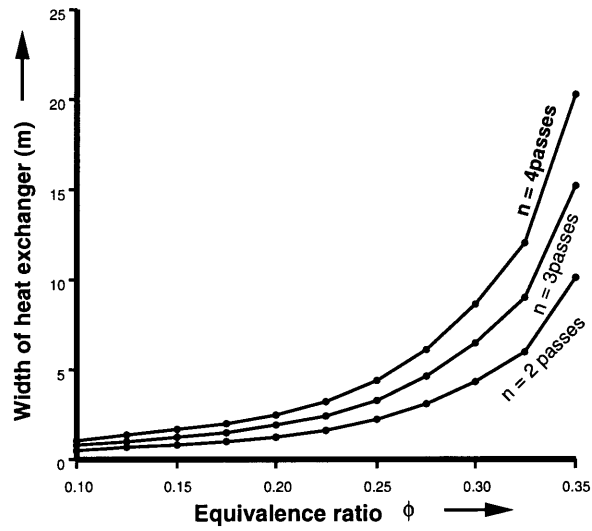


Figure 4-21c: Variation of width of multipass crossflow heat exchanger with pin-fin PF-3 against ϕ for various n

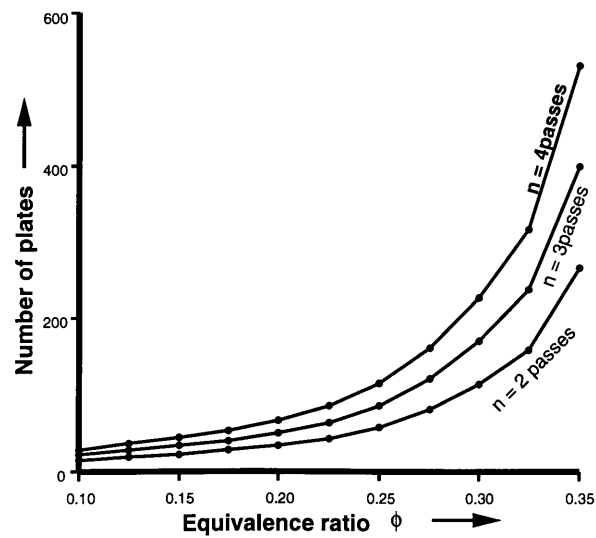


Figure 4-21d: Variation of number of plates N against ϕ for various n : pin-fin PF-3

From Figures 4-19, 4-20 and 4-21, it can be seen that the dimension of importance is b , the

width of the heat exchanger since it is of large value. From these figures, it can also be inferred that ϕ should not be raised beyond 0.2 for practical purposes as b is already of the order of magnitude of 1 at that ϕ value.

4.5.3 Plate-fin counterflow steady-flow heat exchanger

In the previous section, a family of more compact heat transfer surface viz. plate-fin surfaces were suggested for the design of the steady-flow heat exchanger. Types and choices of plate-fin geometries are discussed in Section 4.5.2.1. From the same section, it was inferred that the number of plate-fin geometries that satisfy the performance criterion of Section 4.1 best are limited to three - the plain-fin 46.45T, the wavy-fin 17.8- $\frac{3}{8}$ W and the pin fin PF-3. Therefore the design of the plate-fin counterflow steady-flow heat exchanger need be done for the above three geometries.

A counterflow steady-flow heat exchanger is shown in Figure 4-4b. The length of the heat exchanger is L , its width b and its depth c . It can be easily seen that $b = 2Nk$ where N is the integral number of plate-fins of either the product or reactant side and k is the plate spacing.

4.5.3.1 Heat transfer and pressure-drop data

Heat transfer and pressure-drop data are given in Ref[12] and are in the same format as described in Section 4.5.2.2 since the heat transfer surface geometry are the same.

4.5.3.2 Results: heat transfer and pressure-drop of plate-fin counterflow steady-flow heat exchangers

Figure 4-22a,b and c show the variation of depth c against the height L of the counterflow steady flow heat exchanger for various values of N , the number of sets of plates for the plain-fin 46.45T

geometry. Figure 4-22d shows the variation of pressure drop ΔP , expressed as a percentage of the inlet pressure (4 atm) against height of the heat exchanger for various values of n . Note that ΔP is the same for all equivalence ratio ϕ and N as the flow length is the same regardless of the combination of N and ϕ .

Graphs in Figure 4-23 and 4-24 show also variation of size and pressure-drop parameters for the wavy-fin 17.8- $\frac{3}{8}$ W and pin-fin PF-3 plate-fin geometries.

By suitably selecting L and N , c can be determined. The width of the heat exchangers b may be determined by:

$$b = 2Nk \quad (4.12)$$

where k is the plate spacing

= 2.54 mm for the plain-fin 46.45T

= 10.49 mm for the wavy-fin 17.8- $\frac{3}{8}$ W and

= 11.91 mm for the pin-fin PF-3

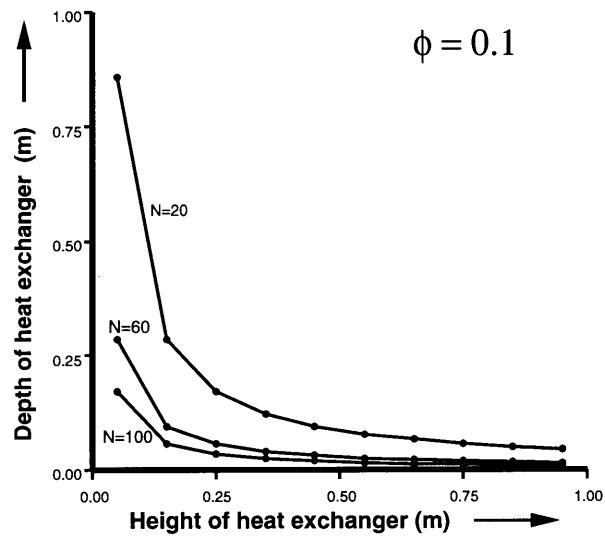


Figure 4-22a: Variation of depth c of heat exchanger against height of heat exchanger L for various N . Equivalence ratio $\phi = 0.1$. Geometry used is plain-fin 46.45T

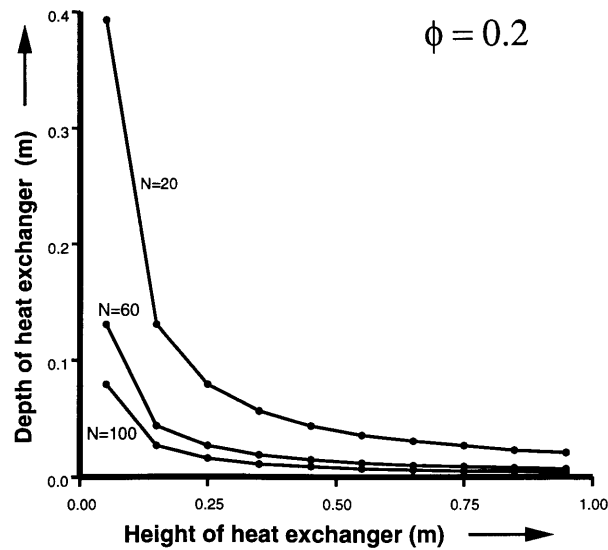


Figure 4-22b: Variation of depth c of heat exchanger against height of heat exchanger L for various N . Equivalence ratio $\phi = 0.2$. Geometry used is plain-fin 46.45T

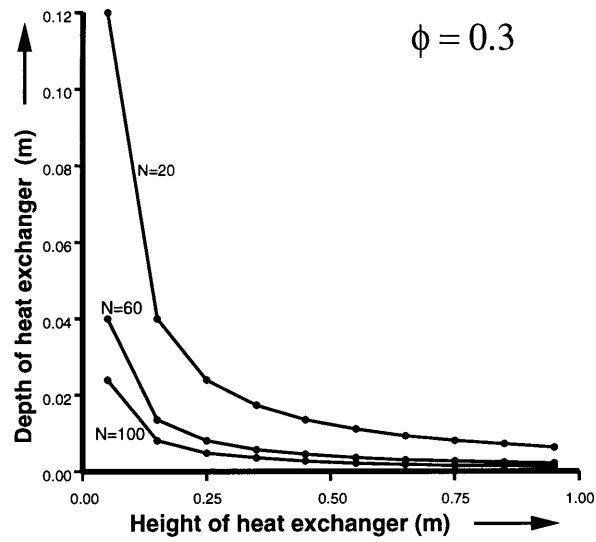


Figure 4-22c: Variation of depth c of heat exchanger against height of heat exchanger L for various N . Equivalence ratio $\phi = 0.3$. Geometry used is plain-fin 46.45T

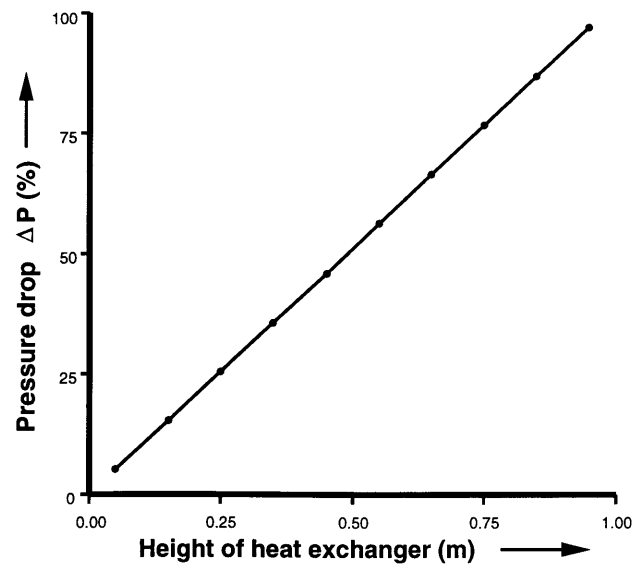


Figure 4-22d: Variation of pressure drop ΔP expressed as a percentage of inlet pressure against L . ΔP is constant for all N and ϕ . Geometry used is plain-fin 46.45T

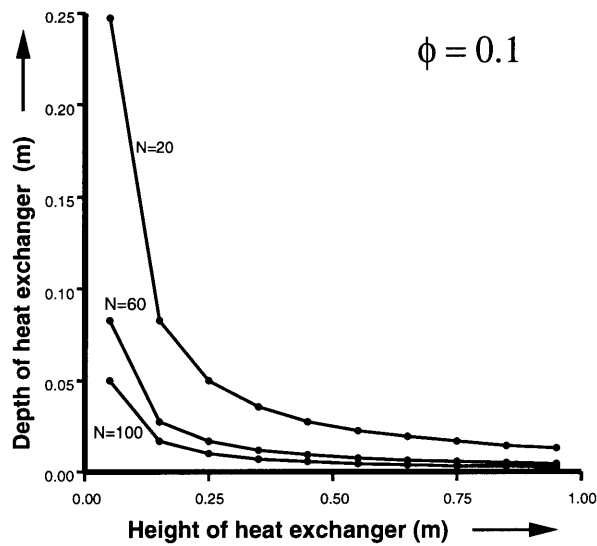


Figure 4-23a: Variation of depth c of heat exchanger against height of heat exchanger L for various N . Equivalence ratio $\phi = 0.1$. Geometry used is wavy-fin 17.8- $\frac{3}{8}$ W

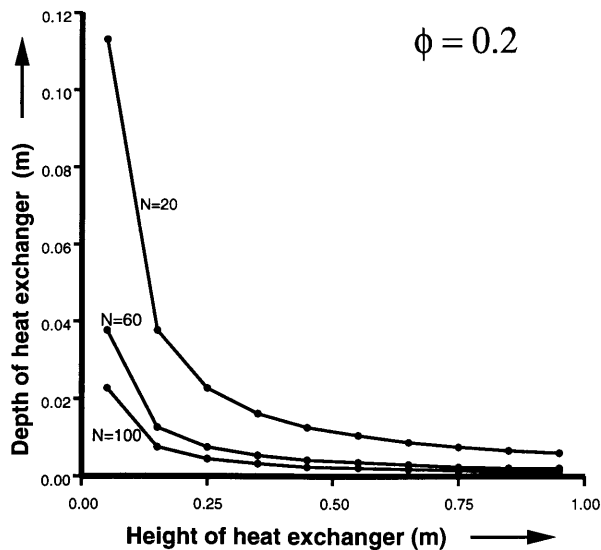


Figure 4-23b: Variation of depth c of heat exchanger against height of heat exchanger L for various N . Equivalence ratio $\phi = 0.2$. Geometry used is wavy-fin 17.8- $\frac{3}{8}$ W

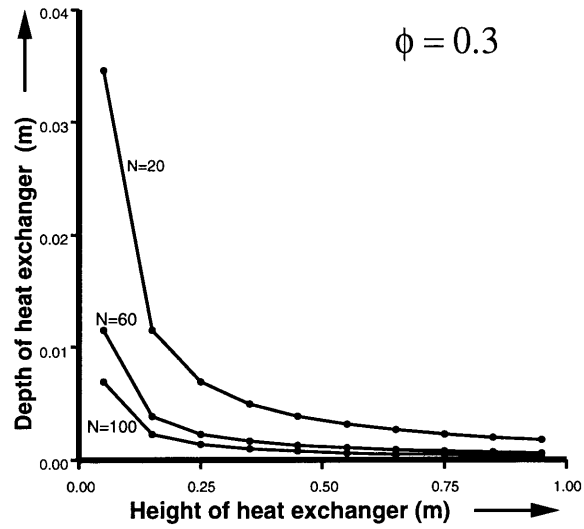


Figure 4-23c: Variation of depth c of heat exchanger against height of heat exchanger L for various N . Equivalence ratio $\phi = 0.3$. Geometry used is wavy-fin $17.8-\frac{3}{8}W$

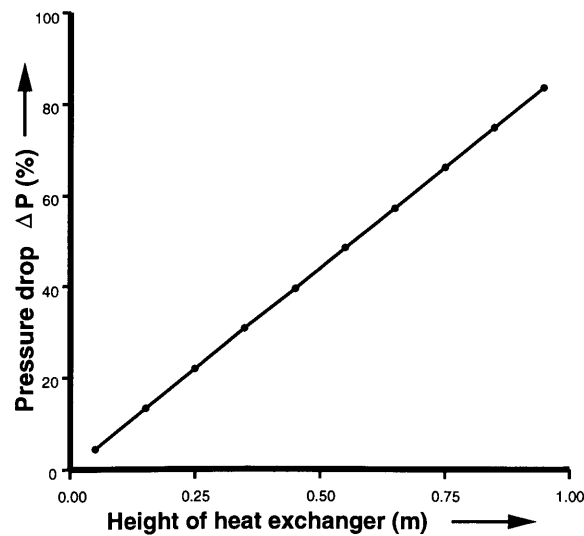


Figure 4-23d: Variation of pressure drop ΔP expressed as a percentage of inlet pressure against L . ΔP is constant for all N and ϕ . Geometry used is wavy-fin $17.8-\frac{3}{8}W$

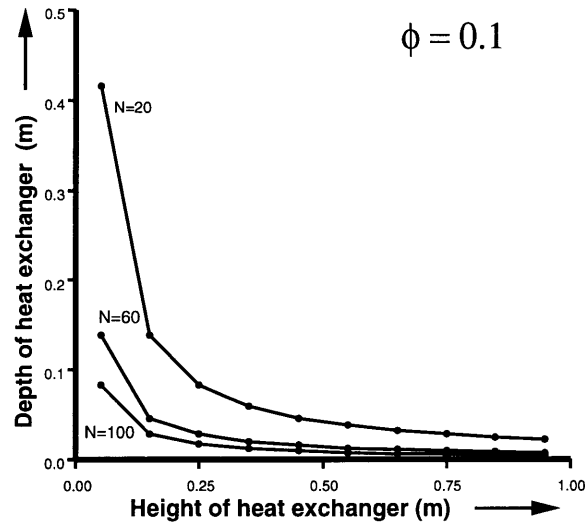


Figure 4-24a: Variation of depth c of heat exchanger against height of heat exchanger L for various N . Equivalence ratio $\phi = 0.1$. Geometry used is pin-fin PF-3

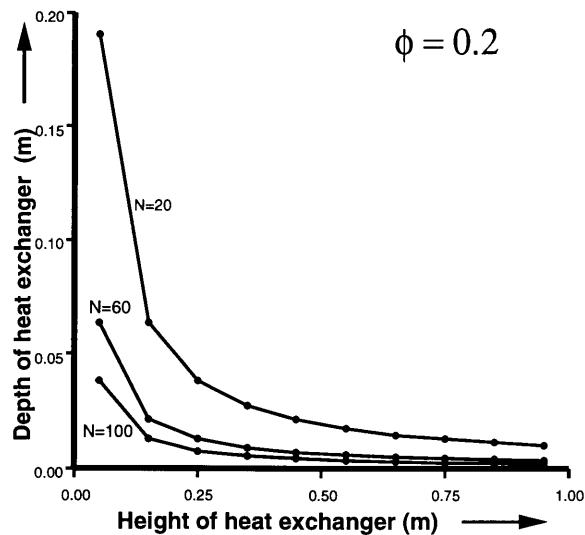


Figure 4-24b: Variation of depth c of heat exchanger against height of heat exchanger L for various N . Equivalence ratio $\phi = 0.2$. Geometry used is pin-fin PF-3

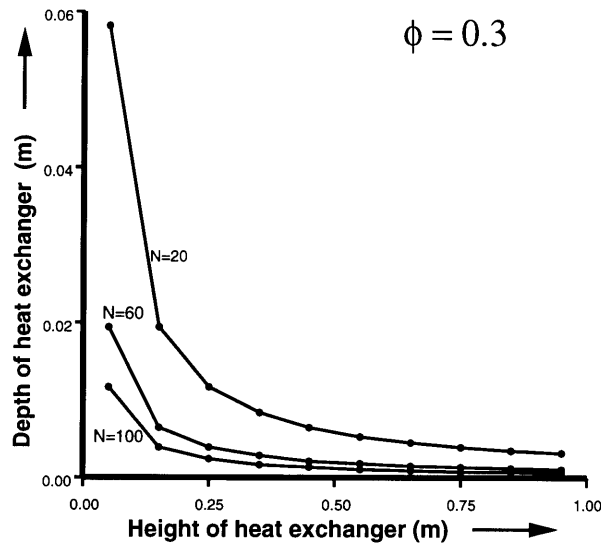


Figure 4-24c: Variation of depth c of heat exchanger against height of heat exchanger L for various N . Equivalence ratio $\phi = 0.3$. Geometry used is pin-fin PF-3

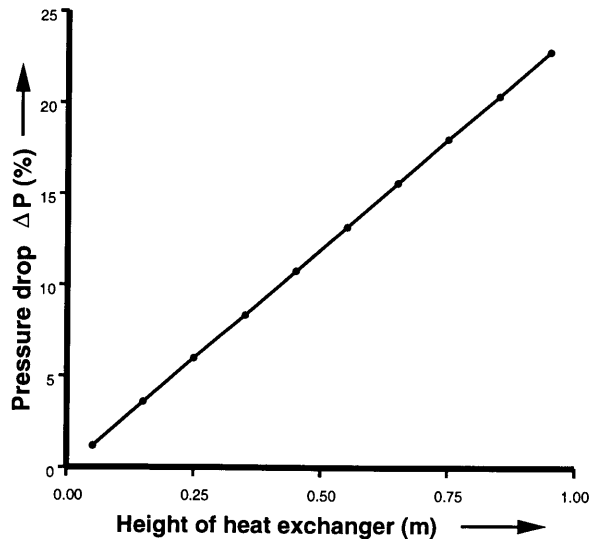


Figure 4-24d: Variation of pressure drop ΔP expressed as a percentage of inlet pressure against L . ΔP is constant for all N and ϕ . Geometry used is pin-fin PF-3

4.6 Design of the Periodic Flow heat exchanger

It is desirable that the heat exchanger designed have little or no moving parts at all. This is to satisfy the objective of burning the ultra-lean methane-air mixture with as little as modification as possible to the existing gas-turbine. In periodic-flow heat exchangers, however, moving parts cannot be avoided. In the switching two-chamber periodic-flow heat exchanger shown in Figure 4-5a, the matrix is fixed and a set of valves alternate the flow between the products and the reactants. In the rotary disk-type periodic-flow heat exchanger shown in Figure 4-5b, the matrix alternates between the two fluid streams by rotation (Ref[34]).

It must seem, therefore, that the steady-flow heat exchanger must be chosen over the periodic-flow heat exchanger on this argument. But the advantages in using a ceramic is to have a matrix that can be used at the elevated temperatures of combustion. Also, in matrices, the diameter of the passage-ways restricts the flow to the laminar Reynolds number regime. This restriction increases the heat transfer and reduces the pressure drop penalties and therefore need to be investigated. In choice of type of periodic-flow heat exchanger, however, since the additional moving mechanism is only one in the case of the rotary-disk type periodic-flow heat exchanger (to rotate the disk) in comparison to a number of mechanisms required to open and close valves, the rotary-disk type heat exchanger is a preferential choice.

4.6.1 Choice of matrix geometries

Ref[12] tabulates the heat transfer and pressure-drop data for two common types of matrix geometries, viz. triangular and hexagonal shown in Figure 4-25. From Ref[12], upon inspection of heat transfer data, it can be seen that the hexagonal geometry is more suitable and therefore has been chosen as the geometry to be used for the periodic flow heat exchanger.

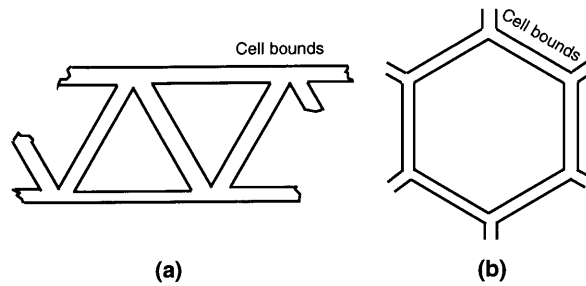


Figure 4-25: Two most common types of matrix geometries for rotary disk-type periodic-flow heat exchanger (a) triangular (b) hexagonal

4.6.2 Data presentation for the hexagonal ceramic matrix

Heat transfer and pressure-drop data for the hexagonal ceramic matrix are presented in Ref[12].

In addition, data are obtained from Ref[34]. Heat transfer and pressure drop data are specified through a number of parameters:

d_h : the hydraulic diameter of each hexagonal passage-way in m

$$= 0.0006 \text{ m}$$

Re : the Reynolds number

p : the porosity, defined as the ratio of volume of pores within the matrix to

the gross volume of the matrix

$$= 0.8105 \text{ for the hexagonal matrix}$$

$StPr^{\frac{2}{3}}$: the non-dimensional heat transfer coefficient which is inversely

proportional to Re

$$= \frac{15.05}{Re} \text{ for the hexagonal matrix}$$

α : ratio of heat transfer area to the total volume in m^2/m^3

$$= 5400 \text{ m}^2/\text{m}^3$$

Relations between heat exchanger effectiveness ϵ and NTU for periodic-flow heat exchangers are shown in Figure 4-26. The non-dimensional number C_{rot} is the matrix flux heat capacity and expresses the switching rate of the matrix. C_{rot} is mathematically defined as the ratio of the heat capacity of the matrix to the heat capacity of the flow.

$$C_{rot} = \dot{m}_m c_{pm} / C_{min}$$

where: C_{min} is the minimum of $\dot{m}c_p$ of either fluid streams

\dot{m}_m is the mass flux of the matrix and depends on the rate of
rotation of the matrix

c_{pm} is the heat capacity of the matrix

C_{rot} is a chosen quantity for the matrix since the speed of rotation can be controlled by an external mechanism. However, from Figure 4-26, it can be seen that when $C_{rot} = 5$ or more, the ϵ -NTU relation is almost equivalent to infinite switching rate i.e. $C_{rot} = \infty$

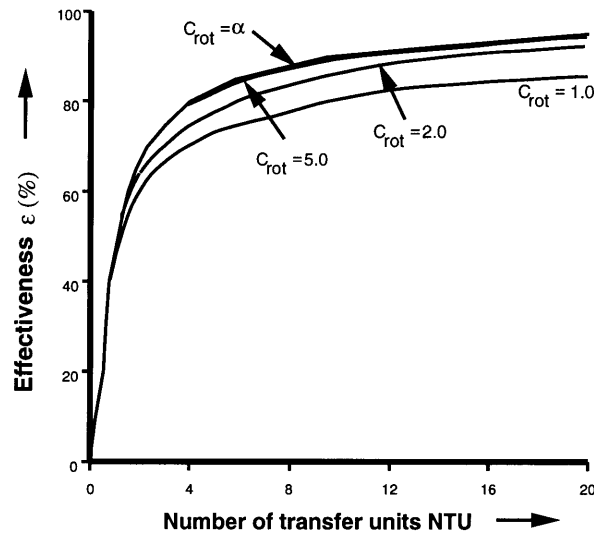


Figure 4-26: Variation of effectiveness ϵ of periodic flow heat exchanger against number of transfer units NTU for various rotational speeds C_{rot} . Ratio of specific heats $\frac{c_{pp}}{c_{pr}} = 1$ (Ref[34])

From Figure 4-26, the effectiveness ϵ of a periodic-flow heat exchanger when the ratio of the specific heats of the two streams $\frac{c_{pp}}{c_{pr}}$ is 1 (and $C_{rot} = 5$) can be best represented by the polynomial fit:

$$\begin{aligned}
 NTU = & 72794.7\epsilon^{10} - 331436\epsilon^9 + 650632.5\epsilon^8 - 720406.2\epsilon^7 + 494209.3\epsilon^6 \\
 & - 217097.6\epsilon^5 + 60833.5\epsilon^4 - 10421.2\epsilon^3 + 976.7\epsilon^2 - 34.9\epsilon
 \end{aligned} \tag{4.13}$$

Pressure-drop data for laminar flow are essentially specified with the same parameters as in Section 4.4.1.2 with the exception that the friction factor f , like $StPr^{\frac{2}{3}}$, is a constant function of the Reynolds number Re :

$$f = \frac{5.05}{Re} \text{ for the hexagonal matrix}$$

4.6.3 Numerics for the periodic flow heat exchanger

The size and pressure drop for the glass-ceramic hexagonal matrix have been iteratively computed as functions of Reynolds number Re for values of equivalence ratio ϕ of the methane-air mixture used.

While the size of the rotary disk-type periodic-flow heat exchanger has been presented in terms of diameter of the disk d_d and the thickness of the disk t_d , pressure drop ΔP has been presented as a percentage of the inlet pressure to the heat exchanger (4 atm); both are expressed as functions of Reynolds number Re for various values of ϕ of methane-air mixture.

4.6.4 Results and Discussion

Figure 4-27a shows the variation of diameter of the matrix disk d_d against Reynolds number Re for values of equivalence ratio ϕ of methane-air mixture. From the figure, it can be seen that d_d is independent of ϕ . This is expected, because d_d is influenced by flow rate and cross-section and not by heat transfer requirements.

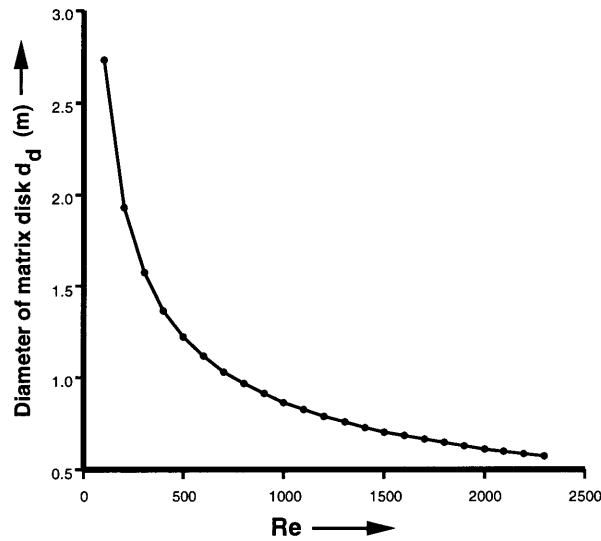


Figure 4-27a: Variation of diameter of matrix disk d_d against Re . d_d is not influenced by ϕ

Figure 4-27b shows the variation of thickness of the matrix disk t_d against Re for various values of ϕ . For a particular ϕ value, it can be seen that t_d increases as Re increases. This is because the non-dimensional heat transfer coefficient, being inversely proportional to Re , decreases as Re increases. In order to facilitate the same heat transfer, it is then necessary to provide greater heat transfer surface area A_h , which is achieved by increasing t_d . For a particular value of Reynolds number Re , t_d decreases with increasing ϕ . This is because of the increased chemical energy content of the methane-air mixture with increasing ϕ , the size of heat exchanger required is smaller, directly appearing as smaller t_d .

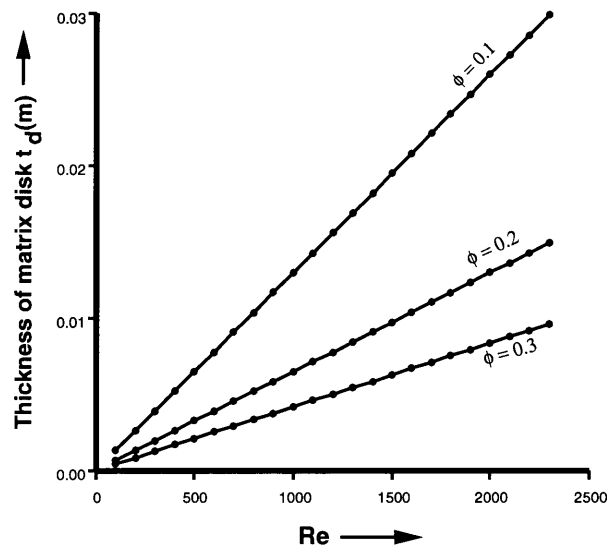


Figure 4-27b: Variation of thickness of disk t_d against Re for various values of ϕ .

Figure 4-27c shows the variation of pressure drop ΔP as a percentage of the inlet pressure to the heat exchanger (4 atm) against Reynolds number Re for various values of equivalence ratio ϕ . It can be seen that for a particular value of ϕ , ΔP increases with increasing Re . With increasing Re , velocity in the passages and hence friction losses increase, and therefore, this variation is seen. As ϕ is increased but Re is kept constant, the size of the heat exchanger needed is reduced. As the cross-sectional area is not influenced by ϕ and but thickness of the matrix t_d is, flowlength is reduced with increasing ϕ for a particular value of Re . Since decreasing fluid flowlength decreases ΔP , reduction in ΔP with increasing ϕ and constant Re can be seen in Figure 4-27c.

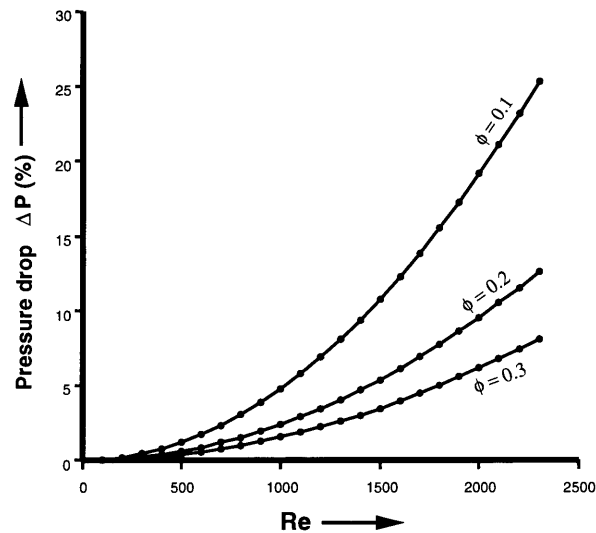


Figure 4-27c: Variation of pressure drop ΔP against Re for various values of ϕ .

A comparison of the order of magnitudes of values d_d and t_d respectively from Figures 4-27a and 4-27b shows that the critical dimension is d_d . The smallest value of d_d is hence desired. Increasing Re increases the flow speed within the passage-ways of the matrix and hence from Figure 4-27a, d_d may be made smaller. However, from Figure 4-27b, it can be seen that Re of flow cannot be extended to the boundary of the laminar-turbulent region (≈ 2300) since ΔP exceeds the tolerated 8% drop when $Re \approx 1300$ (for $\phi = 0.1$) to when $Re \approx 2200$ (for $\phi = 0.3$). To admit of a wide range of ϕ , it is therefore necessary to restrict $Re \approx 1200$. Thus $d_d \approx 0.8\text{m}$ (80 cm).

4.6.5 Power required to rotate the matrix

The power requirement to operate the motor mechanism that rotates the matrix does not depend on the fluid flow characteristics and is weakly dependent on the equivalence ratio ϕ of the fuel-oxidizer mixture (increasing ϕ decreases the size, and hence, mass of the matrix; in general, power required to rotate a smaller mass is smaller, additional factors remaining the same). This is

because friction between the bearings and the matrix as well as friction between the seals and the matrix have a greater influence on the power requirement. However, mechanical design is not the objective of this chapter and therefore a rigorous calculation of power requirement has not been attempted. Instead, Ref[22] has been consulted on a general figure. A well designed rotating system does not require power greater than about 0.02% of the total maximum power output of the gas-turbine power plant. For the GS-350, therefore, power required to rotate the matrix is about 4kW (maximum rated power output is 225kW).

4.7 Decision making: the Steady-flow vs. the Periodic-flow heat exchanger

In the case of the fabricated heat exchanger (Section 4.5.1), a large number of fins have to be additionally welded ($= 80$), their length increased (to 2.90 in from 0.625 in) and a central blockage created in order for it to perform according to the requirements in Section 4.1. However, additional welding is difficult to perform given the small nature of tolerances when the number of fins become large. Also, welding introduces points of structural weakness which may be magnified when the heat exchanger is installed and operated at the elevated temperatures of combustion. Hence, augmentation of the fabricated heat exchanger, though theoretically possible, does not appear practically feasible.

In the steady-flow multipass-crossflow heat exchanger (Section 4.5.2), the width of the heat exchanger b is the critical dimension since, as mentioned in Section 4.4.1.4, b increases rapidly compared to the other dimensions. In order that the value of b be around 1 m (requirement from Section 4.1), it is necessary to limit (upper) the equivalence ratio ϕ to 0.2 and the number of passes to 2. From Figure 3-12, it can also be seen that in order to get the maximum power output from the gas-turbine, ϕ need not be much greater than 0.2. This may therefore appear to be a good match

of requirements. It must be pointed out, however, that with the addition of a turning header in the steady-flow heat exchanger (see Figure 4-4a), b will be much greater than 1 m, which is undesirable and compensatable only by other more complicated methods like splitting and/or diverting the flow.

In the case of the plate-fin counterflow heat exchanger utilizing plate-fin geometries (Section 4.5.3), all the dimensions may be so chosen from Figures 4-22, 4-23 and 4-24 so that they comfortably lie within the bound specified in Section 4.1. From these figures, it can be seen that this may be accomplished without too much penalties in pressure-drops either.

The diameter of the disk d_d in the periodic-flow heat exchanger cannot be made less than 0.8 m since Reynolds number Re has to be limited to 1200 (see Section 4.4.2.4). The periodic-flow heat exchanger design will additionally need a design for the mounting and operation of a motor that would rotate the matrix. Even though the power requirement for this rotating mechanism is quite low, the dimension d_d being close to the bound specified in Section 4.1 does not make the periodic-flow heat exchanger a viable design compared to the counterflow heat exchanger mentioned above.

4.8 Conclusions

The ϵ -NTU method (Section 4.2) is simple yet powerful method of designing and analyzing the performance of heat exchangers as demonstrated in previous sections. Using this method, a seemingly large number of heat exchanger options have been examined and choices have been narrowed down to very few. Where a simple geometry such as tubes are employed, it is possible to use analytical results with good accuracy.

On the strength of the arguments presented in the Section 4.7, it can be clearly seen that a

counterflow steady-flow heat exchanger utilizing either of the three plate-fin geometries viz plain-fin 46.45T, wavy-fin $17.8-\frac{3}{8}W$ or the pin-fin PF-3 is the best design of the heat exchanger for the purpose of this project.

Chapter 5

Combustor Design

“Agnosco veteris vestigia flammae”
- I feel again a spark of that ancient flame
— *Virgil(70-19 BC) - Aeneid IV*

The combustor is the device in which a zone is established where the fuel-oxidizer mixture is burnt and chemical energy is released. Broadly speaking, combustors are designed on the basis of whether the fuel is premixed with the oxidizer or not. Most conventional combustors, such as those employed in aircraft or industrial power plant gas-turbine engines, use fuel that is not premixed with the oxidizer (air). The fuel is stored in tanks, and at the time of operation of the gas-turbine, is introduced into the combustor where it is mixed with the air at the desired proportions and then burnt. As the fuel is essentially separate from the air, within various regions in the combustor, it is possible to vary the equivalence ratio ϕ of the fuel-air mixture as desired. Typically, a conventional combustor comprises three zones as shown in Figure 5-1 (Ref[16]). In the *primary zone*, the fuel-air mixture is stoichiometric or slightly rich to achieve flame stability and sufficient time, temperature and turbulence is provided for the evaporation of the liquid fuel and its mixing with air. The

intermediate (secondary) zone performs two functions. At low altitudes (such as in industrial gas-turbines) it serves as a region in which dissociation losses (which are the result of the chemical instability of the combustion products at high temperatures) in the gas flow can be recovered, and the burning of any imperfectly mixed fuel-rich pockets of gas completed. At high altitudes (such as in aircraft gas-turbine engines), the rate of reaction in the primary zone is slower, owing to the lower pressure and concentration of oxygen, and combustion is usually not completed in the primary zone. Under these conditions, the intermediate zone serves principally as an extension of the primary zone, providing increased residence time at a high temperature. The role of the *dilution (tertiary) zone* is to admit air so that the products of combustion, which are typically at a temperature of 2400 K, may be cooled to a temperature acceptable to the turbine since conventional metallurgy of turbines can withstand a temperature of about 1300 K for stationary and about 1500 K for flying gas-turbines.

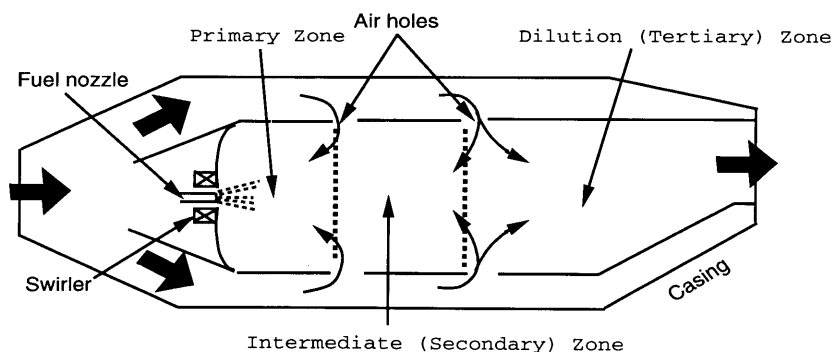


Figure 5-1: Zones in a conventional gas-turbine combustor. *Primary Zone*: combustion takes place and flame is stabilized. *Intermediate Zone*: combustion process is completed by addition of more air. *Dilution Zone*: cooling down the products of combustion (Ref[16])

On the other hand, since fuel and oxidizer are not physically separate in premixed gases, it is

harder to vary the equivalence ratio ϕ ; in many cases it is actually undesirable or impossible. This is especially true of ultra-lean fuel-air mixtures, where the fuel content in the mixture is very low so that the mixture is termed as a low calorific-value or low BTU content fuel. An example of this kind of fuel-air mixture is the mine ventilation gas which is the subject of this project. This gas is an ultra-lean mixture of methane in air with the methane content about 2% of the mixture (this is $\phi \approx 0.2$) by volume at standard conditions; the methane volume content may sometimes be as low as 1% ($\phi \approx 0.1$). Addition of methane to this mixture to raise the equivalence ratio is possible although not economical if the combustor is properly designed to burn ultra-lean mixtures.

The aim of this chapter is to suggest an effective combustor design to burn the ultra-lean fuel-air mixture described above that can also be incorporated easily as a modification to the GS-350 gas turbine. As mentioned in Chapter 4, a detailed mechanical design of the combustor including strength, thermal stresses, vibration analysis or fouling will not be attempted. However, if necessary, qualitative accounts will be taken of these factors.

5.1 Requirements for the combustor that would burn ultra-lean methane-air mixtures

As in the case of the heat exchanger, there are demands and constraints on the design of the combustor which are enumerated below:

1. As described in Section 1.5 and Figure 2-2 the temperature of the methane-air mixture must be raised to a minimum, T_3 , before spontaneous ignition can be sustained. As discussed Chapter 4, the temperature rise may be effected by means of a heat exchanger. Within the combustor, perfect mixing of the reactants with the products is necessary to realize stable burning. The perfect mixing is achieved in the combustion zone, which can be idealized as

a perfectly stirred reactor as described in Chapter 2. Moreover, within the combustor, the time of mixing of products and reactants is assumed zero. This approximation introduces a small error in the analysis. However, most practical systems approach this idealization. An effective combustor design must, therefore, primarily provide a *mixing region*.

2. From Figure 2-6, the flame temperature T_5 , which is the overall temperature of the stirred reactor region (see Figure 2-1), can be considered virtually constant when *sufficient residence time* τ_r is provided for the chemistry to proceed to completion. This constant flame temperature T_5 is 1500 K. This is supported by the observation that the temperature drop of the hot gases from the flame to the exit of the combustor is negligible (Section 5.7).
3. The combustor must fit within practical *size constraints*. Similar to the heat exchanger, a reasonable assumption is that no dimension of the combustor be greater than 1 m.
4. It must also be designed so that the *pressure-drop penalty is low*. For combustors, the tolerated limit of pressure-drop is 4% (Ref[22]) of the inlet pressure to the combustor (4 atm in this case).
5. The combustor must be *structurally compatible* with the heat exchanger. In addition, it must also be designed to withstand vibrations leading to resonant motions that occur frequently in premixed combustion.

5.2 Types of ultra-lean combustors

The problem of ultra-lean combustion is not new and there exist a number of designs which have been used. Of the designs, there are few basic types which are described below:

5.2.1 Swiss Roll combustor

The Swiss Roll (Ref[32]), shown in Figure 5-2, is an integrated heat exchanger-combustor. This is shaped in the form of a spiral with the reactants and products flowing in adjacent coils. The purpose of the spiral is to act as a counterflow steady-flow heat exchanger (Section 4.5.3). Combustion takes place in the cavity at the center of the spiral. Ultra-lean mixtures with volumetric methane concentrations as low as 1% in air have been burnt in this type of combustor when the spiral was made long enough (8 turns). This design also provides a robust method for stabilizing the flame in the cavity and preventing flash-back. If flash-back is to occur, the flame would initially move into the heat exchanger, decreasing the heat exchanger's length. This automatically restores the flame position to the center of the cavity.

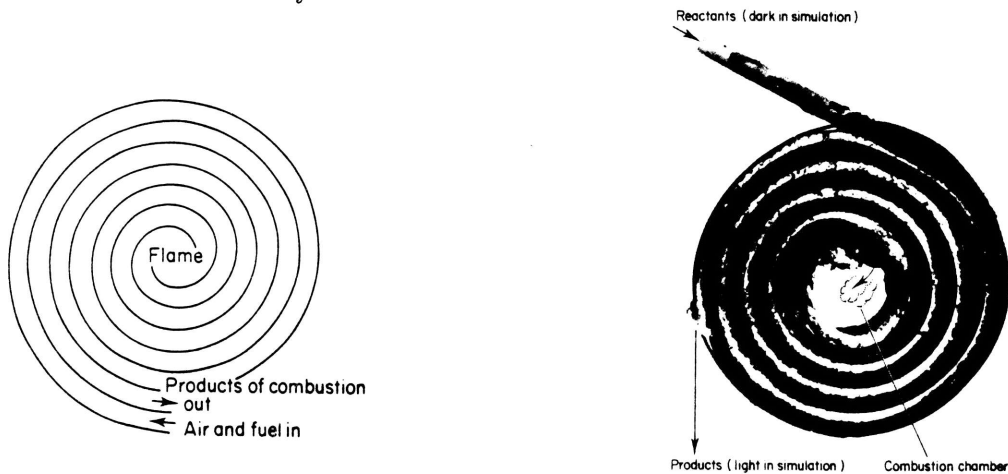


Figure 5-2: The Swiss Roll (Ref[32]). It is an integrated heat exchanger and combustor. The spiral acts as a counterflow heat exchanger and combustion takes place in the cavity at the center of the spiral

Advantageous though this design is from the point of view of combustion, the Swiss Roll has inherent structural problems. For the heat exchanger to be efficient enough so as to reduce loss of energy by conduction through the walls of the spiral, the walls must be made as thin as possible.

Due to the average difference of temperature between the product and reactant streams, which becomes greater as the equivalence ratio is reduced, unequal expansion occurs on the reactant and product side of the spiral, leading to structural failure at the welded joints.

5.2.2 Swirl Combustors

Here the main mechanism for stabilizing the flame in the combustor is swirl. The mechanism of swirl is explained in detail in Section 5.4. Suffice to say here that at high swirl, a reverse-flow region, into which fluid is entrained and where it spends the mixing time τ_m and chemistry time τ_r is established. Swirl is induced by simultaneous tangential flow and axial flow. There are two mechanisms by which this simultaneous flow can be induced. Depending on the mechanism of imparting of swirling flow, there are two basic types of swirl combustors:

5.2.2.1 Axial-tangential swirl combustor: The Cyclone Combustor

A schematic of this combustor is shown in Figure 5-3 (Ref[8]). The combustor is cylindrical with tangential inlets in the cylindrical region. As shown, the main flow is split between the axial part and tangential part. The induction of swirl due to the simultaneous tangential and axial flow sets up an aerodynamic recirculation close to the wall in the form of a thin annulus along the whole length of the tube. The cylindrical region is either lined or made of the refractory material which attains a high temperature under steady combustion of the reactant stream. The recirculation region stabilizes the flame in the annulus as shown.

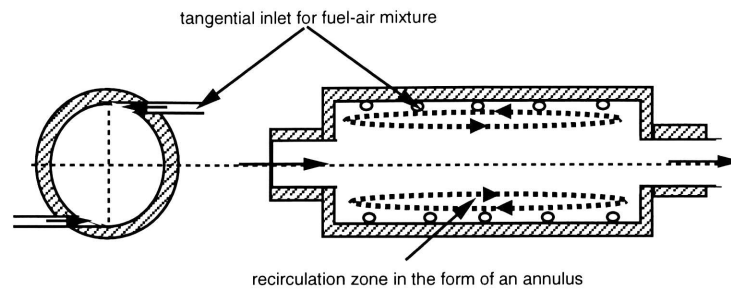


Figure 5-3: A cyclone combustor where the fuel-air mixture is fed both axially as well as through tangential inlets as shown. Swirl sets up a recirculation region close to the wall in the form of an annulus (Ref[8])

This kind of combustor was first constructed to burn poor or low heat content fuels such as wheat husk. Due to the long residence time attainable in the annular recirculation region of the combustor, it is theoretically possible to burn extremely low BTU fuels.

However, an inspection of the method of swirl induction shows that it is induced by tangential flow that is initiated by diverting some of the flow through tangential inlets. Tangential inlets are difficult to make in refractory material (often ceramic), are difficult to fabricate and the interruptions in the combustor geometry can be sources of structural failure (Ref[29]).

5.2.2.2 Axial flow swirl combustor: The Swirler Combustor

A schematic of this combustor is shown in Figure 5-4 (Ref[8]). Swirl is imparted on the axial flow by means of a swirler, a device that consists of a number of blades to divert the flow tangentially (the use of the swirler device gives this combustor its name). The swirl induced at the swirler is locally small, but when the geometry expands at the furnace region, a central recirculation region is set up in which the flame is stabilized (mechanism explained in detail in Section 5.4). The furnace, which has a cylindrical geometry, is lined with a refractory material that can not only withstand the high

temperatures of combustion but also prevents heat loss from the flame to the surroundings.

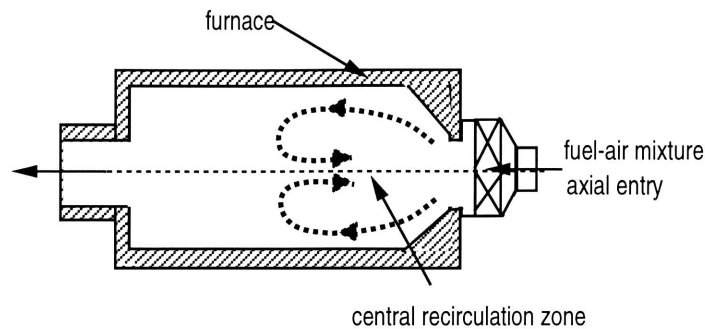


Figure 5-4: A basic swirler combustor. A central recirculation region is established downstream of the swirler where the flame is stabilized and mixing takes place. The furnace is usually lined with refractory material (Ref[8])

Note that the swirler combustor is similar to the conventional combustor shown in Figure 5-1 with the exception that the entire flow is directed through the swirler. The mechanism and function of swirl generation is the same in both cases.

In order to burn ultra-lean fuel-air mixtures, the basic swirler combustor has been modified to incorporate some additional features. Figure 5-5 shows the swirler combustor with the addition of a center bluff body (Ref[1]). Used separately, a bluff body creates a recirculation region. When used in conjunction with a swirler, a stronger recirculation region is expected. The addition of the bluff body also negates some of the detrimental effect of the confinement on the swirl recirculation region in the combustor center (explained in Section 5.4). The confinement is the result of the walls of the combustor. For the same inlet conditions, and at a particular swirl number (defined in a later section), the size of the recirculation zone created in an unconfined environment is always greater than that in confined flow; confinement therefore has a negative effect on the size of the recirculation zone (Ref[28]).

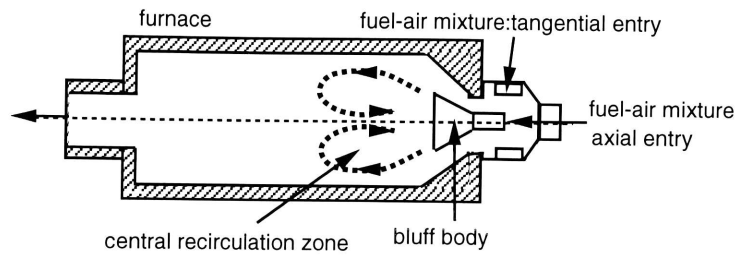


Figure 5-5: Swirler combustor with the addition of a bluff body. It is used in conjunction with the swirling mechanism to create a very strong recirculation region (Ref[1])

Figure 5-6 shows a modification using a pilot burner that allows for the startup of the combustor unit using natural gas. The pilot burner is recessed within the main waste gas burner. When steady state combustion is reached, the natural gas supply is turned off. However, the addition of the auxiliary burner within the basic combustor design complicates the design.

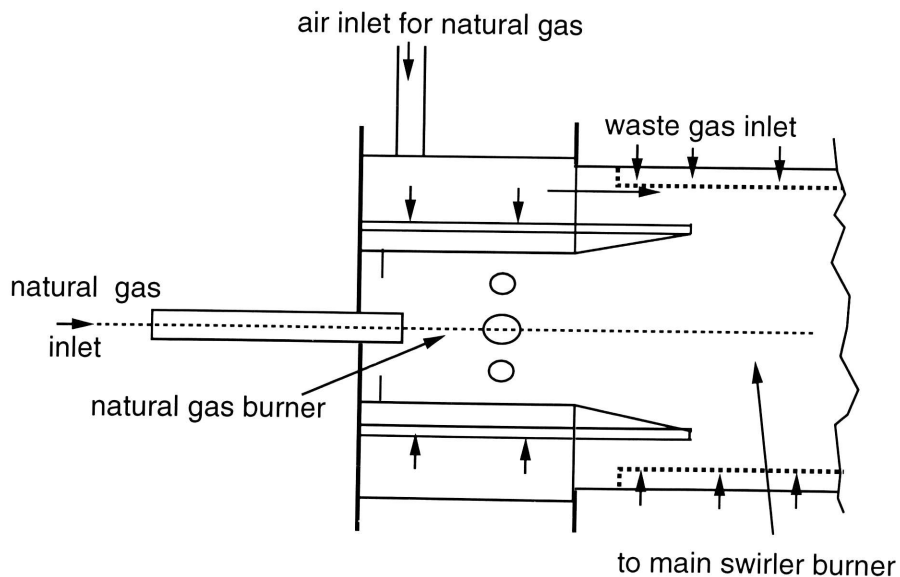


Figure 5-6: Modification to the swirler combustor to use natural gas as a pilot fuel. It is also referred to as a dual-gas burning combustor (Ref[29])

5.3 Choice of ultra-lean combustor

The combustor design must be as simple as possible without sacrificing performance. From the descriptions of the two basic types of ultra-lean combustors, it can be seen that the Swiss Roll and Cyclone combustors are both more complicated to fabricate and more prone to structural failure than the Swirler combustor. Also, swirlers have been commercialized and data which describe their performance are available in greater detail. This is because conventional combustors, which largely have similar design, use swirlers to a great extent.

Therefore, for the purpose of this project, the basic swirler combustor is adopted. Modifications, if necessary will be implemented in the design in later sections. The mechanism of swirl, which is central to the design of the combustor, is described in detail in the next section.

5.4 Understanding the mechanism of swirl

The mechanism of swirl flow is central to understanding the conditions under which a flame may be stabilized in a combustor.

Swirling fluid flow can be considered as being composed of two parts: an axial flow (with a local axial velocity U) and a tangential flow (with a local velocity v). The establishment of a recirculation region depends on a number of parameters, one of which is the strength of the tangential component of velocity v .

The local fluid velocity in the reverse flow (or recirculation) zone is much lower than the velocity of the fluid at the inlet of the combustor. Since flame speeds are also lower than fluid flow speeds, the recirculation zone is useful in anchoring the flame during combustion and preventing blow-out.

Not all the combustible material that enters the combustor is entrained into the recirculation

zone. It is, however, desirable that this entrainment be as high as possible. Since the entrainment of fluid into the recirculation zone is proportional to its size (Ref[1]), it is essential to ensure that the recirculation zone is as big as possible.

The size of the recirculation zone is influenced by a number of parameters which are described in the following subsections. In each case, effort has been made to develop quantitative trends of these parameters. Conclusions made from these quantitative trends will be employed to determine the size and shape of the combustor for this project.

An experimental setup frequently used to study the basic nature of swirling flow is shown in Figure 5-7. Figure 5-7 shows flow within a straight pipe to which swirl has been imparted. The degree of swirl inside the pipe is not enough to create a recirculation region within it (the degree of swirl will be clear in the next section). The Reynolds number of the flow Re_s , is based on the bulk axial velocity component U and diameter of the exit of the pipe D_e (which is the same everywhere in the case of a straight pipe, but not so in case of a divergent pipe). The flow is exhausted into an unconfined environment. Assuming that Re_s is in the turbulent range (the reason will be clear later), a recirculation region is established close to the exit as shown.

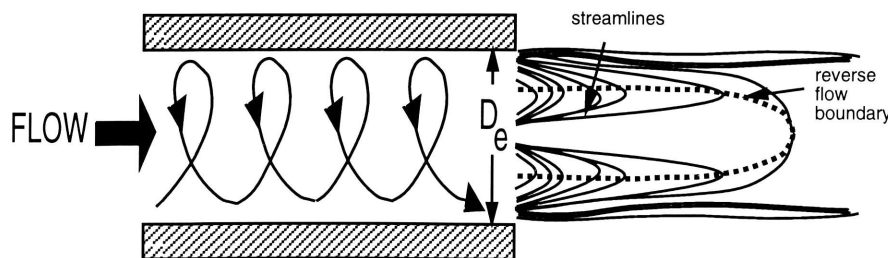


Figure 5-7: basic geometry used to study swirling flows with a straight exit and issuing into an unconfined environment

5.4.1 Degree of swirl: the swirl number S

As mentioned in previous sections, swirl is generated by simultaneous tangential and axial flow. To express the degree of swirl, a swirl number S has been defined as (Ref[27]):

$$S = \frac{2G_\phi}{G_\theta D_e} \quad (5.1)$$

where G_ϕ is the axial flux of angular momentum

$$= \int_0^{\frac{D_e}{2}} (2\pi r \rho u dr) v r$$

G_θ is the axial flux of linear momentum

$$= \int_0^{\frac{D_e}{2}} (2\pi r \rho u dr) u$$

and where D_e = the exit diameter of flow from which swirl is created

u = local axial velocity

v = local tangential velocity

From the definition, it can be seen that S is a similarity criterion that intuitively represents the strength of the tangential flow to the strength of the axial flow and that the greater the strength of the former, the greater is the swirl number S .

5.4.2 Conditions under which a recirculation zone is established

The physical phenomenon that heralds the onset of the reverse flow is an instability called *vortex breakdown*.

Vortex breakdown is a transition stage phenomenon that has been investigated for laminar swirling pipe flows in Ref[18],[26]. The basic features of this flow is shown in Figure 5-8 (constant S). At low Reynolds number Re_s , shown in Figure 5-8a, a small bubble of recirculating fluid appears on the axis of symmetry (shown as streamlines). When Re_s is increased as in Figure 5-8b, the contours of streamlines are qualitatively similar to those in Figure 5-8a, but the streamlines downstream of the vortex indicate the presence of a "centrifugal wave". This wave is associated with the development of positive tangential vorticity component. When Re_s is increased further, as in Figure 5-8c, the amplitude of these waves increase and the wavelength decrease. With the increased amplitude and decreased wavelength, the associated axial deceleration is enough to cause the flow to stagnate under the crest of a wave. Within this stagnant region is found a near spherical region of recirculating fluid which is termed a vortex breakdown bubble. The trend is continued when Re_s is increased further and the recirculation bubbles grow in size and the wavelength becomes shorter. The shortening of the wavelength (leading ultimately to a coalescing of the two bubbles) also leads to the upstream migration of the leading bubble. The production of further recirculation regions downstream proceeds in the same manner.

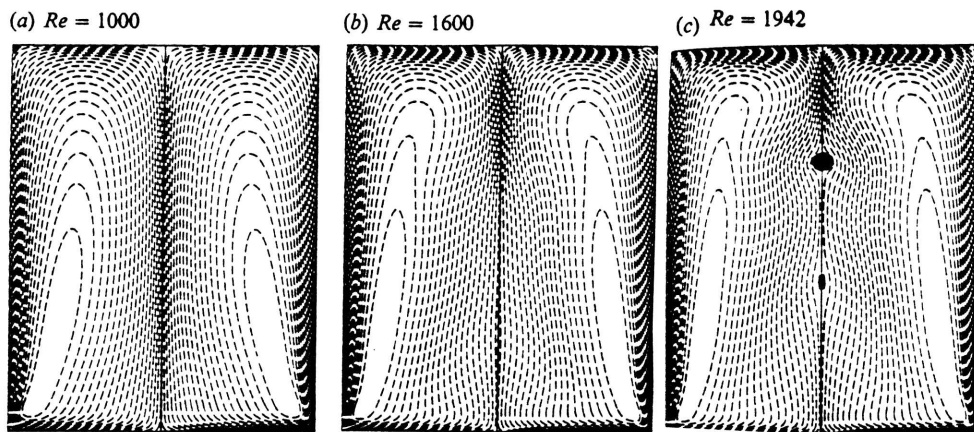


Figure 5-8: Vortex breakdown in cylindrical flow with rotating endwall

- (a) $Re_s = 1000$
 - (b) $Re_s = 1600$ and
 - (c) $Re_s = 1942$
- S is constant.

The physical mechanisms responsible for vortex breakdown can be qualitatively understood by an inspection of the governing equations of steady, inviscid axisymmetric swirling flow (Ref[18]). In terms of the radial pressure gradient and the centrifugal force, the other radial accelerations can be derived from the momentum equation as (Ref[18]):

$$v \frac{\delta v}{\delta r} + w \frac{\delta u}{\delta x} = \frac{u^2}{r} - \frac{1}{\rho} \frac{\delta p}{\delta r} \quad (5.2)$$

where u , v , w are the components of velocity,

p is the pressure and

ρ is the density

Downstream of a point where the radial velocity v is zero (or more generally downstream from a region in which the flow is cylindrical), there will be divergence of the streamlines (positive $\frac{\delta v}{\delta r}$ only if the centrifugal force exceeds the pressure gradient $\frac{\delta p}{\delta r}$). For the confined flow, this arises from the fact that as a particle of fluid moves downstream, it loses most of its angular momentum that it acquired upstream through the action of viscous stresses in the boundary layer near the surface of the confinement (Ref[18]).

Since the stream function ψ is determined, by definition, in axisymmetric flows (Ref[18]) as $u = -\frac{1}{r} \frac{\delta \psi}{\delta x}$ and $w = \frac{1}{r} \frac{\delta \psi}{\delta r}$, it follows that:

$$u = w\sigma'(x) \quad (5.3)$$

where $r = \sigma(x)$ is the radius.

The reason for the initial overshoot in the divergence and subsequent waviness seen in Figure 5-8 can be seen from the equation involving the circulation Γ , stream function ψ and the total pressure head \mathcal{H} (Ref[18]):

$$\frac{\delta v}{\delta x} = \frac{\Gamma}{r} \frac{d\Gamma}{d\psi} - r \frac{d\mathcal{H}}{d\psi} + \frac{\delta w}{\delta r}$$

Assuming that at $x = x_0$, where $v = 0$, and $\frac{\delta v}{\delta x}$ has a local extrema, where a stream surface has the smallest radius, then on a particular stream surface where the radius $r = \sigma(x)$ whose radius is $\sigma = \sigma_0$ at $x = x_0$ can be written as (Ref[18]):

$$\left. \frac{\delta v}{\delta x} \right|_{\sigma} - \left. \frac{\delta v}{\delta x} \right|_{\sigma_0} = A \left(\frac{1}{\sigma} - \frac{1}{\sigma_0} \right) - B(\sigma - \sigma_0) + \left. \frac{\delta w}{\delta r} \right|_{\sigma} - \left. \frac{\delta w}{\delta r} \right|_{\sigma_0} \quad (5.4)$$

where A and B are the particular values of $\Gamma d\Gamma/d\psi$ and $d\mathcal{H}/d\psi$ on this stream surface.

A linear approximation of $\frac{\delta u}{\delta x}$ is made from equation 5.3 (Ref[18]) as:

$$\frac{\delta u}{\delta x} = w\sigma''$$

From the above equations, it can be seen that immediately downstream of x_0 , the diverging stream implies an increasing radius of curvature σ and therefore a decreasing σ'' . However, the last two terms on the right hand side of equation 5.* are positive because the diverging stream, by continuity, implies a reduction in w . The continued divergence leads to a condition where the local slope σ' is a maximum or σ'' is zero. Since the flow continues to diverge downstream from this point, σ'' becomes negative and the stream surface begins to reduce in slope, turning back towards the axis, resulting in the wavy pattern. Increase in Re_s decreases the tangential component of vorticity until it becomes negative (Ref[18]) on some stream surfaces. This negative component is responsible for bringing the axial velocity to be brought down to zero. This can be intuitively understood from the vorticity equation for axial velocity (Ref[18]):

$$U(r) = -\frac{1}{4\pi} \int \frac{s x \omega(r')}{s^3} dV \quad (5.5)$$

where $s = r - r'$

The occurrence and position of the vortex breakdown region was shown to be a function of both Re_s and S (Ref[27]). Figure 5-9 shows the variation of Re_s with axial position $\frac{x}{D_e}$ for various swirl numbers S . This figure was generated for a specific swirl generator, but is found applicable in other cases of swirl generation as well. (Ref[27]).

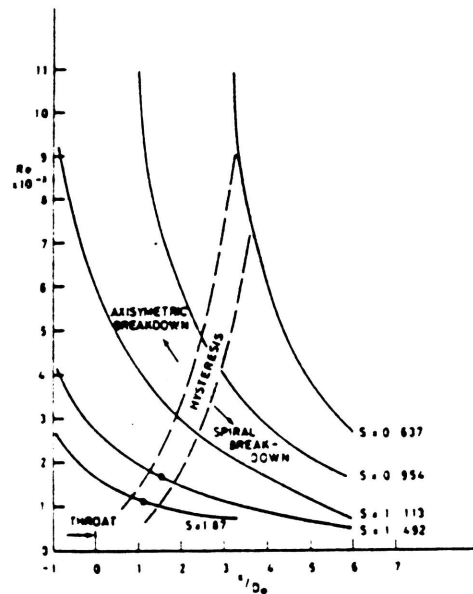


Figure 5-9: Variation of Reynolds number Re_s , against axial position $\frac{x}{D_e}$ for various swirl numbers S (Ref[27])

For the purpose of design of a swirl combustor, it is important to ensure that for a given swirl number, the Reynolds number is outside the region of initial vortex breakdown such that a reverse flow is established. For a swirl number $S = 1$, and the distance from the swirler is zero ($\frac{x}{d_e} = 0$), $Re_s \approx 13000$ is necessary for vortex breakdown to develop (from Figure 5-8). To ensure the establishment of the recirculation region, therefore, $Re_s > 13000$ (for $S = 1$).

In this present setup, the Reynolds number is typically of the order of 10^6 . The combustor will be designed for $S \approx 1$. Thus, a recirculation zone will be established in the combustor to be designed.

5.4.3 Size of the recirculation region

The size of the recirculation region depends on a number of factors that are influenced by the geometry and the flow parameters as mentioned below:

5.4.3.1 Straight exit and unconfined environment

The study of swirling flows can be derived from the basic geometry shown in Figure 5-7. This geometry has a straight exit and the flow issues into an unconfined environment.

Experimental evidence shows that the torroidal region in the case of the flow shown in Figure 5-7 is formed at the exit and occupies upto about 75% of the exit diameter (Figure 5-10).

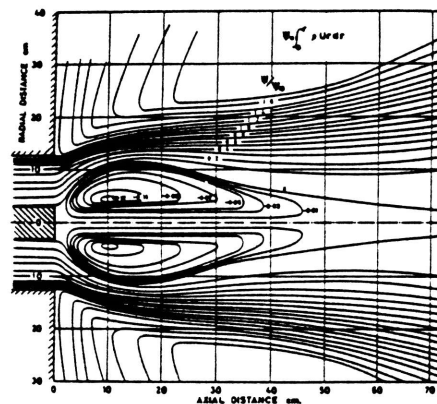


Figure 5-10: Streamlines of central torroidal recirculation region when $S = 1.57$ (Ref[27])

Figure 5-11 shows that the length of the recirculation region X ; in the case of a straight exit, $X/D_e \approx 2 - 4$ at most swirl numbers (assuming that Re_e and S are sufficient enough to be outside the region of initial vortex breakdown) (Ref[27]). However, the variation in X with increasing S is not monotonic. When the swirl number is about 0.6, the initial recirculating zone is long and thin with X of the order of $2D_e$. As the swirl number is increased to about 1.6, X first increases to about $5D_e$. This is because, increased swirl causes a stronger recirculation and consequently more fluid is entrained into the reverse flow region. As the swirl number is increased further, however, X decreases to about $2D_e$ and further to $5D_e$ by $S = 2.4$ with the diameter of the recirculation region

becoming larger as the swirl number is increased even further. This is because beyond a certain degree of swirl, the adverse axial pressure gradient is strong enough to resist the change in length of the recirculating region. Since recirculation is stronger because of the higher swirl number, more fluid is entrained from the surroundings; the adverse radial pressure gradient not being as strong as the axial pressure gradient, the diameter of the reverse flow zone increases.

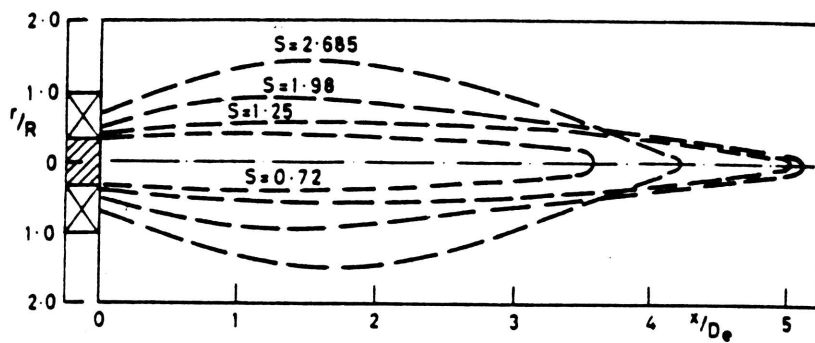


Figure 5-11: Variation of the length of recirculation region against axial distance (Ref[1])

5.4.3.2 Effect of a divergent exit

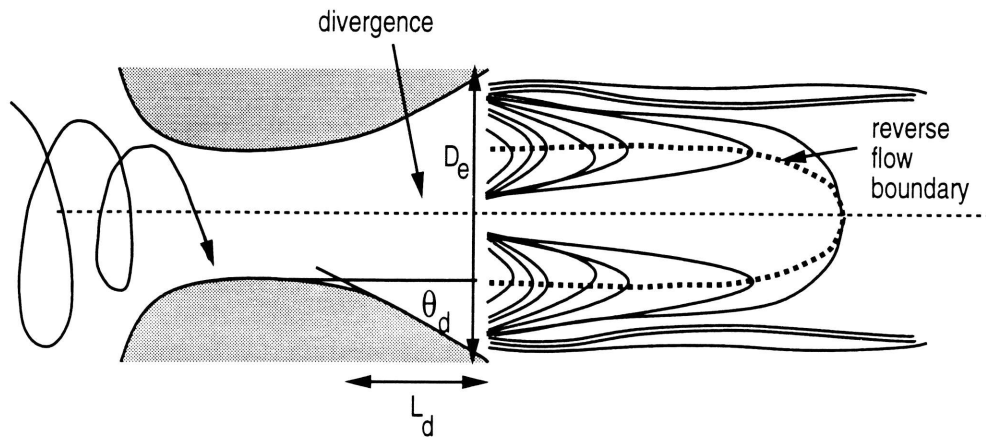


Figure 5-12: Addition of a divergent exit in swirl flow

The general effect of a divergent exit is to increase the size of the recirculation region for the same inlet conditions as a non-divergent exit (Ref[27]). This is because divergence causes an expansion in fluid flow which reduces the axial momentum and therefore increases the swirl number S according to equation 5.1. The increase in size of the recirculation zone then follows the pattern observations in the previous section. Half angle of divergence θ_d has been taken from experimental considerations. Best results have been obtained when θ_d is shallow and of the order of 10° (Ref[27]). The length of the divergence L_d also has an effect on M_{rr} . Experimental evidence (Ref[27]) suggests that the larger the ratio $\frac{L_d}{D_e}$, the greater M_{rr} is. The data varies the ratio $\frac{L_d}{D_e}$ from 0.53 to 3 (Figure 5-13). However, it has been found (Ref[27]) that a relatively short divergence ($\frac{L_d}{D_e} \approx 0.7$) more than doubles the diameter of the recirculation region. This result and that size constraints restrict the design of the combustor, the ratio $\frac{L_d}{D_e}$ has been chosen as 0.7 for the combustor in this project.

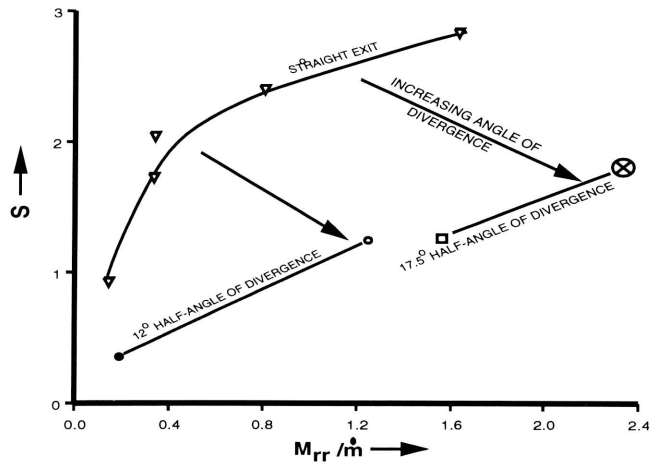


Figure 5-13: Variation of non dimensional recirculated mass flow rate $\frac{M_{rr}}{\dot{m}}$ with swirl number for various angles of divergence: $\bullet \frac{L_d}{D_e} = 0.53$; $\circ \frac{L_d}{D_e} = 2$; $\square \frac{L_d}{D_e} = 1.6$; $\otimes \frac{L_d}{D_e} = 3$ (Ref[27])

5.4.3.3 Effect of confinement

The confinement ratio D_f/D_e (See Figure 5-21) plays an important role in the size of the recirculation region.

It has been observed that, for the same inlet conditions, a confinement has a detrimental effect on the size of the recirculation region (Ref[28]). It was also observed that for high confinement (defined by H/R - cylinder height to radius ratio Ref[18]), vortex breakdown (that heralds the onset of recirculation) did not occur until the Reynolds number Re_s is increased (for the same inlet swirl number S) (Ref[27], Figure 5-9).

The sudden expansion of fluid from the exit to environment in the confinement (Figure 5-21) results in the appearance of a small annular recirculation zone in addition to the main central reverse flow (Ref[27], Figure 5-23, 5-24).

This annular recirculation region has been found to be considerably weaker than the main central recirculating zone (Ref[27], Figure 5-23, 5-24). Thus at some confinement ratios D_f/D_e and swirl numbers S , the pressure gradient that establishes the annular recirculation region becomes weaker than the pressure gradients that are responsible for the central recirculation region; the annular reverse flow zone may become very small and the central recirculation zone may appear to extend to the walls of the confinement. Experimental evidence (Ref[27]) suggests that there are three regimes of swirl number where the effect of confinement can be seen.

When $0.6 < S < 1.6$, the effect of the outer recirculation region is to reduce the size of the central reverse flow region as the ratio $\frac{D_f}{D_e}$ becomes smaller. In order that the outer recirculation region may not have significant impact on the size of the central recirculating region, it has been experimentally suggested (Ref[27]) to limit the ratio $\frac{D_f}{D_e} = 2$.

When $1.6 < S < 2.4$ is a transition zone where the confinement actually increases the central recirculated mass flow (compared to when $0.6 < S < 1.6$) since the outer region of recirculation is diminished by the stronger central reverse flow. This occurs, because, upon leaving the exit (of diameter D_e in Figure 5-21), the swirling flow is so strong that the pressure gradients in the central reverse flow overcome the pressure gradients of the annular reverse flow zone. This increase in size due to “sticking” of the flow to the walls of the confinement may appear beneficial in terms of mass flow rate of entrainment into the central reverse flow zone, but increased penalties of pressure drop due to fluid friction makes this situation undesirable (Ref[27]).

When the swirl number is increased further i.e $S > 2.4$, the effect of the confinement is to monotonically diminish the size of the reverse flow zone as the flow continues to stick to the confinement upon exhausting from the exit (Figure 5-21). As mentioned earlier, the pressure drop penalty is high. Therefore, it is undesirable to apply $S \geq 2.4$ (Ref[27]).

It must be noted that the size of the recirculation zone in confined flow is always less than the corresponding size of the reverse flow zone when the flow is unconfined regardless of the level of confinement. The effect of confinement can only be optimized to achieve the biggest central recirculation zone with the least pressure drop penalty.

As mentioned in Section 5.4.1, the swirl number $S = 1$ and the flow Reynolds number Re_s , chosen for the project will always ensure vortex breakdown and consequently central reverse flow. However, from the above evidence, it can be seen that this choice of swirl number will produce an outer annular reverse flow zone that tends to diminish the central reverse flow. In order to minimize the effect of this outer annular reverse flow, as has been suggested, the ratio $\frac{D_t}{D_e} = 2$.

5.4.3.4 Effect of a bluff body

When an obstacle is placed in the flow of a combusting fluid, the flow velocity is reduced in the boundary layer near the solid wall and the chances for the flame speed to match the flow velocity at some region in the flow field - a requirement for flame stabilization since flame speeds are very much less than flow speeds - are improved. If the obstacle is non-streamlined, such as in a bluff body, then a flow condition is reached downstream of the obstacle where the adverse pressure gradient is strong enough to cause separation from the boundary layer and set up a recirculating vortex in the wake of the bluff body (Figure 5-14).

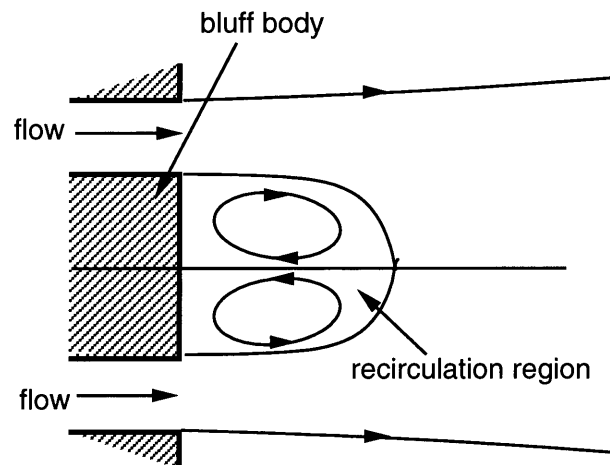


Figure 5-14: Effect of a bluff body on pure axial flow. A central reverse flow region is set up (Ref[1])

This effect of the bluff body in creating a reverse flow has been combined to strengthen the central recirculation region that is created by highly swirling turbulent flow. This is advantageous when the swirling flow is confined and the recirculation region near the walls of the confinement diminishes the central toroidal region.

Thus, swirler combustors, such as that illustrated in Figure 5-5 combining the effects of the

swirler and the bluff body have been constructed. Figure 5-15 shows the increase in the strength of the reverse flow by the addition of a bluff body to the swirling flow for a particular design of this type.

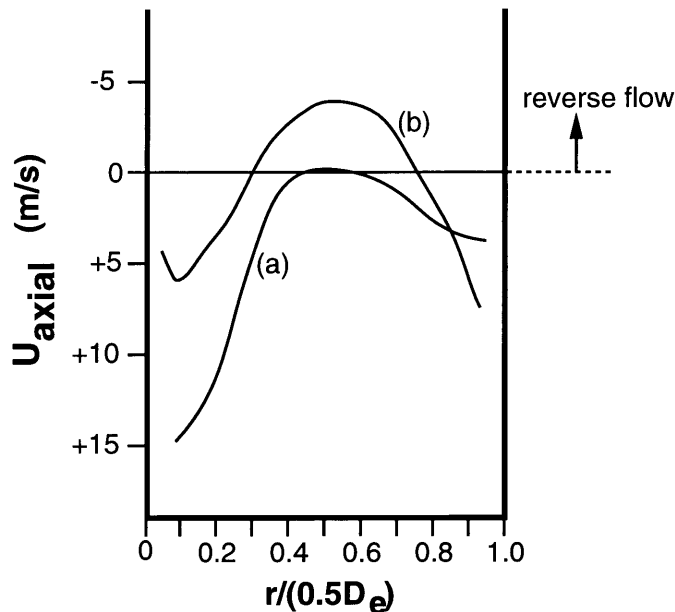


Figure 5-15: Radial variation of axial velocity at point $0.69D_e$ downstream of the swirling flow (a) $S = 1.36$ and no bluff body (b) $S = 0.92$ and with bluff body. $\dot{m} = 1.77 \text{ kg/s}$ for both cases (Ref[1])

The addition of a bluff body as in Figure 5-5 increases the local axial velocity and also increases the pressure drop across it. Unless the bluff body is optimally positioned, the increase in pressure drop can be more disadvantageous than the increase in the size and strength of the recirculation region. For the bluff body shown in Figure 5-5 and whose axial velocity data are presented in Figure 5-15, the optimal position of the bluff body has been experimentally determined. In most cases, this is a complicated and costly process.

It has been shown in Section 5.4 that for the purpose of this project, S and Re_e have been chosen so that a recirculation region will always be established. The addition of a bluff body will

also increase the mechanical complexity of the combustor as well as increase the pressure drop across the combustor. Hence the usage of a bluff body in the combustor design for this project is unnecessary.

5.4.4 Effect of type of swirler on swirl flow

There are two types of swirlers: straight-vane and profiled-vane swirlers. The effectiveness of each type of swirler can be defined by a common parameter - the efficiency of swirl generation η . η is defined as the ratio of the flux of kinetic energy of the swirling flow through the swirler to the pressure drop across the swirler (part of the pressure drop appears as fluid friction losses).

Figure 5-16 shows the variation of efficiency of swirl generation η against swirl number S for straight-vane and profiled-vane swirlers. It can be seen that when profiled vanes are used in place of straight vanes, the efficiency of swirl generation is increased by almost a factor of three (Ref[27]). It has also been found that there is little difference in the non-uniformity of flow at the exit of the two types of swirlers (Ref[27]).

Therefore, profiled-vane swirlers are chosen for the purpose of this project. The detailed design of this swirler will be described in a later section.

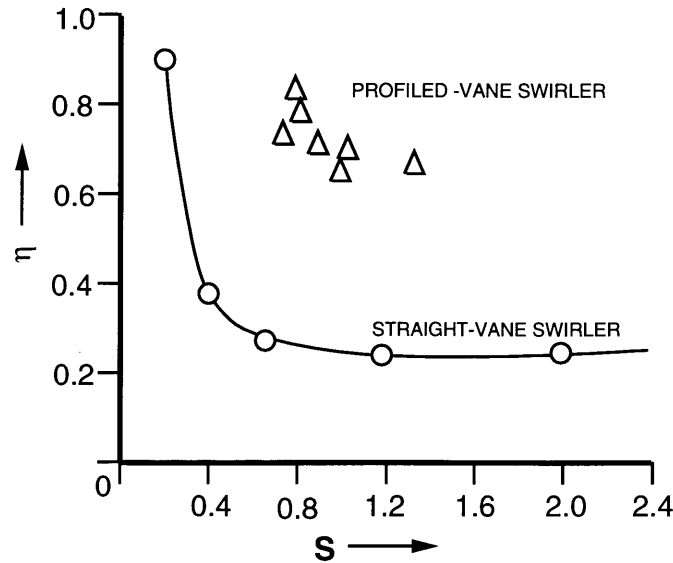


Figure 5-16: Variation of efficiency of swirl generation η against swirl number S for straight-vane and profiled-vane swirlers (Ref[27])

5.4.5 Precessing Vortex Core (PVC)

Following vortex breakdown that heralds the onset of recirculation (Section 5.4.1), the initial forced vortex (explained in Section 5.4.1) degenerates into a Rankine vortex (the Rankine vortex has a central core of forced vortex or solid body rotation) and an outer free vortex¹. The central forced vortex region of the Rankine vortex then starts to precess about the axis of symmetry and this precessing vortex core (PVC) is found to be responsible for the initial high levels of turbulence measured in the area surrounding the central recirculating zone (see Figure 5-17).

As the PVC leaves the swirler, its divergence from the axis of symmetry continues so that by about 2 exit diameters downstream, much of the effect of the PVC is dissipated (Ref[27]).

¹in a free vortex, a particle of fluid does not rotate about its axis; the tangential velocity $v = \frac{C}{r}$ where C is a constant and r is the radius of the vortex



Figure 5-17: Water model of swirling flow from a straight exit into an unconfined environment. Path of the polystyrene clearly shows vortex core precession (Ref[27])

As a result of the precessing vortex core, the flow is actually highly three-dimensional and is not axisymmetric as is often assumed. The PVC precesses about the axis of symmetry at a particular frequency. Comparison of the frequency of the PVC and the mean tangential velocity profile at the exit plane shows that at the radius of the vortex core precession, the frequency of the PVC gives the measured mean tangential velocity at that radius with the assumption of a forced velocity distribution according to the relation (Ref[27]):

$$f = \frac{v}{r_p}$$

where v is the tangential velocity, r_p is the radius to the PVC and f is the frequency of precession of the PVC.

The precession of the PVC in some cases also causes the periodic shedding of radial-axial eddies

from the edge of the exit as shown in Figure 5-18. The precession is responsible for the burner noise (Ref[27]) that is usually heard in swirl combustors. If the frequency of precession happens to be close to the natural structural oscillation frequency of the combustor, it may vibrate violently due to the phenomenon of resonance.

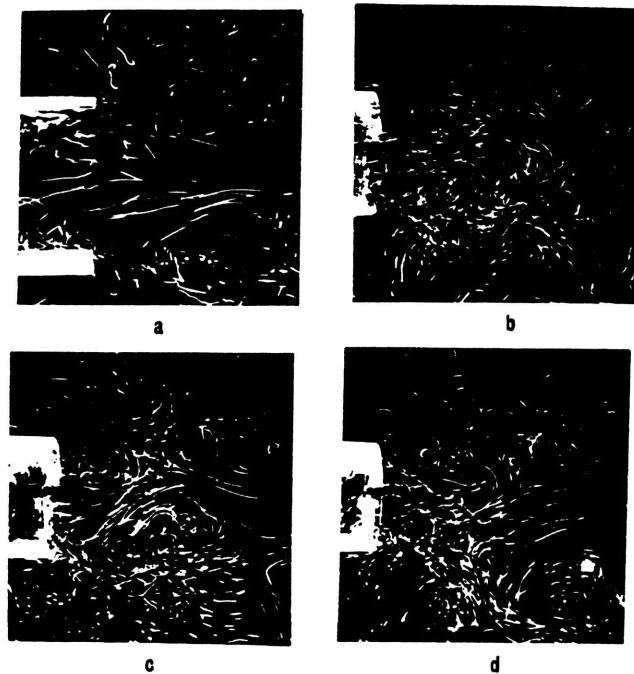


Figure 5-18: Progressive shedding of radial-axial eddies due to the PVC (Ref[27])

5.4.6 Effect of combustion on swirler combustor performance

When premixed fuel-air mixture is used (as is the case in this project), the precessing vortex core (PVC) has been found to occur at higher amplitudes (Ref[27]). Measurements also show evidence of a three-fold increase of the PVC frequency in reacting flow over cold flow and a very short and intense noisy flame is produced (Ref[27]). Figure 5-19 shows the variation of frequency f of the PVC against the Reynolds number based on the exit diameter Re_e (Ref[27]). It can be seen that f is about three times that of the cold flow PVC frequency (Ref[27]).

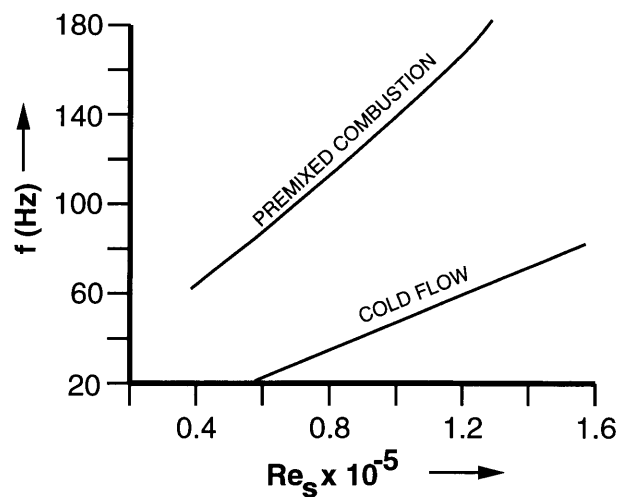


Figure 5-19: Variation of the frequency f of the PVC against Re_s for cold (isothermal) flow and premixed combustion (Ref[27])

Figure 5-20 shows that for premixed flames with the large PVC, the pressure drop ΔP is higher in a premixed than in cold (isothermal) flow at the same Reynolds number.

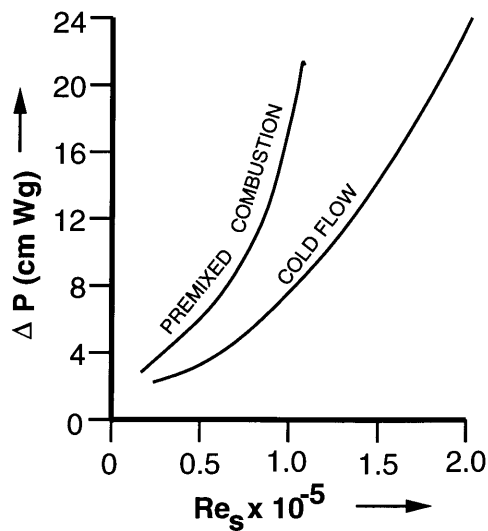


Figure 5-20: Variation of pressure drop ΔP against Re_s during premixed combustion and cold (isothermal) flow (Ref[27])

The noise and vibration is not so pronounced in non-premixed combustion. In fact, it has been observed that the intensity of the PVC is damped by a factor of two in this case (Ref[27]). Since most conventional combustors operate in this mode, the frequency of oscillation of the PVC is not a significant factor.

On the other hand, since the PVC is intensified in premixed combustion, it is important to design the combustor with the frequency of PVC in mind (see Figure 5-19). However, because of the intensified levels of turbulence due to the PVC, mixing of products with reactants in the recirculating zone is enhanced and therefore the approximation of the combustion zone as a perfectly stirred reactor (Chapter 2) is even more accurate for premixed flames.

In general, depending on the type of flame, combustion reduces the length and increases the width of the recirculating region and these changes are most pronounced in premixed combustion. This is independent of constraining parameters such as confinement (Ref[27]). Therefore, on account of this observation, it is possible to reduce the overall length of the combustor .

5.5 Design parameters for the combustor

Based on the discussion in various subsections of Section 5.4, it is possible to develop the basic structure of the combustor as shown in Figure 5-21. The various geometrical relations can be also inferred from Section 5.4:

$$\frac{L_d}{D_e} = 0.7$$

$$\frac{D_f}{D_e} = 2$$

$$\theta_d = 10^\circ$$

and so

$$D_0 = 0.75D_e \text{ and}$$

$$X = 2D_e \quad (5.6)$$

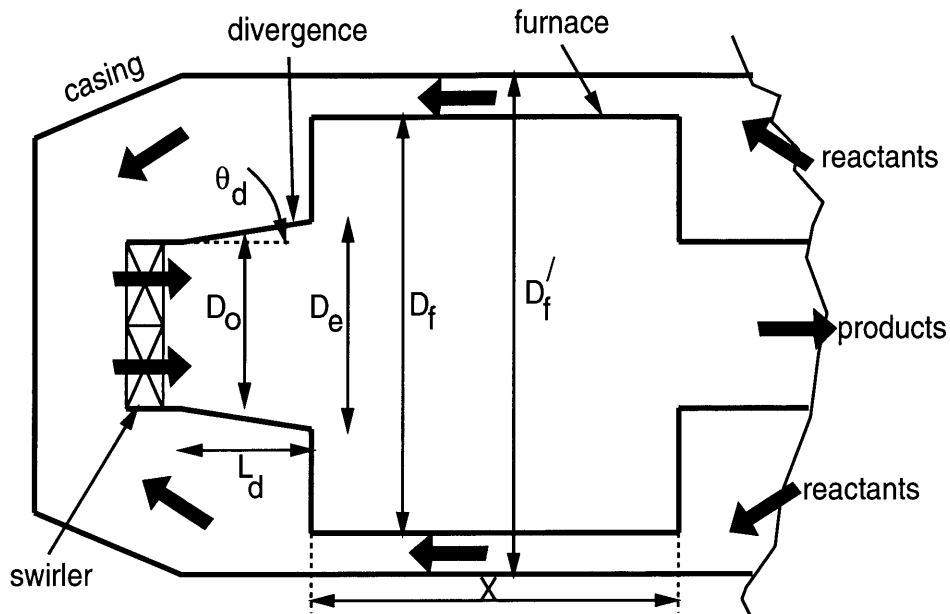


Figure 5-21: Parameters of the designed combustor

Since the central recirculation during combustion is short and wide, it may be assumed that the volume V of the recirculation region occupies the entire cylindrical furnace enclosure downstream of the exit in Figure 5-21. From the geometry, therefore, the volume can be related as:

$$V = \frac{\pi}{4} D_f^2 x = 14.71 D_0^3 \quad (5.7)$$

The volume of the combustor is determined from Figure 2-4. As explained in Chapter 2, the volume of the combustor, V , need not exceed 20000cm^3 even when burning an ultra-lean methane-air mixture. From equations 5.3 and 5.4:

$$D_0 = 0.111\text{m} = 111\text{mm}$$

$$\begin{aligned}
 D_e &= 0.148\text{m} = 148\text{mm} \\
 D_f &= 0.295\text{m} = 295\text{mm} \\
 x &= 0.295\text{m} = 295\text{mm}
 \end{aligned}
 \tag{5.8}$$

5.6 Swirler vane design

From Figure 5-16, it has been seen that the use of profiled-vane swirlers since it is advantageous to increase the efficiency of swirl generation η . Since the dimension D_0 is small ($\approx 110\text{mm}$), it has been decided to use a hubless swirler whose blades are of constant thickness and of constant radius as shown in Figure 5-22. The geometry of the swirler blade is determined at the mean diameter of $\frac{D_0}{2}$.

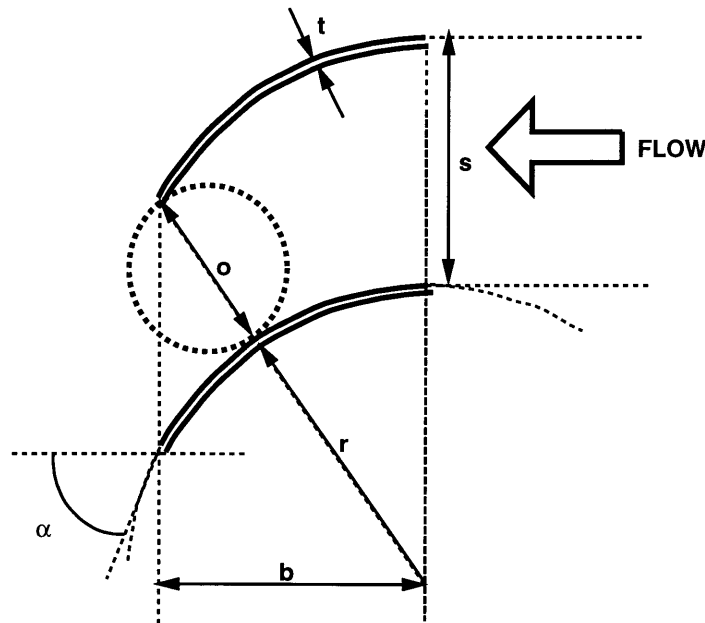


Figure 5-22: Swirler vane construction: α = blade angle; b = blade width; r = blade radius; o = throat diameter; s = blade spacing calculated at $\frac{D_0}{2}$; t = blade thickness

Ref[1] gives a relation between the desired flow angle α' and the swirl number S as:

$$S = \frac{2}{3} \tan \alpha' \quad (5.9)$$

The blade angle α is approximately 5° greater than the flow angle:

$$\alpha = \alpha' + 5^\circ \quad (5.10)$$

From Section 5.4.1, $S = 1$. Hence from equations 5.6 and 5.7:

$$\alpha = 61^\circ \quad (5.11)$$

The number of blades in the swirler is taken, rather arbitrarily, as 10. Considering the magnitude of diameter D_0 and the flow characteristics, this number is suggested in Ref[22]. Geometrically, therefore, s may be determined as:

$$\pi \frac{D_0}{2} = 10s$$

and so:

$$s = 0.0174\text{m} = 17.4\text{mm} \quad (5.12)$$

The blade width, b , and spacing, s , are determined from a correlation given in Ref[34]:

$$\left(\frac{b}{s}\right)_{opt} = 1.25 \sin 2\alpha \quad (5.13)$$

Using equation 5.9, therefore:

$$b = 0.0185\text{m} = 18.5\text{mm} \quad (5.14)$$

The thickness of the blades, t , is suggested in Ref[22] to be 0.5 mm.

The other dimensions in Figure 5-22 may be found from simple geometrical relations:

$$r = \frac{b}{\sin\alpha}$$
$$o = -r + \sqrt{2sr \cos\alpha + r^2} \quad (5.15)$$

where r is the blade radius and o is the diameter of the throat opening in Figure 5-22.

Therefore:

$$r = 0.0212\text{m} = 21.2\text{mm}$$
$$o = 0.0072\text{m} = 7.2\text{mm} \quad (5.16)$$

5.7 Heat transfer performance

Since the inlet and outlet to the combustor are at different ends, it is possible to assume that the cold reactants flow around the combustor and enter it as shown in Figure 5-21. If the casing shown has a diameter D'_f , it can be assumed the ratio $\frac{D'_f}{D_f}$ is the same as the ratio of the outer to inner diameter of the fabricated heat exchanger shown in Figure 4-7 (= 1.22). This assumption is by no means critical, but it assists in finding a reasonable numerical value associated with the hydraulic diameter of the area of cross-section of flow of reactants around the combustor.

The furnace region of the combustor shown in Figure 5-21 is the biggest exposed area of the combustor for heat transfer and therefore the swirler and divergence may be neglected for the

purposes of evaluating the heat transfer without significant loss of accuracy. The flow around the furnace and inside it is, of course, turbulent. Therefore equation of heat transfer for turbulent flow given by equation 4.6 can be employed to find the overall heat transfer coefficient for this geometry. For the purpose of finding the heat transfer coefficient inside the combustor, it is assumed that the properties of the product stream can be evaluated at the flame temperature 1500 K and assuming that the drop in temperature ΔT_4 † is negligible (this assumption is proved to be correct). Then using the continuity relation:

$$\rho \frac{\pi D_f^2}{4} V_f = \dot{m}$$

where $\dot{m} = 2.32 \text{ kg/s}$,

ρ is the average density of gases evaluated at a temperature of 1500 K

and 4 atm pressure,

D_f is the furnace diameter and

V_f is the velocity of flow,

V_f is determined and this value used in the definition of Reynolds number:

$$Re = \frac{V_f D_f}{\nu_f}$$

where ν_f is the kinematic viscosity of the gases evaluated at 1500 K and 4 atm pressure. Hence it is obtained:

$$Re = \frac{55400}{D_f}$$

† difference in temperature of the hot gases at the flame and at the combustor exit

which is used in equation 4.6 to determine the Nusselt number that is used to determine the heat transfer coefficient as:

$$Nu = \frac{124.69}{D_f^{0.8}}$$

From the above equation and using the relation in equation 4.7, the heat transfer coefficient within the furnace region of the combustor is derived as:

$$h_f = \frac{10.89}{D_f^{1.8}} \quad (5.17)$$

Similarly the heat transfer coefficient between the walls of the combustor and the reactant stream flowing between the walls of the combustor (of diameter D_f) and the casing (of diameter D'_f in Figure 5-22) is derived as:

$$h'_f = \frac{23.18}{D_f^{1.8}} \quad (5.18)$$

where the relation $\frac{D'_f}{D_f} = 1.22$ has also been used (see earlier part of this section).

Using equation 4.8, the overall heat transfer coefficient U for the furnace is derived as:

$$U = \frac{7.41}{D_f^{1.8}} \frac{W}{m^2K} \quad (5.19)$$

This result can be combined with the energy equation, that expresses the equality in energy gain by the cold stream (reactants) with the loss of heat energy by the hot stream (products):

$$(\dot{m}c_p)_p \Delta T_4 = U A_h \Delta T \quad (5.20)$$

where p is the subscript denoting products

ΔT_4 is the temperature drop of hot gases (products) from the flame to the exit of the combustor due to heat transfer to surroundings

A_h is the area of heat transfer for the cylinder

ΔT is the temperature difference between the hot and cold streams that is a function of ϕ derivable from Figure 2-6

Thus the temperature drop of hot gases from the flame to the exit of the combustor, ΔT_4 , is derived from equation 5.17 using the values of U obtained from equation 5.16 above, the area A_h calculated from the geometry in Figure 5-22, $\dot{m} = 2.32$ kg/s, the bulk average specific heat of the hot gases c_p evaluated at the flame temperature 1500 K, and ΔT derivable as a function of ϕ as mentioned above:

$$\Delta T_4 = 16.7 D_f^{0.2} (\phi + 0.1) \quad (5.21)$$

When $\phi = 0.37$ (from Figure 2-6, this is the value of ϕ at which no heat exchanger is needed to raise the enthalpy of the reactants) $\Delta T_4 = 6.16$ K.

The above ΔT_4 value is not significant compared to the magnitudes of other operational temperatures of the gas-turbine engine. Therefore, the temperature drop within the combustor can be considered to be negligible.

5.8 Pressure drop in the combustor

The pressure drop in the combustor is divided in Ref[27] into two parts: the pressure loss across the swirler vanes ΔP_v and the pressure drop from just downstream of the swirler to the exit of the combustor ΔP_{cc} .

The pressure drops are given by the following relations (Ref[27]):

$$\begin{aligned}\Delta P_v &= \xi_v \frac{v^2 \rho}{2} \\ \Delta P_{cc} &= \xi_{cc} \frac{U_o^2 \rho}{2}\end{aligned}\tag{5.22}$$

where ξ_v is the pressure loss coefficient = 1.2 for profiled vanes

v is the average tangential velocity at the exit of the swirler which can be found from geometrical considerations and the mass flow rate

ξ_{cc} is the pressure loss coefficient which is a function of the outlet geometry = 1.8 for the geometry considered in Figure 5-21

U_o is the average exit velocity from the combustor which is the maximum considered in the augmented heat exchanger in Figure 4-10 (100 m/s)

For the designed combustor and for $\dot{m} = 2.32$ kg/s, the pressure drops are:

$$\Delta P_v = 1.94\% \text{ of the average combustor pressure of 4 atm}$$

$$\Delta P_{cc} = 2.46\% \text{ of the average combustor pressure of 4 atm}$$

and the total pressure drop in the combustor thus is:

$$\Delta P_c = \Delta P_v + \Delta P_{cc} = 4.4\% \text{ of the average combustor pressure of 4 atm}\tag{5.23}$$

The total pressure drop ΔP_c in the combustor is 4.4% of the average pressure inside the combustor

tor. Though this is higher than the limit mentioned in Section 5.1 (4%), this slight increase is made up by reduced pressure drop in the heat exchanger, the pressure drop in the heat exchanger being much less than the corresponding tolerance limit (see Section 4.5.3.2). Therefore, this combustor is admissible as a viable design.

5.9 Flowfield simulation

As mentioned in Section 5.4.7, the flowfield in a highly swirling environment is strongly three-dimensional in nature. Because of this three-dimensionality, it is impossible to simulate this flowfield in detail within in the combustor using current computer technology.

However, it is useful to get an overall, while approximate idea of the flow in the combustor. In particular, it is important to see whether or not a central recirculation region is produced and determine the approximate size of this recirculation region. This is necessary because the Reynolds number of the flow in the design in Figure 5-21 is of order of magnitude 10^6 and we did not find experimental data at these Reynolds numbers. Also, in Section 5.4.2, the length of the recirculation region X in an unconfined flow is found to be $\approx 3D_e$ (D_e is the exit diameter) and no data is reported for this parameter for confined flows. The result in Section 5.4.8 shows that in the reacting case, the length of the recirculation zone is reduced. This result is used in limiting the value of X in Figure 5-22 to $2D_e$ (thereby achieving a reduction in combustor size at the same time).

Figure 5-23 and 5-24 show the simulation of cold (non-reacting) swirling flow in the designed combustor using the computational fluid dynamics simulation package FLUENT (Ref[3]). The swirl number S has been taken as 1 (it is superimposed as a tangential velocity calculated assuming a forced vortex on a pure axial flow at the inlet). The simulation is restricted to two-dimensional axisymmetric flow, i.e. there is no variation of any flow variable in the θ direction. This assumption

is the basis of the $k - \epsilon$ model (Ref[24]) which has been used to simulate turbulence. The details of the $k - \epsilon$ model will not be described here but it should be noted that this model is known to be inaccurate in strongly recirculating and swirling flows and the results are only qualitative. This is because, as mentioned before, the swirling flow is highly three-dimensional and hence anisotropic whereas the $k - \epsilon$ model assumes that the flow is isotropic. However, the simulation is useful in gauging macro trends of the flow, which should be apparent even while using the most rudimentary (but complete) theory. Because of the inaccuracy in the modelling, the results presented assume a certain granularity to emphasize that the larger trends are those that are important to the design and the exact solution, while certainly helpful, is not crucial to the working design.

Figure 5-23 shows the contours of the stream function in the combustor. The tangent to each contour determines the direction and magnitude of the velocity vector. The central recirculation region can be clearly seen.

Figure 5-23 shows the filled contours of axial velocity in the designed combustor (Figure 5-21). An average bulk flow axial velocity of 60 m/s is imposed at the inlet and the tangential velocity, simulated as that obtained in a forced vortex (this assumption is consistent with the fluid flow just downstream of a vaned swirler) so that swirl number $S = 1$ is superimposed. The Reynolds number of flow Re_s is of the order of 10^6 . As predicted in Figure 5-8, a strong recirculation region must be established and is indeed seen in Figure 5-23.

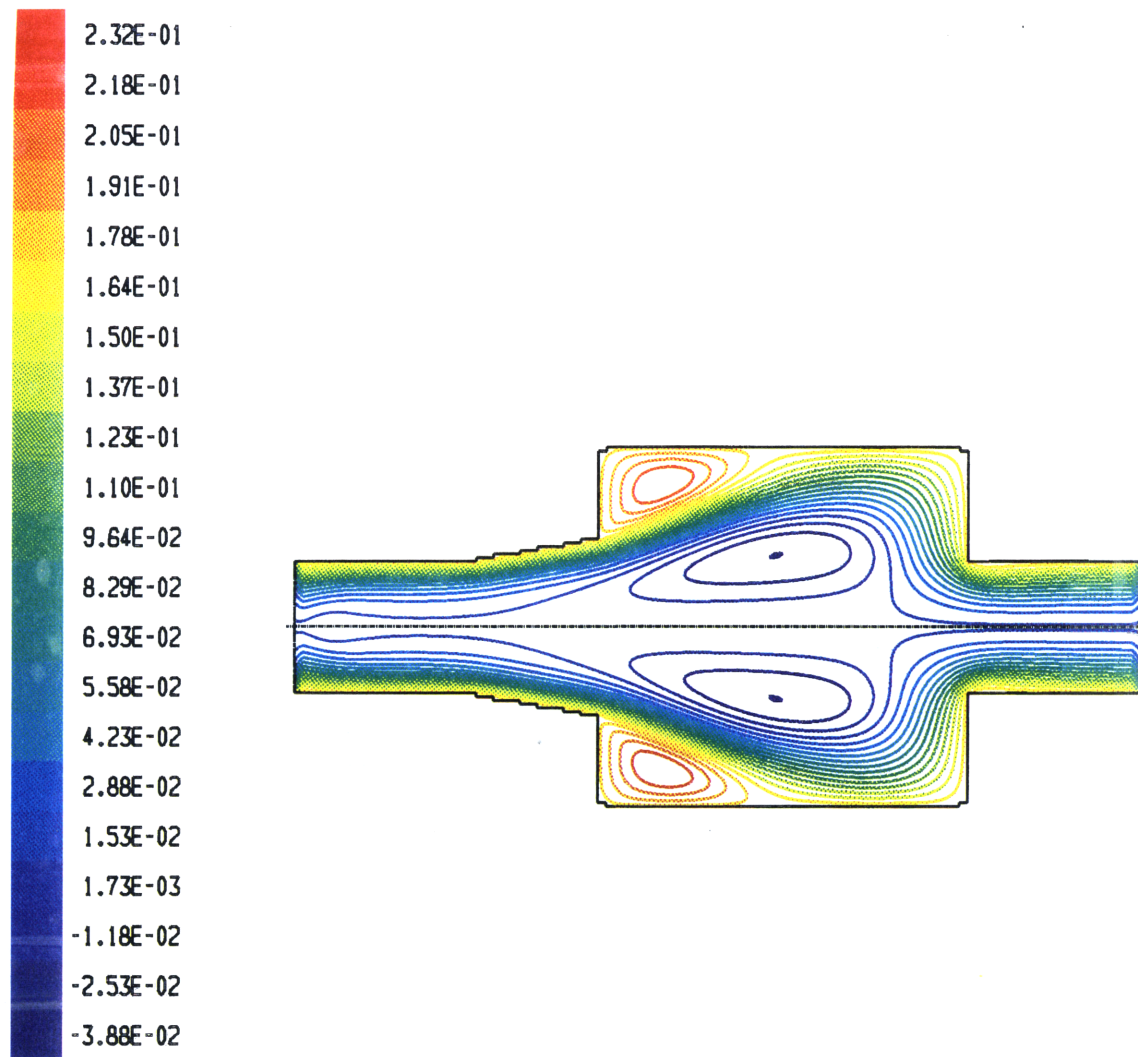


Figure 5-23: Contours of stream function of cold flow simulation in the combustor designed in Figure 5-21. Reynolds number Re_s is of the order of 10^6 and $S = 1$. The large central recirculation region and the small annular recirculation region near the wall of the furnace can be seen

The small annular recirculation region mentioned in Section 5.4.2. that develops close to the

wall of the furnace when $0.6 < S < 1.6$ can be clearly seen in Figures 5-23 and 5-24.

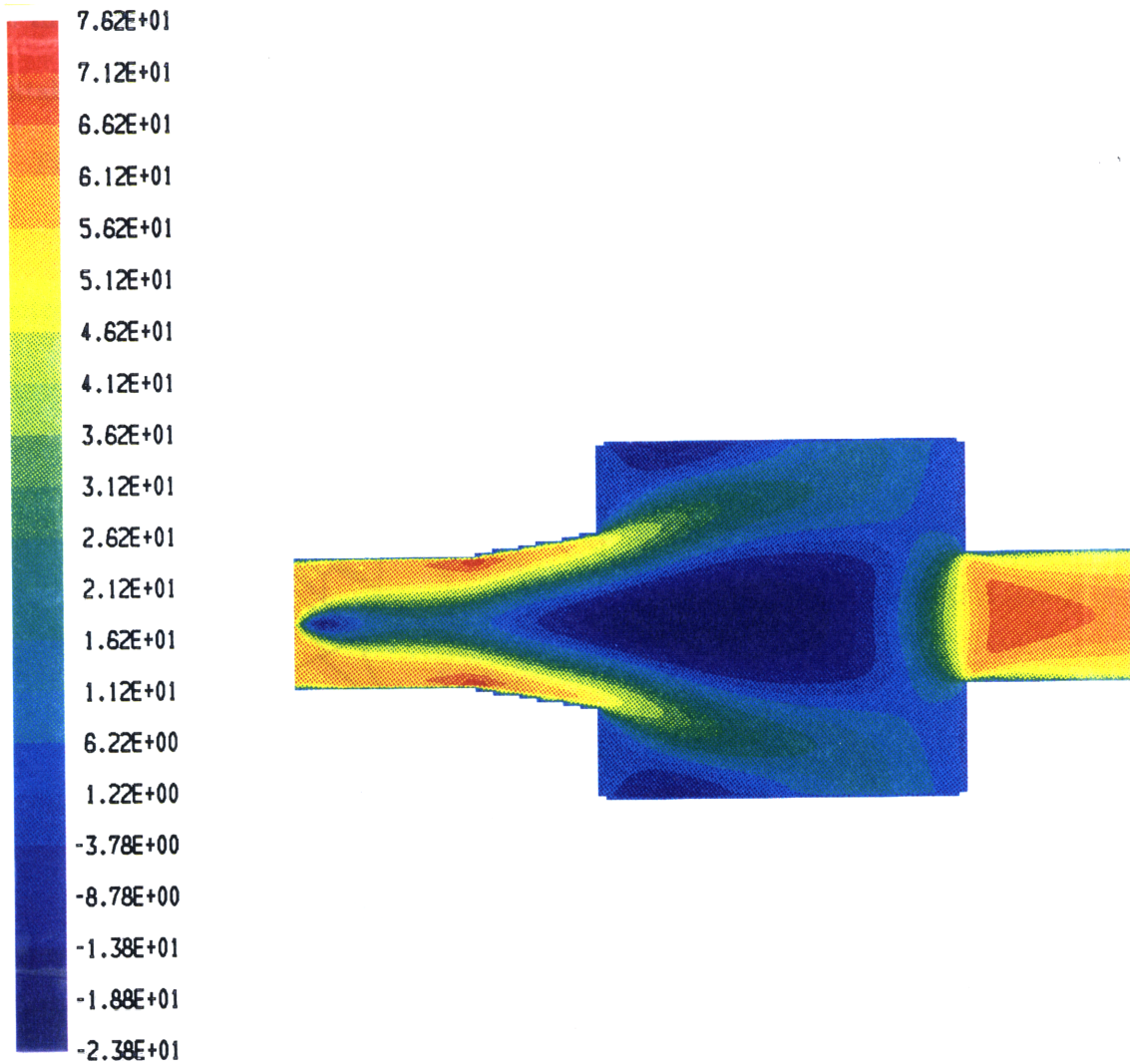


Figure 5-24: Filled contours of axial velocity in the combustor designed in Figure 5-21 during cold flow simulation. Reynolds number Re_s is of the order of 10^6 and $S = 1$. The large central recirculation region and the small annular recirculation region near the wall of the furnace can be seen

5.10 Conclusions

Of the existing designs of ultra-lean combustors, the swirler type of swirl combustor is found most suitable for the purpose of this project.

Figure 5-25 shows a three-dimensional view of the designed combustor. The swirler imparts a large tangential velocity on the inlet flow. At the exit of the divergence, in the furnace, a strong central recirculation region is formed, as evident in Figures 5-23 and 5-24.

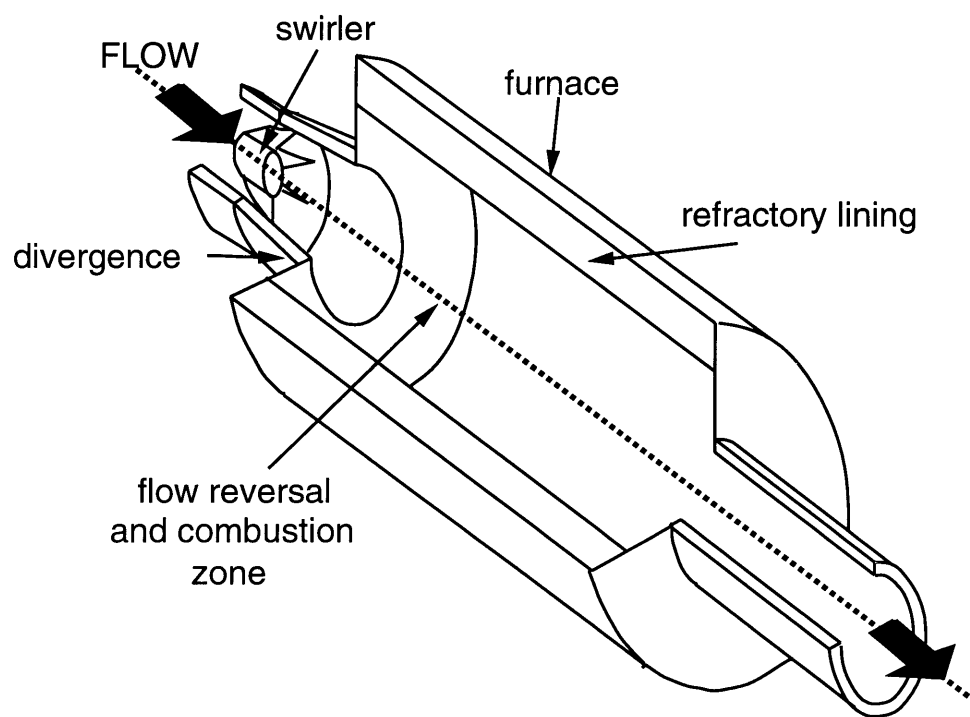


Figure 5-25: Cut-away three-dimensional view of the designed combustor

The size of the combustor is made virtually independent of the equivalence ratio ϕ of the methane-air mixture (see Chapter 2) by changing the dimensions of the heat exchanger to raise the

reactant stream temperature. This is in contrast to the size of the heat exchanger, which is highly dependent on ϕ .

Analysis shows that the combustor cannot be relied upon to function simultaneously as a heat exchanger even though the reactants are allowed to flow outside the combustor (see Figure 5-23); the temperature drops within the combustor are of the order of 6 K and therefore found to be too low to be of any significance.

The predicted pressure drop in the combustor (4.4%) is found to be slightly higher than higher than the tolerated limit of 4%. However, the maximum heat exchanger pressure drop is of the order of 5%, which is much lower than the tolerated limit of 8%. This reduction in pressure drop in the heat exchanger can be used to make up for the increased pressure drop in the designed combustor.

Structurally, the furnace region of the combustor must be lined with refractory material. The refractory material, usually made of ceramic, can withstand the high temperatures of combustion (≈ 1500 K). Since ceramic is a bad conductor of heat, the lining will radiate energy back to the combusting gases and not allow significant heat loss to the surroundings.

Chapter 6

Conclusions and Future Work

Joy, joy for ever! my task is done -
The Gates are past and Heaven is won.
— *Thomas Moore(1779-1852 AD)* - Lalla-Rookh “Fire Worshippers”

6.1 Purpose of the thesis

In this thesis, the thermal design and analysis of a recuperative combustor to be installed in a gas-turbine engine has been carried out. The aim of using a such a combustor is to ensure the combustion of very low BTU content fuels (also called poor fuels). Specifically, this project aims at developing a system incorporating a recuperative combustor to burn mine ventilation air (primarily a mixture of methane-air in which the volume concentration of methane is very low). This work has provided design alternatives for a range of equivalence ratios of the methane-air mixture for a unique gas-turbine engine (SOLAR GS-350) that was chosen at the beginning of Phase II of the project (Ref[23]).

6.2 Approach to the problem

The combustor was approximated as a perfectly stirred reactor (PSR). It is an established method to predict the performance of combustors in industrial and aviation gas-turbine engines. Using this model, it was verified that the recuperative combustor, comprising a separate heat exchanger and a combustor, were necessary to ensure the complete combustion of the methane-air mixture. Thermal design of the heat exchanger and combustor were carried out utilizing quantitative information from the the PSR model and from commercial choices available. Thus, a possible range of solutions to the design were suggested. An integration of the recuperative combustor into the gas-turbine engine GS-350 will be suggested in Section 6.4. Mechanical design aspects such as structure and vibration were not dealt with in detail except some important areas that affected the thermal design and vice-versa.

6.3 Summary of design

The results of the thermal design attempted in the previous chapters have been summarized briefly as follows:

- In Phase II of the project, the Solar GS-350 gas-turbine (capable of developing 225kW maximum rating) was selected as the hardware platform.
- It was determined that the major modification needed was to be performed on the combustor of the GS-350 - the compressor and turbine were essentially left untouched and the recuperative combustor designed corresponding to their specifications.
- The recuperative combustor was determined to consist of two parts - a combustor and a heat exchanger.

- The thermal design and analysis of heat exchangers narrowed down the number of potential options from hundreds to three. All the three heat exchangers designs are of the counterflow plate-fin compact kind. The three plate-fin geometries found suitable were plain-fin 46.46T, Wavy-fin 17.8- $\frac{3}{8}$ W and Pin-fin PF-3.
- The principle of swirl employed in most combustors of jet and industrial gas-turbines was utilized in the modified combustor. This is due to the two advantages that a swirler provides - a region of near homogenous mixing of product species with the reactants and flame stabilization. The combustor size was determined to be practically independent of the equivalence ratio of the methane-air mixture used for a given mass flow rate.
- Temperature limits of the combustor and the heat exchanger as functions of the equivalence ratio were found by approximating the turbulent mixing in the reverse flow downstream of the swirler in the combustor by means of a perfectly stirred reactor; this model closely approximates most conventional combustion systems.

6.4 Design integration

In Chapter 4, a design for the heat exchanger was suggested and in Chapter 5, a design for a combustor was recommended. Though each of these designs are physically independent of each other, it is important to evaluate whether the two components are structurally compatible with one another at least in the concept mechanical design stage.

Figure 6-1 shows a possible method of integrating the design of the heat exchanger and the combustor into the overall structure of the gas-turbine engine. The compressor and turbine have not been modified. The only modifications include the recuperative combustor, which, as has been

seen in earlier chapters, has been redesigned and split into the separate units of heat exchanger and combustor. This particular configuration is similar to the one shown in Figure 4-7 where the combustor has been placed over the heat exchanger (this combination replaces the original combustor).

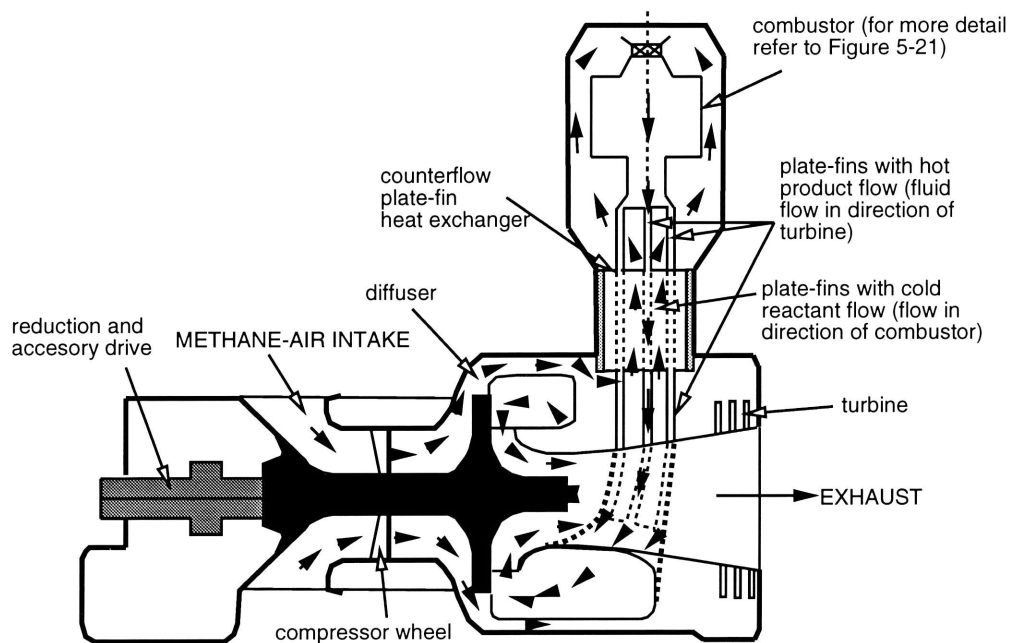


Figure 6-1: Conceptual integration of heat exchanger and combustor designs into the GS-350 gas-turbine engine. Note: figure not to scale.

6.5 Future work and accuracy of the current design

A project that aims at developing a technology and commercializing it will essentially consist of three phases:

- The first phase attempts to answer the question “is the concept feasible?” and comprises technical and economic feasibility. Thus, in this phase, the concept of the technology would

be investigated into and its viability for commercialization would be assessed.

- Once the question of feasibility has been satisfactorily answered, the detailed process is undertaken in the second phase to answer the question “how exactly to do it?”. For the recuperative combustor, this detailed process includes thermal and mechanical design development. Thermal design defines the basic structure, shape and size of the recuperative combustor. Mechanical design includes vibration and structural analysis. A prototype testing of the developed technology must be done in the field in order to assess the performance of the design and increase its robustness. Therefore, this phase involves the most capital, labour and time investment.
- Assuming that the detailed design and testing concluded in the second phase is successful, the finished product is ready for commercial deployment and production in the third and final phase. Production infrastructure, marketing, distribution and on-site servicing are important in assuring that the product is a commercial success.

Thermal design, the first step in the second stage development of the recuperative combustor, has been achieved in this thesis. It included certain theoretical performance predictions as detailed in earlier chapters. However, since subsequent mechanical design and testing remain to be completed, it is only possible to say that the performance of the modified GS-350 gas-turbine engine in the field will be within the ballpark figures of the estimates provided in this thesis; a definite correlation can only be determined after experimental data has been obtained.

Bibliography

1. Beer, J.M., Chigier, N.A., *Combustion Aerodynamics*, Applied Science Publishers, 1983.
2. Cohen, H., Rogers, G.F.C. and Saravanamuttoo, H.I.H., *Gas Turbine Theory, III ed.*, Longman Gp. U.K Ltd., 1987.
3. *FLUENT (version 4.11) Fluid Flow Modelling*, FLUENT Inc., 1991.
4. Ghoniem, A.F., *MIT course 2.280: Fundamentals of Reacting Flows and Combustion*, instructor's class notes, 1993.
5. Glarborg, P., Kee, R.J., Grcar, J.F., Miller, J.A., *PSR: A FORTRAN program for Modelling Well Stirred Reactors*, Sandia National Laboratories, January 1990.
6. Glassman, A.J., *Combustion*, Academic Press, 1977.
7. Glassman, A.J., *Turbine Design and Application*, NASA, 1972.
8. Gupta, A.K., Lilley, D.G., Syred, N., *Swirl Flows*, Abacus Press, 1984.
9. Gyftapolous, E.P. and Beretta, G.P., *Thermodynamics - Foundations and Applications*, Macmillan Publishing Co., 1991.
10. Howell, J.R., Buckius, R.O., *Fundamentals of Engineering Thermodynamics*, McGraw Hill, 1987.
11. Kakac, S., Bergles, A.E., Mayinger, F., *Heat Exchangers — Thermal-Hydraulic Fundamentals and Applications*, Hemisphere Publishing Corp., 1981.
12. Kays, W.M., London, A.L., *Compact Heat Exchangers*, McGraw Hill, 1984.
13. Kee, J., Ripley, F.M., and Miller, J.A., *Chemkin Thermodynamic Database*, Sandia National Laboratories, 1987.
14. Keenan, J.H., Chao, J., Kaye, J., *Gas Tables*, John Wiley and Sons, 1983.
15. Lapina, R.P., *Estimating Centrifugal Compressor Performance*, Gulf Publishing Co., 1982.

16. Lefebvre, W.A., *Gas Turbine Combustion*, McGraw-Hill, 1983.
17. Lienhard, J.H., *A Heat Transfer Textbook*, Prentice-Hall Inc., 1981.
18. Lopez, J.M., *Axisymmetric Vortex Breakdown: Parts 1 and 2*, Journal of Fluid Mechanics, Vol 221, 1990.
19. Mizutani, Y., Satomura, M., *Combustion of Ultra-Lean Combustible Mixtures in a Heat Recirculation Type Cyclone Furnace System*, 19th Symposium (International) on Combustion/Combustion Institute, 1982.
20. Private communication: Ghoniem, A.F., Professor, Mechanical Engineering, Massachusetts Institute of Technology.
21. Private communication: Sööt, P.M., President, NorthWest Fuel Development Inc., Portland, Oregon.
22. Private communication: Wilson, D.G., Professor, Mechanical Engineering, Massachusetts Institute of Technology.
23. Solar, *Operations and Maintenance Manual — GS-350*, Publication SD 3099, October 1971.
24. Sonin, A.A., *MIT course 2.273: Turbulent flow and Transport*, instructor's class notes, 1993.
25. Sonntag, R.E., Wylen, G.J.V., *Introduction to Thermodynamics*, John Wiley and Sons, 1982.
26. Sööt, P.M., *SBIR proposal: Gas Turbines for Combustion of Natural Gas in Mine Ventilation Air: Phases I and II*, Northwest Fuel Development Inc., 1990.
27. Syred, N., Beer, J.M., *Combustion in Swirling Flows: A Review*, Combustion and Flame, 123, 1974.
28. Syred, N., Dahman, K.R., *Effects of High Levels of Confinement upon the Aerodynamics of Swirl Burners*, AIAA, Vol2, No.1, 1978.
29. Syred, N., Dahman, K.R., Styles, A.C., Najim, S.A., *A Review of Combustion Problems associated with Low Calorific Value Gases*, Journal of the Institute of Fuel, 1977.
30. Syred, N., Gupta, A.K., Beer, J.M., *Temperature and Density Gradient Changes arising with the Precessing Vortex Core and Vortex Breakdown in Swirl Burners*, Journal of the Institute of Fuel, 1972.
31. Walker, G., *Industrial Heat Exchangers*, Hemisphere Publishing Corp., 1990.
32. Weinberg, F.J., *Advanced Combustion Methods*, Academic Press, 1984.
33. Weiss, M.A., Longwell, J.P., *High Temperature Reaction Rates in Hydrocarbon Combustion*, Ind. Eng. Chem., vol 47, 1955.
34. Wilson, D.G., *Design of High-Efficiency Turbomachinery and Gas Turbines*, MIT Press, 1984.
35. Wood, B.D., *Applications of Thermodynamics*, Addison-Wesley Publishing Co., 1969.

Appendix A

GS-350 cycle calculations: derivations

A.1 Efficiency of an Air-standard ideal Recuperative Brayton cycle

The air-standard ideal Recuperative Brayton cycle is shown in Figure A1-1. The corresponding T-S diagram is shown in Figure A1-2.

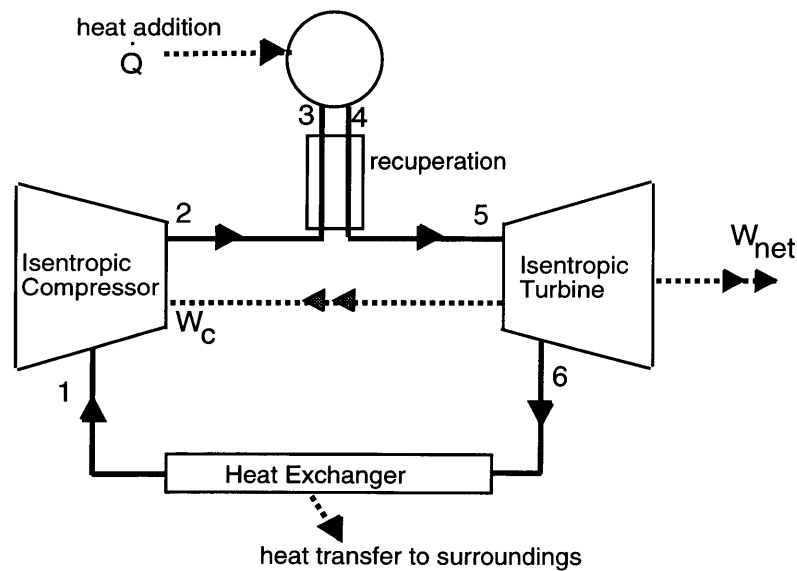


Figure A1-1: Recuperative Brayton cycle. Temperature of the reactants at T_2 are raised to a higher temperature T_3 (which is the minimum required for ignition in the combustor) by means of heat transfer from hot products at T_4

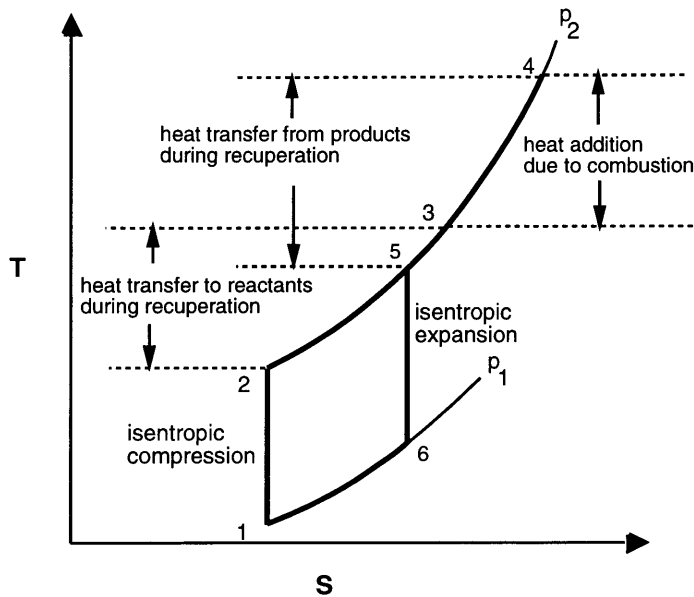


Figure A1-2: T-S diagram of the Recuperative Brayton cycle. 4-5 is heat transfer from hot product stream to cold reactant stream. 2-3 is the enthalpy increase of the cold reactant stream due to this heat transfer

Work done in compressing the gas W_c in the compressor (process 1-2 in Figure A1-2) can be written as the difference of enthalpies of the gas before and after compression if the process is ideal:

$$W_c = -(h_2 - h_1) = -c_p(T_2 - T_1) \quad (\text{A.1})$$

where h_1 is the enthalpy of the gas before compression with temperature T_1

h_2 is the enthalpy of the gas after compression with temperature T_2

c_p is the mean specific heat of the fluid

Similarly the ideal gross work obtainable from the turbine as the gases expand (process 5-6 in Figure A1-2) may be written as:

$$W_t = (h_5 - h_6) = c_p(T_5 - T_6) \quad (\text{A.2})$$

where h_5 is the enthalpy of the gas before expansion with temperature T_5

h_6 is the enthalpy of the gas after expansion with temperature T_6

An isentropic compression or expansion may be written as in equation 3.5. Using the ideal law $P = \rho RT$, this may be written in terms of temperatures as:

$$\frac{T_2}{T_1} = \frac{T_5}{T_6} = r_p^{\frac{k-1}{k}} \quad (\text{A.3})$$

where k is the adiabatic isentropic coefficient and

r_p is the pressure ration

The maximum theoretical chemical rate of heat addition can be similarly calculated (process 3-4 in Figure A1-2) as:

$$\dot{Q} = (h_4 - h_3) = c_p(T_4 - T_3) \quad (\text{A.4})$$

where h_3 is the enthalpy of the gas before combustion with temperature T_3

h_4 is the enthalpy of the gas after combustion with temperature T_4

Enthalpy is added to reactants \dot{q}_{reac} due to heat transfer from hot products during recuperation (process 2-3 in Figure A1-2). This heat transfer results in a loss of enthalpy to the products \dot{q}_{prod} . Since the heat transfer is assumed ideal $\dot{q}_{reac} = \dot{q}_{prod}$.

By the definition of cycle efficiency η_r (Ref[*]):

$$\eta_r = \frac{\text{useful work output}}{\text{total chemical heat energy supplied}}$$

Therefore:

$$\eta_r = \frac{W_t - W_c}{\dot{Q} + \dot{q}_{reac} - \dot{q}_{prod}}$$

or

$$\eta_r = 1 - \left(\frac{1}{r_p} \right)^{\frac{k-1}{k}} \quad (\text{A.5})$$

A.2 H_{pc} , W_c , η_{pc} and η_{cad}

A.2.1 Polytopic head work H_{pc} done in compression of a gas

This equation derives from integrating the steady-state, steady-flow work givenby:

$$H_{pc} = \int_1^2 v dP \quad (\text{A.6})$$

where v is the specific volume and

dP is the incremental change in pressure

Since the polytopic process is given from equation 3.*:

$$Pv^n = \text{constant} = C^n \Rightarrow v = \frac{C}{P^{\frac{1}{n}}} \quad (\text{A.7})$$

we arrive at the result by substitution:

$$H_{pc} = \int_1^2 \frac{C dP}{P^{\frac{1}{n}}}$$

$$\Rightarrow H_{pc} = C \frac{n}{n-1} P_1^{\frac{n-1}{n}} \left[\left(\frac{P_2}{P_1} \right)^{\frac{n-1}{n}} - 1 \right]$$

where P_1 and P_2 are the pressures of the gas before and after compression respectively. From equation A.7, we can deduce that:

$$C P_1^{\frac{n-1}{n}} = P_1 v_1$$

Therefore we get:

$$H_{pc} = RT_1 \frac{n}{n-1} \left[r_p^{\frac{n-1}{n}} - 1 \right] \text{ kJ/kg} \quad (\text{A.8})$$

where $r_p = \frac{P_2}{P_1}$ is the pressure ratio of compression.

A.2.2 Actual work done W_c done during compression

The actual work done during compression is the change in enthalpy of the gas because of this (process 1-2 in Figure A1-2) and can be written as:

$$W_c = c_p \Delta T = c_p (T_2 - T_1)$$

Since we have from equation A.3 the relation between temperatures:

$$T_2 - T_1 = T_1 \left[\left(\frac{T_2}{T_1} \right) - 1 \right] = T_1 (r_p^{\frac{n-1}{n}} - 1)$$

we may see that:

$$W_c = c_p T_1 (r_p^{\frac{n-1}{n}} - 1) \quad (\text{A.9})$$

From the definition of k , the ratio of the specific heats and the relation of the universal gas constant R to the specific heats:

$$\frac{c_p}{c_v} = k \text{ and } c_p - c_v = R$$

we then obtain:

$$c_p = R \frac{k}{k-1} \quad (\text{A.10})$$

Therefore we get:

$$W_c = RT_1 \frac{k}{k-1} (r_p^{\frac{n-1}{n}} - 1) \text{ kJ/kg} \quad (\text{A.11})$$

A.2.3 Polytropic efficiency during compression η_{pc}

Polytropic efficiency η_{pc} is defined as:

$$\eta_{pc} = \frac{H_{pc}}{W_c} \quad (\text{A.12})$$

From equations A.8 and A.11, we may infer that:

$$\frac{n}{n-1} = \frac{k}{k-1} \eta_{pc} \quad (\text{A.13})$$

A.2.4 Relation between polytropic efficiency η_{pc} and adiabatic efficiency η_{cad}

From the temperature relation of equation A.9, we have:

$$T_2 - T_1 = T_1(r_p^{\frac{k-1}{\eta_{pc}k}} - 1) \quad (\text{A.14})$$

If the adiabatic efficiency is η_{ad} , then the temperature difference as above may also be written as:

$$T_2 - T_1 = \eta_{cad}T_1(r_p^{\frac{k-1}{k}} - 1) \quad (\text{A.15})$$

Equations A.14 and A.15, expressing the same temperature difference can now be compared. Hence we have:

$$\eta_{cad} = \frac{r_p^{\frac{k-1}{k}} - 1}{r_p^{\frac{k-1}{\eta_{pc}k}} - 1} \quad (\text{A.16})$$

A.3 Exothermic Energy Yield (ψ) of a methane-air mixture

Let the mixture of methane-air contain β % of methane in air by volume. Ratio of volume of methane to volume of air in a unit mixture of fuel-air is then:

$$\frac{\beta}{100 - \beta} \quad (\text{A.17})$$

At standard conditions of temperature and pressure:

$$\text{ratio of volumes} = \text{ratio of moles}$$

and therefore the molar ratio of methane to air in a unit mixture of fuel-air can be given by equation A.17. Hence the mass ratio of methane to air in the unit mixture of fuel-air can be written as:

$$\frac{16n}{28.96(100 - n)} \quad (\text{A.18})$$

since the molecular weights of methane and air are 16 kg/kmol and 28.96 kg/kmol respectively. Therefore, the total mass per mole of a mixture of methane in air containing β % of methane in air by volume is:

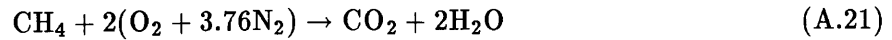
$$16n + 28.96(100 - n) \text{ kg} \quad (\text{A.19})$$

The Lower Heating Value (LHV) of methane is 50 MJ/kg of *fuel* (Ref[*]). From this value we can infer that 16n kg/kmol of methane will release 800n MJ/kmol of energy. This energy is released, however, in a mixture of mass given by equation A.19. Hence the exothermic energy yield (ψ) of the mixture, defined as maximum theoretical energy obtainable from a fuel upon its complete burning can be written as:

$$\psi = \frac{8 \times 10^5 n}{16n + 28.96(100 - n)} \text{ kJ/kg of mixture} \quad (\text{A.20})$$

A.4 Relation between β and equivalence ratio of methane-air mixture ϕ

The stoichiometric equation for the combustion of methane in air is:



From the above equation we may note that molar fuel-air ratio is 1/9.52. Molar fuel-air ratio of a methane-air mixture containin $\beta\%$ of methane in air by volume is given by equation A.17. Therefore, the equivalence ratio of a methane -air mixture ϕ , which can be generally defined for any fuel-air mixture as:

$$\phi = \frac{\text{desired fuel-air ratio}}{\text{stoichiometric fuel-air ratio}} \quad (\text{A.22})$$

can then be written as:

$$\phi = \frac{\frac{\beta}{100-\beta}}{\frac{1}{9.52}}$$

or

$$0.1\phi = \frac{\beta}{100 - \beta}$$

Since the number β is small compared to 100 , we may then write:

$$0.1\phi = \frac{\beta}{100}$$

and therefore, we obtain:

$$\beta = 10\phi \quad (\text{A.23})$$